AKADEMIA GÓRNICZO-HUTNICZA IM. STANISŁAWA STASZICA W KRAKOWIE

FIELD OF SCIENCE: Physics

SCIENTIFIC DISCIPLINE: Physical Science

DOCTORAL DISSERTATION

Tailoring the magnetic anisotropy of antiferromagnetic thin films in epitaxial multilayer systems and ferromagnetic / antiferromagnetic nanostructures

Author: Hashim Nayyef

Supervisor: dr hab. inż. Michał Ślęzak

Completed at: AGH University of Krakow, Faculty of Physics and Applied Computer Science

Kraków, 2023

The contents of this thesis were prepared as a part of a project funded by the National Science Centre (NCN) of Poland titled “Spintronics using insulating antiferromagnets – from fundamental properties to applications” (NCN OPUS-21 2021/41/B/ST5/01149).

NATIONAL SCIENCE CENTRE
POLAND

I would like to express my sincere gratitude to my supervisor dr hab. inż. Michał Ślęzak for guiding me in every step of this research. On that token, I would like to thank dr hab. Anna Kozioł-Rachwał and prof. dr hab. Tomasz Ślęzak for their guidance and my colleagues Weronika Janus, Marcin Szpytma, my friends, and my family for their great support.

Abstract

In this thesis, the interaction between antiferromagnetic (AFM) and ferromagnetic (FM) thin films in various epitaxial multilayer systems is investigated. The first study examines a NiO(111)/Fe(110) bilayer, where the stabilization of two magnetic states with orthogonal spin orientations in the AFM NiO layer is documented. Field-free, reversible switching between these states is demonstrated, which was achieved by the precise tuning of interface magnetic anisotropy (MA), thermal hysteresis of spin reorientation transition, and interfacial FM/AFM exchange coupling. The potential for field-free switching of AFM magnetic moments is highlighted, potentially opening up new possibilities in heat-assisted magnetic recording technology. Furthermore, it is found that the magnetic moments in NiO can be rotated within the NiO(111) sample plane, with the MA and spin orientation in NiO being influenced by the underlying FM Fe layer. By varying the Fe thickness, temperature, or applying a small external magnetic field, modification of the magnetic state and anisotropy of the AFM NiO layer is achieved.

Next, the investigation delves into exchange bias and interfacial AFM spin orientation in CoO(111)/Fe(110) bilayers. The results reveal that exchange bias occurs in the zero-field-cooled system and is determined by the in-plane magnetic state of the Fe sublayer above the Néel temperature (T_N) of CoO. The direction of interfacial frozen AFM CoO spins within the CoO(111)/Fe(110) sample plane is dictated by the uniaxial MA of the Fe layer. Selecting a specific magnetic state of the Fe sublayer when passing the T_N of CoO allows for control over both the axis and direction of interfacial AFM spins within the sample plane.

Lastly, the influence of a nonmagnetic Au spacer on the interaction between FM Fe(110) and AFM CoO(111) sublayers is explored. The findings demonstrate that the thickness of the Fe and Au layers can be adjusted to modify the effective anisotropy of the Fe layer and the strength of the exchange bias interaction between Fe and CoO sublayers. The MA of the FM above the T_N of the AFM plays a crucial role in governing exchange bias and interfacial CoO spin orientation at low temperatures. Furthermore, it is shown that exchange bias can act as the dominant MA source for the FM, allowing for a 90-degree rotation of the easy axis compared to the initial, exchange bias-free orientation.

Overall, these studies provide insights into the intricate interaction between AFM and FM components of epitaxial multilayer systems. The understanding and control of these interactions can potentially find new applications in novel magnetic devices and technologies.

The research conducted in this thesis have led to publishing 5 papers:

- M. Ślęzak, P. Dróżdż, W. Janus, H. Nayyef, A. Kozioł-Rachwał, M. Szpytma, M. Zając, T. O. Menteş, F. Genuzio, A. Locatelli, and T. Ślęzaka. Fine tuning of ferromagnet/antiferromagnet interface magnetic anisotropy for field-free switching of antiferromagnetic spins. Nanoscale, volume 12/ 18091-18095 (2020). DOI: 10.1039/D0NR04193A
- M. Ślęzak, P. Dróżdż, W. Janus, M. Szpytma, H. Nayyef, A. Kozioł-Rachwał, M. Zając, and T. Ślęzak. Tailorable exchange bias and memory of frozen antiferromagnetic spins in epitaxial CoO(111)/Fe(110) bilayers. Journal of Magnetism and Magnetic Materials, Volume 545/168783 (2021). DOI: 10.1016/j.jmmm.2021.168783
- M. Ślęzak, H. Nayyef, P. Dróżdż, W. Janus, A. Kozioł-Rachwał, M. Szpytma, M. Zając, T. O. Menteş, F. Genuzio, A. Locatelli, and T. Ślęzak. Controllable magnetic anisotropy and spin orientation of a prototypical easy-plane antiferromagnet on a ferromagnetic support. Phys. Rev. B, volume 104/ 34434 (2021). DOI: 10.1103/PhysRevB.104.134434
- M. Ślęzak, H. Nayyef, P. Dróżdż, W. Janus, E. Świerkosz, M. Szpytma, M. Zając, A. Kozioł-Rachwał, and T. Ślęzak. Memory of frozen and rotatable antiferromagnetic spins in epitaxial CoO (1 1 1)/Fe and NiO(1 1 1)/Fe bilayers. Nuclear Instruments and Methods in Physics Research Section B: Beam Interactions with Materials and Atoms, Volume 539/148-151 (2023). DOI:10.1016/j.nimb.2023.03.038
- H. Nayyef, E. Świerkosz, W. Janus, A. Klimeczek, M. Szpytma, M. Zając, P. Dróżdż, A. Kozioł-Rachwał, T. Ślęzak, and M. Ślęzak. Tunable interplay between exchange coupling and uniaxial magnetic anisotropy in epitaxial CoO/Au/Fe trilayers. Scientific Reports, volume 13/10902 (2023). DOI: 10.1038/s41598-023-38098-6

Content:

1. Chapter one: Introduction

AFM materials possess immense potential, positioning them as exceptional candidates for the future of spintronic applications. They have the capacity to replace FMs as the active component in spintronic devices. The unique properties of AFM materials, such as their resilience against magnetic field disturbances, absence of undesired stray fields, ultrafast dynamics, and generation of substantial magnetotransport effects, make them highly intriguing and promising from application point of view[1,2].

Synthetic AFM, which consist of two or more antiparallelly coupled FMs typically interconnected through Ruderman-Kittel-Kasuya-Yoshida interactions[3], are currently employed to address device malfunctions arising from FM stray fields in reduced lateral dimensions[4]. This is particularly relevant in scenarios like magnetic random-access memories, where neighbouring cells are meant to be isolated from one another but may experience crosstalk. However, synthetic AFMs only provide partial compensation, as small but non-zero stray fields persist. In contrast, AFM materials inherently offer complete compensation, except for a minute proportion at the interface. To develop a functional "magnet-free" device, it becomes imperative to explore how spin transport can be harnessed for writing the AFM order and detecting its subsequent changes. This necessitates the development of predictive models, disruptive materials, and novel experimental designs. Several research teams are currently investigating the theoretical and experimental aspects of this subject. Examples include reviews on the theory of current-induced torques in metals[5], spin transition in AFM-based spin valves[6], AFM dynamics [7], spin Hall effects in metallic AFMs[8], and manipulation and detection of the magnetic state in an AFM[9,10] .

Indeed, one possible approach is to study the FM-free, purely AFM systems. In such a case one can potentially fully exploit intrinsic properties and the most advantageous features of AFM materials, namely ultra-fast dynamics, and robustness against external magnetic fields. However, in the absence of net magnetization, the read-out of the staggered magnetization or Néel vector is the key obstacle to employing AFM

systems in novel devices[11]. Another possible approach is to benefit from the well-established read-out methods of FMs without serious diminishing the above mentioned AFM advantages, as it has been very recently demonstrated for exchange coupled Py/Mn_2Au FM/AFM system[11].

The investigation of the interaction between AFM and FM thin films in epitaxial multilayer systems and nanostructures is of significant interest in the field of spintronics. The ability to tailor the MA of AFM thin films opens up new opportunities for controlling their magnetic properties and exploring emergent phenomena. This research has the potential to contribute to the development of advanced magnetic devices with enhanced functionality and performance in various technological domains such as data storage, spintronics and magnetic sensing.

2. Chapter two: Magnetism of Thin Films

One of the active areas in modern physics focuses on the exploration of magnetic systems with reduced dimensions, such as surfaces, thin films, multilayers[12], as well as magnetic particles and interacting magnetic nanostructures[13]. The motivation behind this interest stems from the emergence of unique magnetic structures and phenomena in these systems, absent in their bulk counterparts, and the potential for various technological applications[14,15]. Advancements in experimental techniques have enabled precise and controlled fabrication of these systems, allowing for high-sensitivity and spatially-resolved investigations of their magnetic properties, even at the atomic level. Concurrently, advanced theoretical methods and computational tools contribute to simulating and elucidating the underlying magnetic phenomena. Theoretical studies now have the capability to predict novel phenomena and propose experimental investigations of specific systems. The remarkable progress achieved thus far indicates the immense promise of studying low-dimensional magnetism in future research[16].

In this chapter, literature overview concerning thin films static properties will be provided, such as magnetization, magnetic arrangement, and magnetic ordering temperature, with consideration given to film thickness, atomic morphology, temperature, and other factors. A particular emphasis will be placed on investigating the magnetization direction and spontaneous magnetic reorientation observed in various thin film systems. The determination of magnetic arrangements near material interfaces plays a crucial role, whether between a magnetic and nonmagnetic material, two distinct FM layers, or in the vicinity of a FM - AFM interface. When a magnetically ordered system comes into atomic contact with another material, it is natural to expect the emergence of a novel magnetic arrangement near the interface, differing from the bulk configuration. This phenomenon is commonly known as the magnetic proximity effect. Initially studied in the context of a FM in contact with a paramagnet[17], this effect has been extended to many other systems[18,19] including AFM/FM bilayers relevant for this thesis.

Before going to details, it is worth to provide some general observations. Examining the periodic table of elements reveals the intriguing fact that most individual atoms possess a magnetic ground state, whereas the corresponding bulk systems are typically nonmagnetic. As a general rule, the likelihood of a magnetic ground state

increases as the spatial dimensionality of an extended system decreases or as the local symmetry of a specific site in the atomic lattice diminishes. Consequently, magnetic properties are typically more pronounced at the surface of a bulk magnet compared to its interior. In essence, a magnetic ground state arises from electron correlations, such as Hund's rules. Increasing electron mobility or kinetic energy reduces the significance of these correlations, potentially leading to the disappearance of the magnetic ground state. Conversely, magnetic ordering in an extended system, arising from interactions between atomic magnetic moments, requires a certain degree of electrons mobility or overlapping electron wave functions of neighbouring ions. Thus, the presence and structure of magnetism in extended systems depend on the delicate balance between electronic correlations and kinetic energy. The determination of magnetic properties in bulk systems is constrained by a limited selection of pure materials and compounds. Factors such as crystallographic and thermal stability restrict the range of available combinations of constituents. In contrast, the investigation of low-dimensional systems, such as magnetic thin films and interacting magnetic nanostructures, provides a broader range of systems for examination. By experimentally measuring systems with controlled structures and employing theoretical simulations, it becomes possible to comprehensively explore the conditions and boundaries of a magnetic ground state. This analysis can be conducted as a function of numerous parameters, allowing for a detailed understanding of the underlying principles and constraints.

2.1. Magnetic Anisotropy in ferromagnetic low dimensional systems

MA refers to the directional dependence of the magnetization, and it plays a crucial role in determining the stability and switching behaviour of magnetic materials. Experimental observations demonstrate that the magnetization tends to align itself along specific axes within a magnetic material. Deviating from these preferred axes, known as the easy axes, incurs an energy cost.

MA is defined as the energy required to rotate the direction of magnetization from the easy axis to the hard axis[20]. The origin of MAs can stem from various factors, such as the electric field of the solid or crystal, the shape of the magnetic sample, or mechanical strain or stress. These factors are characterized by polar vectors and cannot determine a single direction for the magnetization, which is an axial vector. As a result, there can exist

a unique axis for anisotropy, but not a unique anisotropy direction. Consequently, the energy density, denoted as E_a associated with MA must remain constant when the magnetization is inverted. This requirement implies that E_a is an even function of the angle θ formed by the magnetization vector **M** and the magnetic axes.

The presence of strong easy-axis anisotropy is essential for materials with hard magnetism, while soft magnets require near-zero anisotropy. The energy density, that represents the inclination of magnetization along an easy axis, can be defined as:

$$E_a = K_1 \sin^2\theta + K_2 \sin^4\theta + K_3 \sin^6\theta \ \ldots \quad (2.1)$$

where the coefficients K_i $(i = 1, 2, 3, ..)$ are the anisotropy constants that typically vary from less than 1 $kJ\ m^{-3}$ to over 20 kJm^{-3}. It is worth noting that, in the absence of MA, the ability of 2D objects like thin films to exhibit magnetic ordering, as mentioned earlier, would be non-existent. Similarly, in bulk samples, the magnetization would become entangled in intertwined curls and would be scarcely detectable[21]. This phenomenon occurs because the exchange interaction has a limited range, enabling the magnetization to effortlessly rotate into new directions within a distance known as the magnetic coherence length, resulting in negligible energy costs. It is worth mentioning that the anisotropy is temperature-dependent and approaches zero at the Curie temperature (T_C) in the absence of an applied external magnetic field.

2.1.1. The origin of magnetic anisotropy

The MA has two main sources: the magnetic dipolar interaction and the spin-orbit interaction. The dipolar interaction, with its long-range nature, contributes to the anisotropy and is influenced by the sample's shape. It plays a significant role in thin films, often leading to in-plane magnetization. When the spin-orbit and dipolar interactions are absent, the electron-spin system's total energy becomes independent on the magnetization direction. In a localized perspective, the spins are coupled to the orbits through the spin-orbit interaction, which, in turn, is influenced by the crystal lattice. Itinerant materials experience a small orbital momentum induced by the spin-orbit interaction, resulting in the coupling of the total magnetic moment (spin plus orbital) to

the crystal axes. This dependence on the magnetization orientation relative to the crystalline axes gives rise to the magneto-crystalline contribution to the anisotropy, reflecting the crystal's symmetry.

At interfaces, the lowered symmetry strongly modifies this contribution compared to the bulk, resulting in what is known as interface anisotropy, as recognized by Néel in 1954[22]. Additionally, the spin-orbit interaction, along with the overlap of wavefunctions between neighbouring atoms, is responsible for the magneto-elastic or magneto-strictive anisotropy observed in strained systems. This is particularly relevant in multilayers where adjacent layers exhibit lattice mismatch.

It is worth noting that in thin films, both shape anisotropy and magnetocrystalline anisotropy (MCA) contribute to the general anisotropy of the system. The anisotropy constants K in equation (2.1) can be expressed as the sum of these two contributions. The first term K_D represents the shape anisotropy. The second term K_M corresponds to MCA originating from the atomic structure and bonding within the film. Giving that the first order of the MA energy density in a thin film can be expressed as follows:

$$E_a = (K_D + K_M) \sin^2 \theta + \cdots \qquad (2.2)$$

the balance between K_M and K_D plays a crucial role in thin films and multilayers, and it can be influenced by temperature for example. An interesting case is observed in the Fe/Cu(001) system, where the magnetization transitions from an out-of-plane orientation at low temperatures to the in-plane of the film at around 300 K. Extensive studies have been conducted on this reorientation transition[23].

In applied magnetism, it is particularly intriguing that thin films within layered structures (as well as certain ordered alloys) may exhibit an easy axis perpendicular to the sample surface. In isolated thin films, the magnetization typically lies in the plane due to the influence of shape anisotropy. However, in specific sandwich structures, the magnetization prefers an out-of-plane orientation. This perpendicular MA holds significant technological importance and serves as a remarkable example of the interplay between the two anisotropy mechanisms in determining the easy axis.

2.1.1.1. Shape anisotropy

The distribution of magnetization within atomic cells comprises contributions from both spin and orbital effects, and it deviates from a spherical shape as it involves various multipoles[24]. When expanding the spin density into multipole terms, the dominant term, upon integrating over the atomic volume, corresponds to the magnetic spin moment. The spin moment, originating from the exchange interaction, is inherently isotropic, and MA arises solely from the preferred dipolar coupling between atomic moments. Consequently, the dipole-dipole interaction between magnetic moments, represented by m_s, positioned at the atomic locations within the lattice can be expressed:

$$E_{dipole-dipole} = -\frac{\mu_0}{4\pi}\sum_{i\neq j}\frac{1}{r_{ij}^3}\left[m_i \cdot m_j - 3\frac{(r_{ij}\cdot m_i)(r_{ij}\cdot m_j)}{r_{ij}^2}\right] \quad (2.3)$$

The summation is performed over all atomic dipoles m_i and m_j, where their absolute values correspond to the spin moment m_s. Each pair of dipoles is considered only once, and $\boldsymbol{r_{ij}}$ represents the vector connecting the two moments (see Fig. 2.1). The subsequent term in the multipole expansion, the quadrupole term, captures the lowest-order anisotropic spin distribution within the atomic cell. This term introduces the intra-atomic magnetic dipole moment. Additionally, the magnetization density within the atomic volume is influenced by the orbital moment, which contributes to its anisotropy represented by m. Typically, the anisotropy of the orbital moment is comparable to that of the intra-atomic magnetic dipole moment. However, in practice, both contributions are significantly smaller than the lowest-order magnetic dipole-dipole interaction described by (2.3) formula.

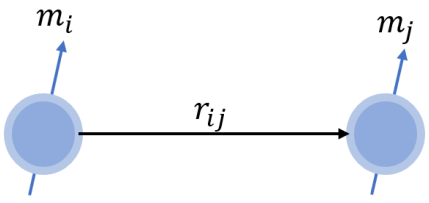

Fig. 2.1 Representation of two neighbouring magnetic moments m_i and m_j

Considering that all moments are parallel due to the dominant exchange interaction, the dipole-dipole energy between two magnetic dipoles is minimized when both atomic moments align parallel to the internuclear axis.

In thin films, the internuclear axes tend to align preferentially within the plane of the sample. As a result, the dipole energy is minimized when the magnetic moment is oriented in the plane. In the case of bulk materials, the dipolar field can be separated into three components. The first component, E_S, corresponds to the contributions from atomic dipoles within a spherical volume, located on the lattice sites. The second component, E_L, arises from pseudo-charges on the surface of the sphere. The third component, E_D, is a macroscopic contribution originating from the demagnetizing field caused by pseudo-charges on the external surface of the sample.

$$E_{dipole-dipole} = E_S + E_L + E_D \quad (2.4)$$

It is important to note that the dominant term, E_D, solely originates from the demagnetizing field, and is responsible for the shape anisotropy[20].

2.1.1.2. Magneto-crystalline anisotropy

The microscopic origins of MA in transition metals have been the subject of ongoing debate since the pioneering work by Van Vleck in 1937[25]. Many interests in this topic have been reignited with the advent of artificially engineered transition metal films and multilayers that exhibit perpendicular MA[26,27]. However, understanding the microscopic mechanisms behind MCA remains challenging, often leading to general hand-waving arguments[26,28]. The difficulties arise from the treatment of spin-orbit interactions in transition metals and their compounds, which possess small sizes. Consequently, MCA is typically characterized by small energy values. For instance, it was possible to accurately determine the known [111] anisotropy direction in bulk fcc Ni[29], where the MCA is approximately 10^{-5} eV/atom due to the high symmetry of the lattice. As a result, developing a conceptual understanding of the MCA's origin remains elusive, as it emerges from the intricacies of the band structure.

In general, MCA can be defined as follows: MCA represents the energy required to rotate the magnetization from the "easy" direction to the "hard" direction in a bulk sample, assuming the absence of magnetostatic effects. It is determined by the anisotropy of the spin-orbit energy, whereby the rotation of the magnetization into the hard direction entails an energy cost.

In practical applications MCA (described in (2.2) by K_M) is often treated as an empirical constant, which is typically determined through measurements such as FM resonance or magnetization curves obtained along the hard axis. Historically, MCA and magneto-elastic anisotropy have been regarded as distinct phenomena. However, on a microscopic level, both of these anisotropies arise from the same underlying mechanism, namely the anisotropy of atomic structure and bonding in conjunction with the spin-orbit interaction. Therefore, both anisotropies are discussed under the general term MCA. The concept of MCA was initially proposed by Van Vleck[30], who attributed it to the spin-orbit interaction that couples the isotropic spin moment to an anisotropic lattice. In modern electronic structure calculations, the MCA energy is associated with the largest difference in spin-orbit energy when the material is magnetized along two distinct crystallographic directions. In the absence of shape anisotropy effects, these two directions define the "hard" and "easy" magnetization directions[20].

2.1.1.3. Surface anisotropy

Van Vleck's concept suggests that MA arises from spin-orbit coupling and is influenced by the preferred "easy" axis created by the bulk lattice[30]. On the other hand, Néel proposed in 1954 that surface or interface anisotropy arises due to the reduced symmetry at the surface or interface, which creates a significant difference in MA between the surface and bulk of FM materials[22].

For a considerable time period, it remained uncertain whether a few-layer-thick film of a material like Fe, which possesses weak bulk anisotropies, could exhibit sufficient surface-induced perpendicular anisotropy to overcome shape anisotropy and result in perpendicular magnetization. Further advancements have revealed that surface or interface-induced perpendicular MA is indeed possible. The realization of this effect relied on the development of techniques for producing atomically clean epitaxial metallic

films on single crystal metallic substrates. This was initially deemed challenging due to the higher interdiffusion rates of metals compared to insulators and semiconductors[22,30].

The magnetic properties of surface atoms differ from those of bulk atoms due to the reduced symmetry at the surface. This difference in magnetic behaviour is known as Néel-type surface anisotropy[22,31]. Surface/interface anisotropy plays a crucial role in systems where surface properties dominate, especially in films consisting of only a few atomic layers (AL). Importantly, the magnitude of surface anisotropy remains constant regardless of film thickness, as long as variations in thickness do not induce structural or morphological changes at the interface layer. However, the commonly used separation of effective anisotropy (K_{ef}) into volume (K_V) and surface (K_S) terms mask the inherent nature of Néel-type surface anisotropy. This separation can be expressed by (2.5):

$$K_{ef} = K_V + 2K_S/d \tag{2.5}$$

where d represents the film thickness[32–34]. It has to be noted that this approach does not always accurately represents the physics of surface anisotropy. True surface/interface anisotropy contributes a constant term to the MA, which may depend on film thickness. Therefore, assuming that an anisotropy contribution scales with d^{-1} does not necessarily indicate a genuine Néel-type surface anisotropy[35].

It is often assumed[33] that film strain varies inversely with film thickness (d^{-1}), and this contribution was in some cases mistakenly attributed to surface anisotropy. However, some experimental measurements challenge this assumption[36], as they do not demonstrate a d^{-1} variation in film strain. Thus, the general applicability of a d^{-1} strain variation for epitaxial films is questionable. Additionally, the separation of MA into volume and surface terms becomes inappropriate for extremely thin films, such as several monolayers, where separating the sample into bulk and two surfaces is not suitable. Furthermore, the apparent thickness dependence of magnetoelastic anisotropy contributions can be misinterpreted as surface anisotropy. Surface contributions to MA, as proposed by Néel, can indeed dominate the overall MA. Examples include the reorientation of easy magnetization direction in Ni monolayers induced by hydrogen or iron, highlighting the crucial role of adsorbate coverage in determining the MA of FM monolayers[36].

2.1.2. In-plane magnetic anisotropy of Fe(110) films on W(110)

In most cases, the in-plane MA of thin films is considerably weaker compared to the out-of-plane anisotropy. However, there are certain exceptions, particularly in thin film systems that possess lower surface symmetries than square or hexagonal structures. An example of such an exception can be found in epitaxial (110) oriented iron films on tungsten W(110) single crystal surface[37]. In the following part of this chapter the in-plane MA and associated in-plane to in-plane spin reorientation transition in Fe/W(110) system will be described in detail as all experimental results presented in chapters four, five, and six concern AFM films grown on Fe(110)/W(110). As a matter of fact, the well-defined and controllable MA and spin reorientation transition (SRT) in Fe(110) layers was used as a tool to modify the MA or magnetic state of AFM overlayers, as it will be shown by results presented in chapters four, five, and six.

The absence of out-of-plane anisotropy in Fe(110) can be attributed to the crystallographic symmetry of the surface. The arrangement of atoms and the resulting symmetry prevent the existence of preferred orientations for the magnetic moments perpendicular to the plane. Essentially, the crystal symmetry of Fe(110) does not exhibit any specific preference for a particular magnetic alignment in the direction perpendicular to the surface[37]. In the standard series expansion of bulk MCAs in cubic crystals, terms of less than fourth order vanish when expressed in terms of directional cosines with respect to the cubic axes. The first nonvanishing term is given by $K_1(\alpha_1^2\alpha_2^2 + \alpha_2^2\alpha_3^2 + \alpha_3^2\alpha_1^2)$. However, for surface energy, lower order terms can exist due to the reduced symmetry at the surface. This was initially observed by Néel[22], who demonstrated that the dominant contribution, known as the out-of-plane anisotropy, is determined by the orientation of the spontaneous magnetization relative to the surface normal. Néel established a connection between magnetic surface anisotropies and bulk magnetoelastic properties through a phenomenological pair-bonding model.

The energy density of the bulk MCA in cubic crystals:

$$E_{bulk} = K_1(\alpha_1^2\alpha_2^2 + \alpha_2^2\alpha_3^2 + \alpha_3^2\alpha_1^2) \qquad (2.6)$$

can be in case of perfectly in-plane Fe(110) system expressed as:

$$E_{bulk} = \left(\frac{K_1}{4}\right) \cdot (\sin^2 2\theta + \sin^4 \theta) \tag{2.7}$$

where θ is the in-plane magnetization angle (See Fig 2.2). The contribution to the surface energy σ for in-plane magnetization **M** is given by:

$$\sigma = -K_{S,P} \sin^2 \theta, \tag{2.8}$$

where $K_{S,P}$ is the anisotropy constant for the in-plane anisotropy. With the assumption of homogeneous magnetization with an in-plane magnetization vector **M**, the total free energy per unit volume (E/V) for a film with a thickness d can be expressed as:

$$E/V = E_{bulk} + \left(\frac{1}{d}\right) \cdot (\sigma^{(1)} + \sigma^{(2)}) \tag{2.9}$$

which means:

$$E/V = \frac{K_1}{4} (\sin^2 2\theta + \sin^4 \theta) - \left(\frac{1}{d}\right) \left(K_{S,P}{}^{(1)} + K_{S,P}{}^{(2)}\right) \cdot \sin^2 \theta \tag{2.10}$$

where $\sigma^{(1)}$, $\sigma^{(2)}$, $K_{S,P}{}^{(1)}$, and $K_{S,P}{}^{(2)}$ refer to both surfaces of the thin film.

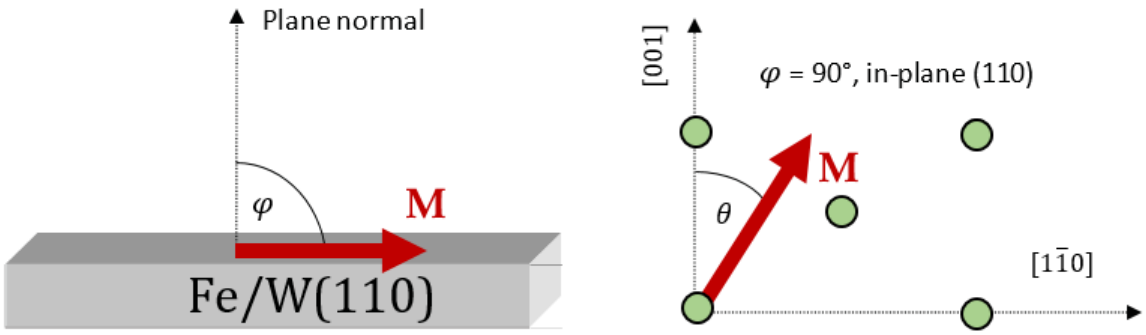

Fig. 2.2 The definition of the polar angle (φ), and the in-plane angle of magnetization (θ) in Fe(110) on W(110).

2.1.2.1. Thickness-driven SRT in Fe(110)

In case of Fe(110) when $K_1 > 0$ and ${K_{S,P}}^{(i)} > 0$ and for the critical thickness (d_c), anisotropy energies for both orientations $\theta = 0°$ and $\theta = 90°$ are equal, which means:

$$d_c = \left({}^{4}/_{K_1}\right) \cdot \left({K_{S,P}}^{(1)} + {K_{S,P}}^{(2)}\right) \tag{2.11}$$

For a symmetric film, ${K_{S,P}}^{(1)} = {K_{S,P}}^{(2)} = K_{S,P}$, and the equation (2.11) can be expresses as:

$$d_c = \left({}^{8}/_{K_1}\right) \cdot K_{S,P} \tag{2.12}$$

This means, that with increasing thickness, at the critical thickness d_c, the magnetic moments spontaneously switch from $[1\bar{1}0]$ to [001] direction, as schematically presented in Fig. 2.3 (a). In other words, at the critical thickness, it takes no energy to switch the magnetic moments from [001] to $[1\bar{1}0]$ and vice versa.

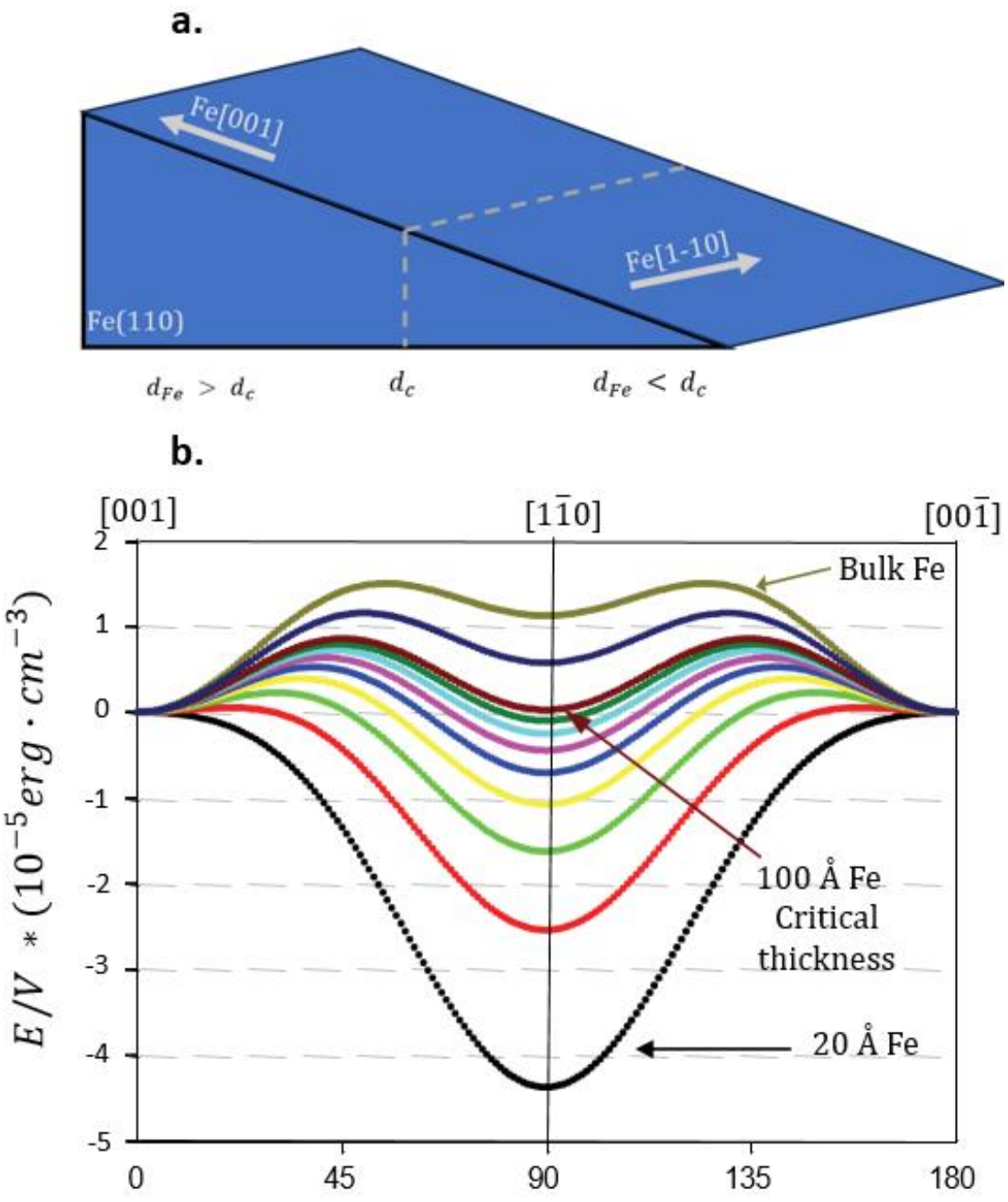

Fig. 2.3 (a) Schematic representation of the SRT thickness dependence in a wedged Fe(110) thin film. (b) Simulation of the in-plane MA energy as a function of the angle Θ for various thicknesses of the Fe(110) thin layers. The assumed values of the surface and the volume anisotropy constants are K_1 =

$4.5 \cdot 10^5\ (erg \cdot cm^{-3})$, $K_{S,P}{}^{(i)} = 0.11\ (erg \cdot cm^{-2})$ for several thicknesses. Simulation data is taken from the reference [38].

Fig. 2.3 (b) presents a simulation of energy per unit volume given by 2.10 formula assuming particular set of MA constants for increasing thicknesses of Fe(110). As can be seen in Fig. 2.3, with increasing thickness of Fe layer, the global minimum of energy initially present for Θ = 90° (so along $[1\bar{1}0]$ in-plane direction) above some critical thickness (here ~100Å) becomes to be only a local minimum. For thicker Fe films the global minimum of energy is for Θ = 0° (so along [001] direction) and thus around ~100 Å one expects thickness induced in-plane to in-plane reorientation transition. Obviously, another set of MA constants would result in different critical SRT thickness. For instance, assuming the same K_1 and increasing the $K_{S,P}$ value will shift the SRT to higher Fe thicknesses. This can be interpreted by increased surface contribution which makes the magnetization of even relatively thick Fe films oriented along $[1\bar{1}0]$ direction, i.e., orthogonally to [001] bulk easy axis of Fe. The same effect was realized experimentally for example by annealing of the Fe films on W(110) which makes the surface smoother as compared to as grown films and thus increases the surface contribution to MA. As a result, the critical thickness of the SRT increases as well.[39]

Baek et al. investigated the reorientation of magnetization in pure Fe(110) films and explored how this reorientation could be modified using noble-metal overlayers, specifically Ag and Au[40].

In the case of pure Fe(110) films, the researchers grew an epitaxial Fe wedge film on a W(110) crystal with varying thicknesses. They observed that thinner films exhibited magnetization along the $[1\bar{1}0]$ direction, while thicker films displayed magnetization along the [001] direction. The critical thickness for this transition was found to be between 85 Å and 86 Å. Notably, the transition from one magnetization direction to another was exceptionally sharp, occurring within approximately 1 monolayer (ML) of thickness change. Furthermore, they concluded the coexistence of both $[1\bar{1}0]$ and [001] domains during the reorientation transition. This transition was attributed to a delicate balance between surface anisotropy, favouring the $[1\bar{1}0]$ direction, and bulk anisotropy, favouring the [001] direction. It was highlighted that in 3d metals like Fe, the bulk MCA is considerably smaller than surface anisotropy, explaining the relatively high critical thickness required for in-plane to in-plane reorientation. Authors analysed the

photoemission spectra measured along the two chosen in-plane orientations, namely [1$\bar{1}$0] and [001]. The results are shown in Fig. 2.4 (a). One can notice that the sum of the two spin polarizations remains almost constant across the transition region. Basing on this observation authors concluded that both [1$\bar{1}$0] and [001] domains coexist during the reorientation transition.

The study then explored the influence of noble-metal overlayers, Ag and Au, on the Fe reorientation. Both Ag and Au overlayers were found to reduce the critical thickness for the reorientation transition compared to pure Fe(110). Ag, which grew epitaxially on Fe(110), showed a linear decrease in the transition thickness, reaching about 70% of the clean Fe(110) surface value after ~2 ML of Ag, after which it saturated at higher coverage, as demonstrated in Fig. 2.4 (b). In case of Au overlayers a much more pronounced decrease in the transition thickness was observed and partially attributed to its stronger electronic interaction with Fe. Unlike Ag, Au did not exhibit saturation in its effect on the transition thickness. It should be underlined that such drastic influence of Au overlayer on SRT critical thickness can be observed only in case of as deposited, grown at room temperature (RT) Au overlayers. Post-preparation annealing of the Au/Fe bilayers makes the effect much smaller as it will be shown in chapter 6 of this thesis.

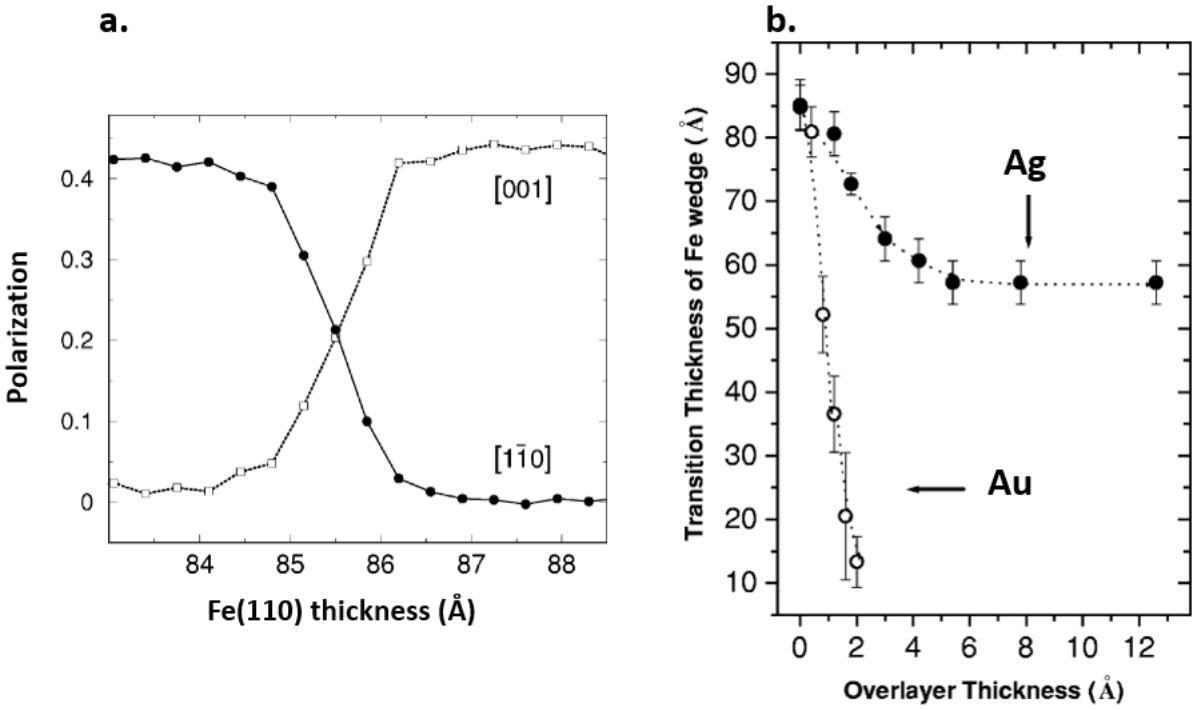

Fig. 2.4 (a) Secondary electron spin-polarization as a function of Fe(110) thickness. (b) Critical Fe thickness of SRT as a function of overlayer thickness for two studied cases, Ag and Au. These results are taken from reference.[40]

2.1.2.2. Temperature-driven SRT in Fe(110)

Over the past years, there has been significant interest in reorientation transitions driven by temperature[41–43]. The anisotropy-flow concept has been employed to explain the general characteristics of these transitions[44]. However, most of these studies primarily focus on reorientations from out-of-plane to in-plane orientations, as they rely on the understanding that higher temperatures favour in-plane reorientation due to increased entropy.

Concerning in-plane to in-plane SRTs, Fruchart et al.[41] observed a 90°, temperature induced switching of the magnetization in Fe(110) from $[1\bar{1}0]$ to [001] (see Fig. 2.5) in epitaxial W/Fe/W trilayers.

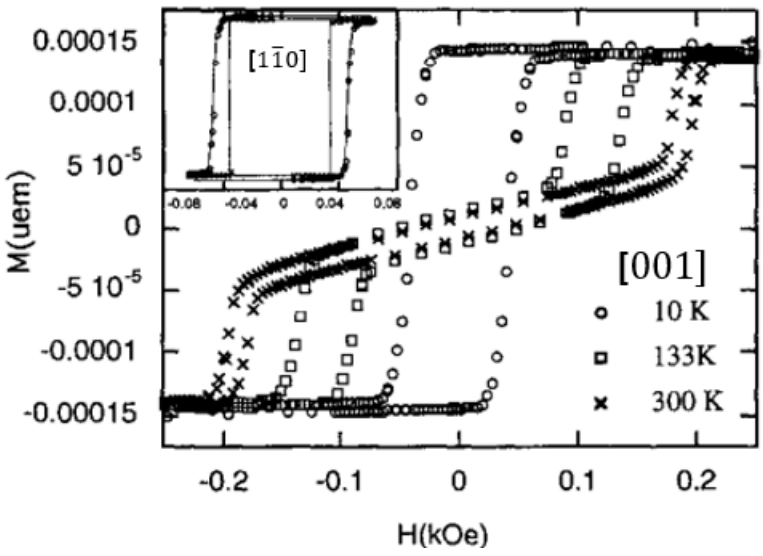

Fig. 2.5 MOKE results obtained for W(500 Å)/Fe(60 Å)/W(500 Å) system at different temperatures showing a clear temperature-driven SRT. Data taken from reference[41].

In Fig. 2.5, and at 300 K, Fruchart et al. found that $[1\bar{1}0]$ was the easy axis for 60 Å Fe(110), and [001] axis had a typical hard loop. However, decreasing the temperature of

the measurement to 10 K has induced a 90° switching in the magnetization making [001] an easy axis as documented by the typical square-like magnetic hysteresis loop plotted in Fig. 2.5 with open dots.

Gerhardter et al.[45] investigated the temperature dependence of the in-plane anisotropy for Fe(110) thin films grown on W(110). They have found that the anisotropies of a sample of 130 Å Fe grown at 300K (with a critical thickness below 100 Å) exhibit different anisotropy behaviour compared to a sample of 200 Å Fe grown at 600K, which they have explained as a result of the influence of the substrate temperature during the evaporation. Fig. 2.6 shows the temperature dependence of the K_{ef} anisotropy for several Fe(110) samples[45]. Note that the sample with d_{Fe} = 200 Å switches with increasing the temperature from [001] to [1$\bar{1}$0] due to the different temperature dependencies of the surface and the volume magnetic anisotropies, which means that temperature-driven SRT is observed.

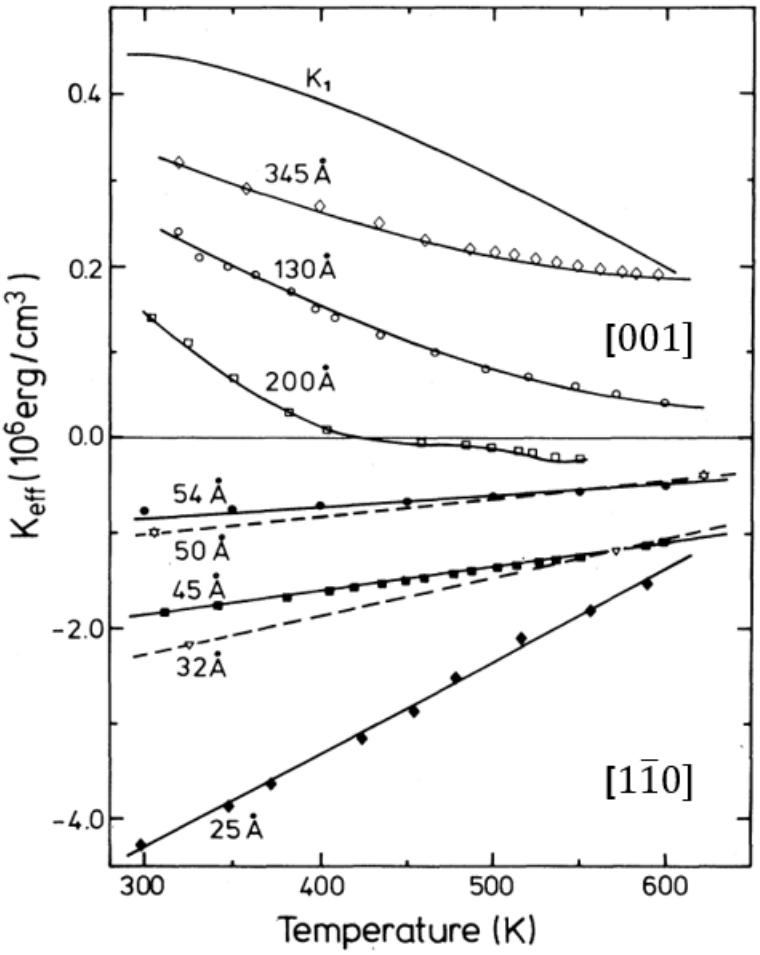

Fig. 2.6 Effective in-plane anisotropy of Fe(110) as a function of temperature. Results taken from reference[45].

Since temperature change also affects other aforementioned factors (changes in surface morphology, adsorption/desorption of residual gases), it is difficult to separate the actual influence of temperature from indirect effects. However, providing the critical temperature of SRT is low (preferably below or close to 300 K) the unwanted temperature induced changes in surface structure and morphology can be omitted. Similarly, in case of capped Fe films the adsorption induced effects are excluded and so a true temperature induced SRT can be triggered and followed, like it will be shown in chapter four for NiO(111)/Fe(110) bilayers.

2.2. Magnetic properties of antiferromagnetic thin films

AFM materials exhibit a unique magnetic behaviour where adjacent magnetic moments align antiparallel to each other. These materials consist of two interpenetrating sublattices of magnetic ions. By observing the temperature dependency of the magnetic susceptibility for AFM, one can determine T_N, the temperature above which AFM materials become paramagnetic (See Fig 2.7). Below the T_N, one sublattice becomes spontaneously magnetized, while the other sublattice magnetizes in the opposite direction. As a result, AFM materials lack net spontaneous magnetization and exhibit linear magnetization responses to external fields, akin to paramagnetic materials.

In the early 1930s, pioneering work by Louis Néel laid the foundation for the discovery of antiferromagnetism. Néel proposed that in some materials, adjacent magnetic moments could align antiparallel to each other, resulting in a cancellation of the overall magnetic moment. This groundbreaking idea challenged the conventional understanding of magnetic order. The first direct proof of AFM ordering came in 1949 from Shull and Smart's neutron diffraction of manganese oxide, MnO[46]. This experiment revealed that the spins on Mn^{2+} ions are split into two sets, oriented antiparallel to each other. Before this discovery, the primary evidence for antiferromagnetism relied on the correlation between the observed temperature-dependent susceptibility and theoretical predictions using the Curie-Weiss theory.

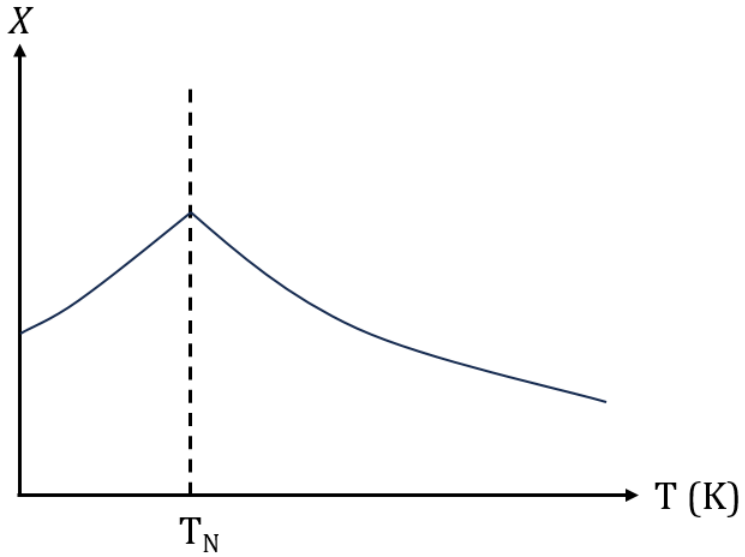

Fig 2.7 Diagram shows the magnetic susceptibility as a function of temperature for a typical AFM. The temperature at which the magnetic susceptibility drastically changes is T_N.

Over the past couple of decades, the availability of highly sensitive experimental techniques for studying magnetic properties has sparked a considerable amount of research focused on AFM in low-dimensional systems. These systems typically consist of small particles or films deposited on nonmagnetic or FM substrates. Similar to well-known FM materials, confined AFM systems exhibit magnetic properties that can deviate significantly from bulk properties due to interface or size effects[47]. These effects range from the stabilization of unconventional AFM ordering to the emergence of uniaxial anisotropy in low-dimensional AFM samples. Moreover, the study of AFM-FM interfaces unveils a rich phenomenology associated with interface exchange coupling[48].

In systems with strong electronic correlations, such as AFM oxides, which possess very short correlation lengths, intrinsic finite-size effects can be observed only in ultrathin films or nanoparticles. Additionally, "surface-related" finite-size effects can arise due to the interplay between properties of atoms at the core of a particle or layer and those at the surface, which can be influenced by reduced coordination. For example, as mentioned in sec. 2.1.1., surface spins often exhibit higher MCA compared to spins within the bulk due to symmetry reduction. In addition, structural or chemical effects can also emerge from phenomena like surface segregation, relaxation, or reconstruction. Furthermore, the surrounding environment can significantly modify the properties of interface atoms through hybridization, strain, or chemical interdiffusion[48]. All these

factors play a crucial role in determining the magnetism of systems containing an AFM film.

2.2.1. Metal oxide AFM films

Given the intricate interplay between magnetic, chemical, structural, and morphological features, the preparation and characterization of high-quality samples are essential in the study of low-dimensional systems. AFM monoxides are often favoured in these studies. They can be grown as high-quality thin films on suitable substrates, exhibit high chemical and mechanical stability, and have relatively high AFM ordering temperatures The proximity of T_N to RT in the case of CoO is advantageous for creating exchange-biased systems. However, from the point of view of most of the applications the higher the T_N is, the more desired material is, which makes NiO (but also other AFM materials, like for example Mn_2Au) advantageous and intensively studied. Another significant aspect of AFM monoxides is their insulating nature[49]. AFM oxides are insulators due to strong electronic correlations and have magnetic properties arising from short-range super exchange interactions mediated by oxygen bonds.

Consequently, from a magnetic standpoint, AFM monoxides can be effectively described within the framework of the Heisenberg or Ising formalism as ensembles of well-localized spins interacting primarily with their nearest neighbours[48].

Two metal oxide AFM materials studied in this thesis are NiO and CoO. Bulk NiO and CoO crystallize in a cubic NaCl structure. Below the T_N (T_N^{NiO} = 523 K and T_N^{CoO} = 291 K respectively for NiO and CoO), the magnetic moments of Ni^{2+}(Co^{2+}) ions in NiO(CoO) align ferromagnetically within the (111) planes, while the adjacent (111) planes are coupled antiferromagnetically. In ultrathin layers, the NiO(CoO) spin direction can be modified by strain induced by the substrate. Previous studies have shown that compressive strain imposes an in-plane NiO(CoO) spin direction, while out-of-plane spin alignment is preferred for AFM grown under tensile strain[50]. In case of NiO, a contraction of the cubic unit cell along the stacking directions of the ferromagnetic planes reduces the crystallographic symmetry and consequently each of the four possible $< 111 >$ directions define a so called “twin domain” (T). Another small contraction along the spin

direction results in three possible $< 11\bar{2} >$ spin directions within each T domain and defines the so called "spin domains" (S). To conclude a total of 12 orientational domains are allowed in NiO, as summarized in Table I.

S	T			
	$T_1[\,1,1,1\,]$	$T_2[\,1,1,\bar{1}\,]$	$T_3[\,1,\bar{1},1\,]$	$T_4[\,\bar{1},1,1\,]$
S1	$[\,1,1,\bar{2}\,]$	$[\,1,1,2\,]$	$[\,1,2,1\,]$	$[\,2,1,1\,]$
S2	$[\,\bar{2},1,1\,]$	$[\,1,\bar{2},\bar{1}\,]$	$[\,\bar{2},\bar{1},1\,]$	$[\,\bar{1},1,\bar{2}\,]$
S3	$[\,1,\bar{2},1\,]$	$[\,\bar{2},1,\bar{1}\,]$	$[\,1,\bar{1},\bar{2}\,]$	$[\,\bar{1},\bar{2},1\,]$

Table I. Crystallographic directions of the S and T domains in NiO. Top row: stacking direction of ferromagnetic Ni^{2+} planes in the four T domains. Following rows: spin direction in the 12 orientational domains.

2.2.2. Finite size effects in antiferromagnetic materials

One of the most known and often reported example of finite size effects in both ferro- and antiferro-magnetic low-dimensional systems is a reduction of the critical magnetic ordering temperature, T_{order}, where T_{order} is the T_C in case of FMs, and T_N in AFM systems. Such reduction can be understood as the system gradually approaching the conditions dictated by the Mermin-Wagner theorem as its size diminishes. As per this theorem, one- (1D) and two-dimensional (2D) systems with short-range interactions cannot exhibit spontaneous breaking of continuous symmetry at finite temperature, which in other words means that certain long-range orderings, like crystalline order, ferromagnetism and importantly antiferromagnetism cannot occur at absolute temperature $T > 0$ [48,51].

Experimental investigations have provided substantial evidence of significant reductions in the magnetic transition temperature T_N across various low-dimensional AFM oxide systems[48,52].

In a simplified mean-field approach, which assumes T_{order} to be proportionate to the exchange energy density of the particle or thin film, the decrease in the magnetic transition temperature stems from the diminished total exchange energy resulting from

a smaller number of neighbouring atoms. However, it is important to take into account that the system's surroundings are not passive and can contribute to the overall exchange energy. For instance, the environment (substrate, neighbouring, covering or buffer layers, etc.) may induce surface MA through a strain field or modify the magnitude and coupling strength of interface moments via hybridization effects or other interactions. The mean-field model states that the change in T_{order} relative to the bulk value, $T_{order}(\infty)$, is inversely proportional to the size or thickness (d) of the particle or film. Nevertheless, experimental findings do not entirely support this prediction, and the size-dependent reduction in T_{order} finds better explanation through scaling theories[53].

According to scaling theories, the correlation length of fluctuations in the AFM order parameter logarithmically diverges as the reduced temperature $(T - T_{order})/T_{order}$ approaches zero in the vicinity of the magnetic ordering transition T_{order}. In the case of a system where the size d significantly exceeds a characteristic length ξ that characterizes the spatial range of spin-spin interactions, one observes a gradual reduction in T_{order} that adheres to a power-law relationship [54]:

$$\frac{T_{order}(\infty) - T_{order}(d)}{T_{order}(\infty)} = \left(\frac{\xi + a}{2d}\right)^{\lambda} \tag{2.13}$$

here, λ is a constant, and (a) corresponds to the lattice spacing. Since $d \ll \xi$, T_{order} is expected to exhibit a linear variation with d [54]:

$$T_{order}(d) = T_{order}(\infty)\ \frac{d-a}{2\xi} \tag{2.14}$$

The specific relationship between T_{order} and d exhibits variations across different experimental systems, highlighting the substantial influence of environmental factors[48].

2.3. Magnetic control of AFM anisotropy: Interface FM/AFM exchange coupling

The efficient manipulation of AFM states has become crucial for future advancements[10]. To address this challenge, research efforts have focused on (i) magnetic, (ii) electrical, (iii) strain, (iv) and optical manipulation methods[55,56]. The main approach, which will be discussed in this work, is the magnetic control.

Song et al. studied the techniques for influencing the orientation of magnetic moments, a well-established practice traditionally associated with the use of magnetic fields, primarily in the context of FM materials[55]. However, when it comes to AFMs, this undertaking presents a more formidable challenge, primarily due to the inherent negligible Zeeman energy effect[10]. Specifically[5,54,55], one avenue involves the application of an external magnetic field that surpasses a defined threshold, albeit demanding the use of a considerably robust magnetic field to achieve the alignment of magnetic moments or domains. For instance, in the case of NiO(111) single crystals, this alignment necessitates a magnetic field of 9 T to orient the magnetic moments perpendicular to the field's direction, a result of Zeeman energy reduction, coupled with contributions from MA or domain formation induced by magnetostriction[57]. Likewise, for the Mn_2Au AFM, achieving a favoured orientation of AFM moments demands an in-plane magnetic field of approximately 70 T[58].

Additionally, C. Song et al. explored the application of exchange bias as a more universally applicable approach for manipulating the magnetic moments of AFMs when they are coupled with FM materials. This approach necessitates a smaller magnetic field to exert control. The discovery of exchange bias, attributed to Meiklejohn and Bean in 1956[59], marked the inception of extensive research in this domain over subsequent decades. The manifestation of exchange bias becomes evident in the magnetic hysteresis loop, characterized by a pronounced shift in its centre along the horizontal axis. This shift arises from the interfacial interplay between FM and AFM neighbouring components as the system is cooled below their respective ordering temperatures T_C and T_N[60]. The exchange bias effect will be described in the following 2.3.1 section.

2.3.1. Exchange bias

In the P.K. Manna and S.M. Yusuf review, authors focus on the exchange bias effect[61], a magnetic phenomenon known as unidirectional or exchange anisotropy. This phenomenon arises due to the interaction at the interface between a FM material and an AFM material[62,63]. The study identifies key indicators of the exchange bias effect, including the shift of the field-cooled (FC) hysteresis loop along the magnetic field axis in magnetic field-dependent DC-magnetization studies, an increase in coercivity observed in FC-hysteresis compared to zero field-cooled (ZFC) cases, and a training effect, where the exchange bias field gradually decreases as the number of loop cycles (n) increases in cyclic hysteresis loop studies. Additionally, the study notes other characteristics of the exchange bias effect, including unidirectional anisotropies[62,63], asymmetric reversal of hysteresis loops[64,65], and a vertical shift of the FC hysteresis loop along the magnetization axis[66,67]. The origin of these effects lies in the interface between two magnetically ordered systems, such as FM and AFM materials.

The phenomenological model of the exchange bias mechanism is based on the microscopic spin configuration at an AFM/FM interface. Fig. 2.8 illustrates the simplest phenomenological origin of a shifted hysteresis loop observed in a magnetization study for an exchange-coupled AFM/FM system. The model considers a FM in close proximity to an AFM at temperature of measurement (T), with the AFM having a relatively large MCA. Additionally, T_c of the FM greater than T_N of the AFM ($T_C > T_N$) is assumed.

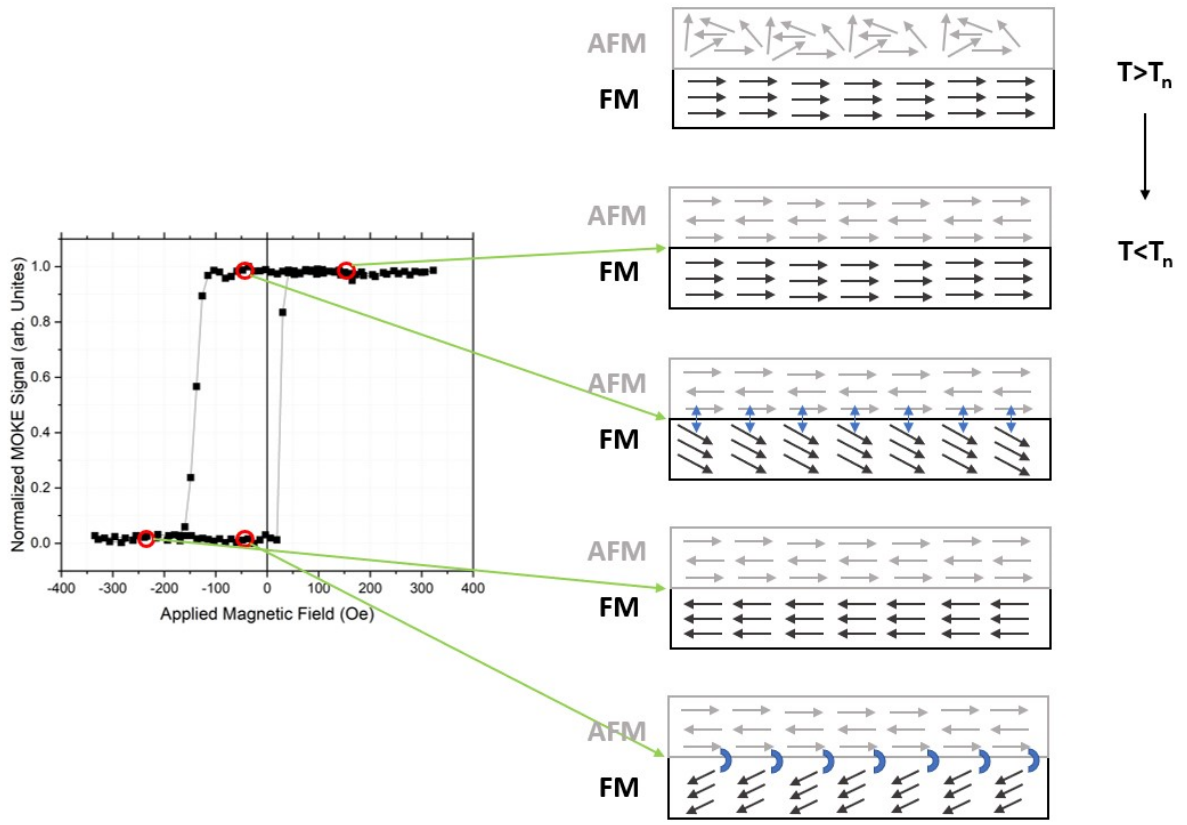

Fig. 2.8 Illustration of the spin arrangement and exchange bias of a bilayer consisting of a FM and an AFM at various stages of an exemplary exchange-biased hysteresis loop.

At a temperature T, where $T > T_N$, the FM spins align themselves with an externally applied magnetic field ($\boldsymbol{H}$), while the AFM spins, which is in a paramagnetic state, remain randomly oriented. A hysteresis curve measured at this temperature (not shown) remains symmetric with respect to zero field axis, unaffected by the proximity of the AFM. Let's assume a high enough magnetic field is applied (along the positive X-axis) in order to saturate the FM. Without changing the magnetic field direction, the AFM/FM system is cooled to a temperature below the T_N of the AFM, following a procedure known as field cooling. For simplicity, type-II AFM ordering is also assumed which means that AFM consists of FM planes that are coupled antiferromagnetically. As a result of the exchange interaction at the AFM/FM interface, the first AL of the AFM aligns either parallel (in case of FM interfacial coupling assumed in the present discussion) or antiparallel (AFM coupling) to the FM spins. Consequently, due to AFM ordering within AFM layer, the spins of the second and subsequent ALs alternate between antiparallel and parallel alignment with respect to the first FM plane of AFM.

The basic assumption of this model is that the FM and AFM exist in a single domain state, and the interface spins of the AFM (first monolayer) are uncompensated. When the magnetic field direction is reversed (positive to negative), the FM spins attempt to realign themselves accordingly. However, due to the interface coupling between the FM and the AFM, it requires additional Zeeman energy to rotate the FM spins as the AFM layer tends to keep the FM magnetization oriented along the positive magnetic field direction. Consequently, the left coercive field (negative magnetic field) increases. Upon complete reversal of all FM spins, a negative saturation magnetization is obtained. When returning from negative to positive magnetic field, the FM spins require less Zeeman energy to return to their initial configuration because AFM layer still prefers the positive field direction and, in this case, supports the external magnetic field in reorientation of FM magnetization. The overall result is a shift of the field-cooled hysteresis loop along the magnetic field axis. If the shift occurs towards the negative magnetic field axis after the FC procedure with a positive magnetic field, it is referred to as the negative exchange bias phenomenon, this case is the most often reported one. Conversely, if for the same FC procedure, the shift occurs along the positive magnetic field axis, it is called the positive exchange bias phenomenon. The magnitude of the shift, measured from the origin of the magnetic field axis, defines the value of the exchange bias field (H_{EB}).

It is worth mentioning that the aforementioned phenomenological description represents the simplest model for understanding the exchange bias phenomenon. Recent reports[68,69] have identified two types of uncompensated AFM spins: pinned (frozen) and unpinned (rotatable)[70–72]. Pinned spins are tightly locked to the AFM lattice and remain fixed under an external magnetic field. Unpinned spins, on the other hand, follow the magnetization of the FM layer and can rotate accordingly. The presence of pinned and unpinned uncompensated AFM spins contributes to the shift of the field-cooled hysteresis loop and the enhancement of coercivity, respectively[70,71,73,74]. Ohldag et al. discusses the observation of uncompensated spins at the interfaces of various exchange bias sandwiches, such as NiO/Co, IrMn/Co, and PtMn/$Co_{90}Fe_{10}$[73]. Previous studies had suggested the presence of pinned spins in certain systems, but a quantitative correlation between pinned magnetization and macroscopic exchange bias fields had not been established. The authors employed high-sensitivity x-ray magnetic circular dichroism (XMCD) spectroscopy to investigate the presence of uncompensated spins and their behaviour in these systems. They found that only a small fraction of the

interfacial spins, approximately 4% of a monolayer, were tightly pinned to the AFM and did not rotate in an external field. The amount of pinned interfacial magnetization was found to be quantitatively correlated with the macroscopic exchange bias field. The study also provided insights into the role of domain walls and contributions from deeper layers in the AFM. The exact origin of the pinned spins remains unclear, but they are speculated to be located at grain boundaries within the polycrystalline films. The findings contribute to a better understanding of the microscopic mechanisms underlying exchange bias phenomena.

2.3.2. Interfacial coupling scenarios: collinear vs orthogonal

In the study conducted by M. Finazzi et al., a comprehensive investigation delves into the intricate ground-state configuration of interfaces between magnetically compensated AFM and FM materials[48]. This exploration primarily focuses on the alignment of the AFM layer's magnetic easy axis with respect to the bulk FM moments, aiming to unravel the fundamental mechanisms at play. It's elucidated that in an ideal scenario, this magnetic interface adopts a ground state referred to as the spin-flop state, characterized by a unique perpendicular orientation of the FM moments with respect to the AFM magnetic axis. This spin-flop state[75], once it's observed, remains remarkably stable. However, the initial presumption that this state leads to exchange bias was subsequently contested by a more accurate model based on moment precession dynamics rather than energy minimization.

Interestingly, this study reveals that the presence of defects at the interface can disrupt the spin-flop ground state. Such disruptions lead to a shift from the ideal perpendicular alignment to a collinear coupling between the FM and AFM moments, as shown in Fig. 2.9. The extent of this deviation from the ideal state is contingent on various factors. For instance, the magnitude of the effective exchange field (H_{ex}) and the proportion (u) of magnetically active defects at the interface play pivotal roles in determining the nature of this deviation. Moreover, Monte Carlo simulations in this study provide additional insights. They suggest that the transition from collinear to perpendicular alignment of FM and AFM spins occurs at lower temperatures, particularly in cases involving rough interfaces[76]. Additionally, beyond interface defects, the study

highlights the substantial impact of volume defects, such as dislocations within the AFM material. These defects have the potential to disrupt the collinear alignment of spins within the AFM layer, affecting their coupling with FM magnetization. In essence, this research not only sheds light on the complex configurations at magnetically compensated AFM–FM interfaces but also underscores the significant influence of defects, whether at the interface or within the material volume, on the resultant magnetic behaviour.

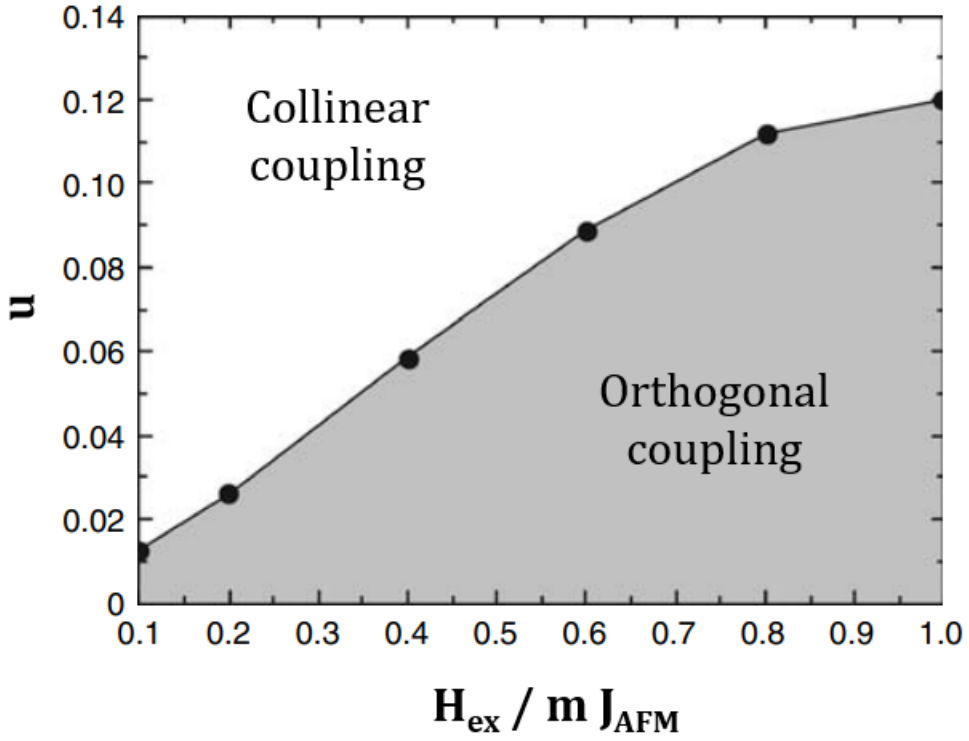

Fig. 2.9 Illustration of the regions in the parameter space where the ground state of the system is determined by either collinear or orthogonal AFM-FM coupling. The parameter H_{ex} represents the magnitude of the effective exchange field caused by magnetically active defects at the AFM-FM interface. The parameter u corresponds to the fraction of atomic sites at the interface, ranging from 0 (indicating an ideally compensated interface) to 1 (indicating a completely uncompensated interface). J_{AFM} represents the super exchange coupling constant, and m represents the local magnetic moments in the AFM material. Data is adapted from reference[77].

In addition to interface defects, there are multiple factors that influence the coupling between AFM and FM materials at the AFM-FM interface[48]. One such factor is

the presence of volume defects, including dislocations within the AFM material. These defects can disrupt the collinear alignment of spins within the AFM layer, thus affecting the coupling between FM magnetization and AFM anisotropy axis[78]. Furthermore, the AFM-FM interface coupling in real systems can be strongly dependent on the conditions under which the interface is prepared. This is due to the presence of frustration caused by competing exchange interactions. Additionally, magnetoelastic effects induced by strain should be taken into consideration. For example, thin FM metal films (such as Fe and Co) on NiO(001) exhibit perpendicular coupling between FM and AFM, while the coupling is collinear for thin NiO films on Fe(001)[79,80]. Moreover, in the case of the NiO/Fe(001) system, the coupling is dependent on the thickness of the NiO layer. When the NiO thickness is less than approximately 15 Å, the anisotropy axis aligns parallel to the magnetization of the Fe substrate. However, as the NiO coverage exceeds 25 Å, the anisotropy axis rapidly becomes perpendicular to the Fe magnetization[80].

2.4. Interlayer exchange coupling in AFM/S/FM

The use of a non-magnetic spacer in FM/Spacer/FM systems has been extensively studied, with numerous research works focusing on the characteristic oscillation of interlayer exchange coupling in such configuration[81–85]. However, comparatively little attention has been given to employing a non-magnetic spacer in AFM-FM systems. In this chapter, my aim is to present pioneering works that have explored the interlayer exchange coupling in AFM/spacer/FM systems using a non-magnetic spacer. Furthermore, in Chapter 6, I will present our own findings and results pertaining to this study, contributing to the understanding of the interplay between AFM and FM layers through a non-magnetic spacer[86].

Gökemeijer et al.[87] discuss the significant advancements made in understanding the coupling between AFM and FM thin layers through a non-magnetic spacer. To investigate the coupling, the authors intentionally inserted a nonmagnetic spacer layer between the FM and AFM layers and field cooled the sample below the T_N of the AFM layer. They experimentally demonstrate that exchange bias can occur across the spacer layer, indicating that the exchange coupling is a long-range interaction that extends over several tens of angstroms. This coupling is not oscillatory like the interlayer coupling

observed in FM-FM systems but instead decays exponentially. The range of the FM-AFM exchange coupling is specific to the spacer material, suggesting that it is likely of electronic origin. By varying the thickness of the spacer layer and studying different spacer materials (such as Cu, Au, and Ag), the authors observe that the coupling strength decreases exponentially with increasing spacer thickness. They propose a revised expression for the exchange field that considers interactions beyond the immediate interface and accounts for the long-range nature of the coupling.

A. Paul et al. studied the same effect of an insulating spacer layer on the exchange bias phenomenon in bilayers consisting of $CoO/AlO_x/Co$ structures and investigated the impact of varying the thickness of the bottom Co layer and the AlO_x spacer on the exchange bias field[88]. Similar to the previously mentioned work, they have observed that field cooling the system will result in exchange bias. In this study, the researchers investigate the influence of an insulating spacer layer, specifically AlO_x, on the exchange bias effect. Unlike previous studies using metallic spacers, the non-conductive nature of the AlO_x spacer suggests that interlayer exchange coupling is not expected to play a role. However, they observe a significant enhancement of H_{EB} in the presence of an ultra-thin AlO_x spacer and a non-monotonic dependence on its thickness. In more details, the results demonstrate that the H_{EB} is enhanced compared to the situation without a spacer. The enhancement is particularly notable for a thickness of approximately 1.0 nm for the AlO_x spacer. Moreover, the dependence of H_{EB} on the spacer thickness shows a non-monotonic behaviour.

Using different materials for the metallic spacer (Al, Ag, Au, Si, Pd, Ru, Ti), L. Thomas et al. observed that both the H_{EB} and coercive field (H_C) decrease exponentially with increasing spacer thickness[89]. The characteristic length scale for this exponential decay is a few Angstroms. Some materials, such as Al and Ti, exhibit a nonmonotonic variation in H_{EB} for very thin spacer layers. The results show that H_{EB} decreases rapidly with increasing spacer thickness and becomes negligible for spacer layers thicker than approximately 8 Å. Most materials exhibit a monotonic variation, except for Ti which shows oscillatory behaviour within a specific thickness range. Authors also showed that the decay length estimated from the exponential decay is approximately 0.5 Å for most spacer materials, except for Ag which has a longer decay length of 7.5 Å.

3. Chapter three: Research methodology

In this chapter, the techniques that were used to prepare and characterize the samples studied in this thesis will be presented. Two similar UHV systems were used for samples preparation. Namely, these were preparation chamber in the laboratory of "Nanostructures on surfaces" in AGH University of Krakow and preparation chamber of the multichambered UHV system at the PIRX beamline in Solaris facility. Both systems included molecular beam epitaxy technique to grow the samples (sec. 3.1.1) and Low-energy electron diffraction (sec. 3.1.2) to monitor the quality and type of crystallographic orientation at the surface and interfaces of studied systems. Fig. 3.1 shows the setup of the UHV preparation chamber at AGH. It is equipped with manipulator used to move the samples inside the UHV chambers, Residual Gas Analyser (RGA) for potential leak detection and determination of particular residual gases partial pressures, Low-energy electron diffraction (LEED) for characterizing the crystallographic structures of the grown films and to monitor the quality of their surfaces, UFO chamber to transfer the sample between the UHV chambers, and MBE for high quality and chemically clean materials deposition.

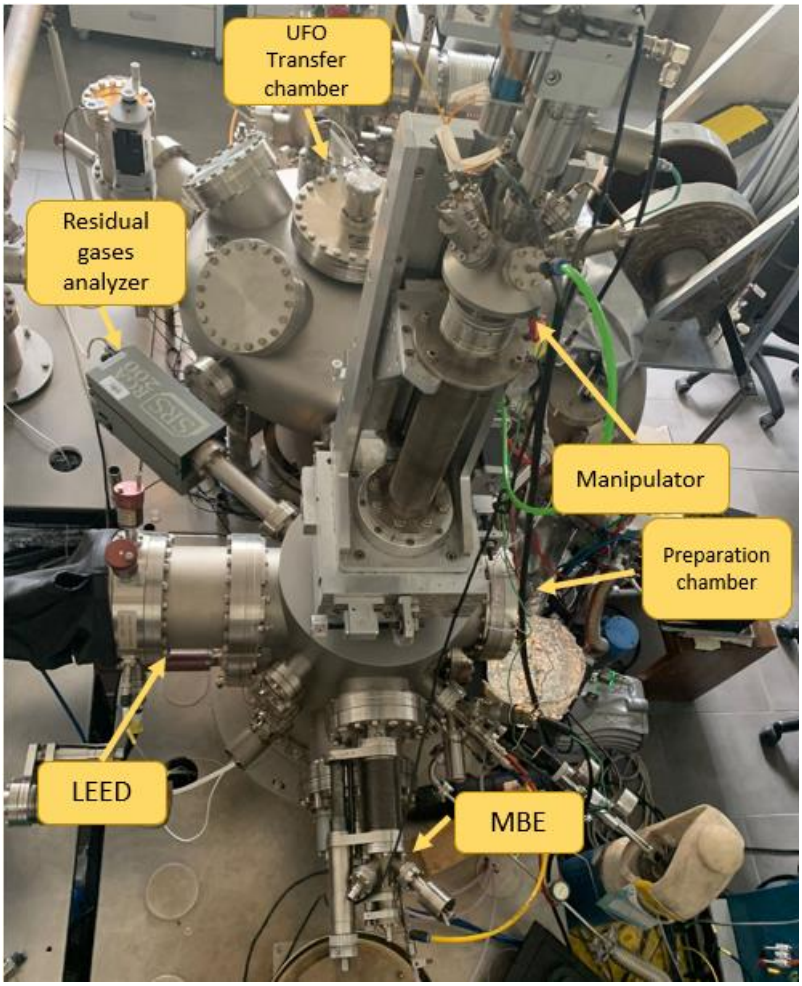

Fig. 3.1 Photo of the preparation chamber at the laboratory of nanostructures on surfaces in AGH University of Krakow.

3.1. Sample preparation and its in-situ structural characterization

3.1.1. Molecular beam epitaxy (MBE)

Molecular beam epitaxy (MBE) represents an advanced technique for depositing thin films under ultra-high vacuum (UHV) conditions, wherein focused beams of thermally activated atoms and molecules are directed onto a substrate. This process, which is called thermal evaporation, as a refined version of vacuum evaporation, requires a complex apparatus to achieve precise control.

The majority of UHV deposition techniques rely on the process of thermal evaporation or sublimation of materials. When a substance is heated to a sufficiently high temperature, certain atoms or molecules gain enough energy to overcome the chemical

bonds holding them together, causing them to escape from the material. This phenomenon is known as evaporation when it occurs from liquid form and sublimation when the material source has a solid form. To quantify the rate at which atoms or molecules are deposited onto a substrate positioned at a distance L from the deposition source, the flux, denoted as I, can be expressed as:

$$I = \frac{p(T)\,A}{\pi\,L^2\sqrt{2\pi m K_B T}} \tag{3.1}$$

In this context, $p(T)$ represents the equilibrium pressure, and A represents the evaporation area, while m refers to the molecule's mass. Boltzmann's constant is denoted as K_B, and T represents the temperature.

In order to achieve a deposition rate ranging from 0.1 to 1 monolayer per minute, with a distance of 10 cm (L) and an area of 0.5 square centimetres (A), an equilibrium vapor pressure of approximately 10^{-5} to 10^{-4} Torr is necessary, and the temperature of the source to get this vapor pressure for selected elements(Fe, Co, Ni, and Au) should be in the range of 1150 – 1250 K[90].

The simplest thermal sources are characterized by their straightforward design and are often crafted in-house. They consist of open heaters without any radiative or insulating shielding or mechanisms to mitigate thermal gradients. Typically, they are constructed using refractory metal foils, such as boats and tubes, or shaped filaments and baskets. Direct heating is achieved by passing an electrical current through these elements. One limitation of these sources is their inability to produce a consistently stable deposition rate.

In more advanced applications the so-called Knudsen cells, also known as K cells (or effusion cells), are utilized when highly consistent evaporation rates are required. A photo of exemplary K cell equipment attached to the UHV system at AGH laboratory is shown in Fig. 3.2 (a). These cells operate on the principle of molecular effusion, which was first demonstrated by Knudsen as early as 1909[91]. A Knudsen cell, schematically shown in Fig.3.2 (b), consists of a crucible made from tungsten in traditional K cells or materials such as alumina or pyrolytic boron.

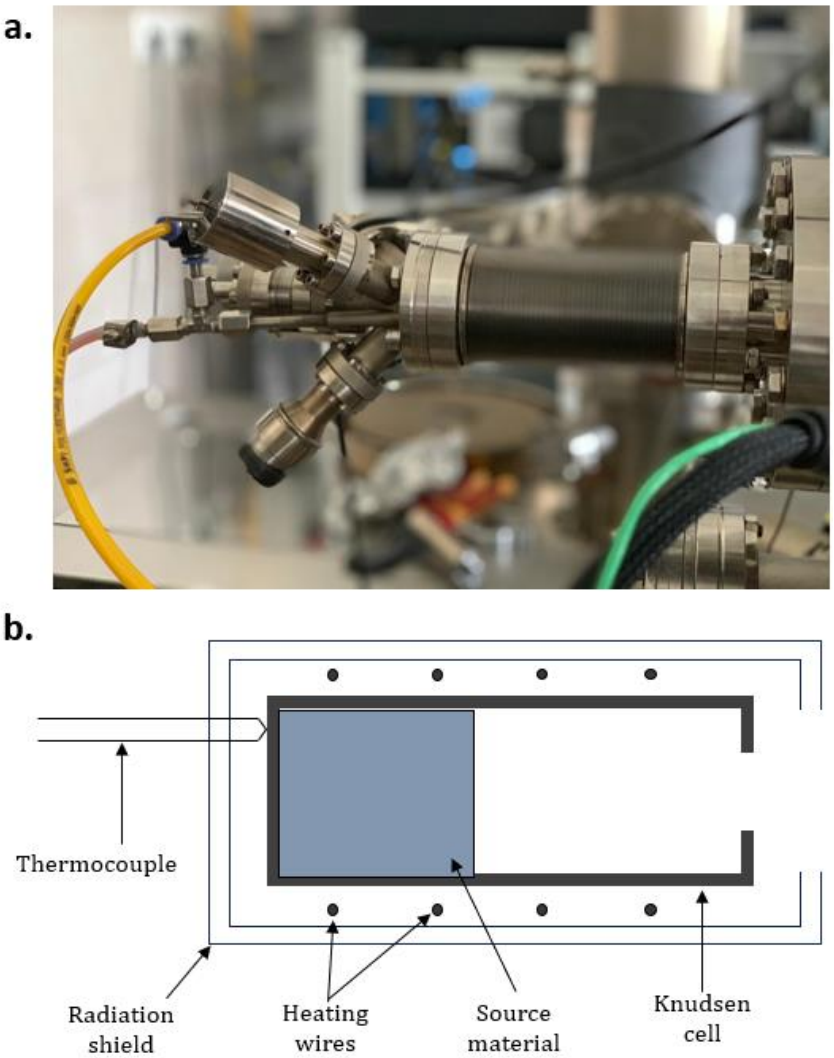

Fig. 3.2 (a) a picture of a Knudsen cell (b) a schematic diagram of a Knudsen cell.

MBE, as its name implies, utilizes focused beams of atoms or molecules within a high-vacuum environment to supply the necessary building blocks to grow a crystal on a substrate surface. These beams are directed towards the crystal, which can be maintained

at a moderately elevated temperature. This temperature provides sufficient energy for the arriving atoms to move across the surface and find their appropriate positions within the crystal lattice. The UHV conditions ensure minimal contamination on the growing surface. Within the vacuum environment, the atoms and molecules in the beams travel along almost collision-free paths until they reach either the substrate or the walls of the chamber. Upon contact, they condense and are effectively eliminated from the system. By inserting a shutter in the beam, the flow of atoms can be instantly halted. This capability allows for slow and contamination-free film growth.

The general design of MBE consists of a steel chamber that is fitted with pumps to establish an UHV environment, typically around 10^{-11} Torr. Within such system, there is a growth chamber housing multiple K-cell. These cells facilitate the evaporation of various atomic or molecular materials. The substrate, intended for growth, is positioned inside the chamber. It is carefully maintained at a controlled temperature while being subjected to high vacuum conditions. In some solutions (although not in the UHV system of the author home group at AGH), to ensure uniformity across the sample, it is also rotated during the growth process. Moreover, a principal shutter is placed between the K-cells and the substrate that shadows the surface of the substrate to give the possibility of growing samples with variable thickness of the deposited layer by moving the sample during the deposition process (see Fig. 3.3).

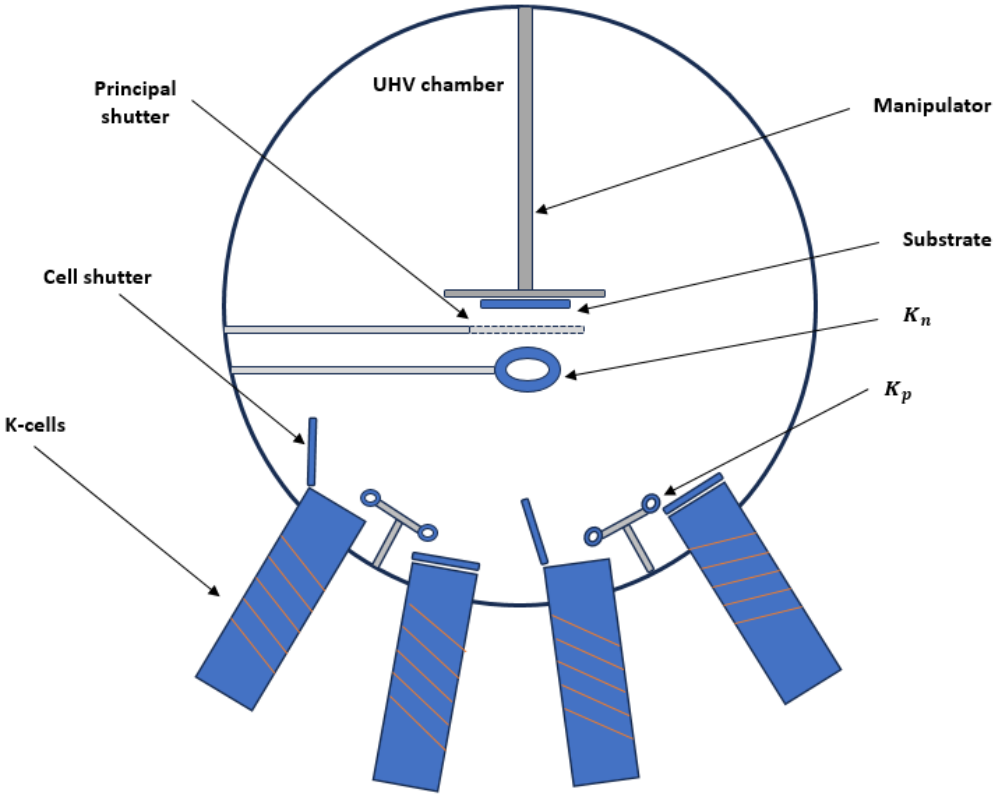

Fig. 3.3 Schematic configuration of MBE with multiple K-cells.

The last component of the setup is a quartz crystal monitor used to determine the deposition rate of the material. The system includes two monitors, one located near the effusion cells and the other closer to the sample. They are utilized to calculate the time needed to deposit a layer of a specific thickness. The frequency change of the crystal oscillations is proportional to the mass of the deposited material. Therefore, it is possible to calculate the needed change of frequency ΔF to grow a specific thickness (d) of a given element:

$$\Delta F = M_e \cdot \left(\frac{K_n}{K_p}\right) \cdot \left(\frac{K_p}{K_s}\right) \cdot d \tag{3.2}$$

where M_e $\left(\frac{\text{Hz}}{\text{Å}}\right)$ refers to the deposition constant of the element, K_n is the position of the quartz crystal monitor closer to the substrate, K_p is the position of the quartz crystal monitor closer to the effusion cells, and K_s is the position of the substrate. The ratios of the positions of the quartz crystal monitors and the substrate are added to compensate

for the error caused by the decreasing deposition rate with distance from the effusion cells. Determination of the frequency change speed that is read by the control software $\left({}^{df}/_{dt}\right)$ [Hz/min], allows to calculate the time of growing a specific thickness of an element:

$$t = \frac{\Delta F}{{}^{df}/_{dt}} \tag{3.3}$$

Precise control of evaporation speed and sample's thickness make MBE technique an excellent approach for material preparation in systems where relatively thin or ultrathin layers have to be fabricated[92].

3.1.2. Low-energy electron diffraction (LEED)

Electron and X-ray diffraction techniques are extensively employed for surface structure characterization. These methods analyse the particles or waves that are elastically scattered by the crystal to obtain valuable structural information. The intensity of the diffracted beams provides insights into the atomic arrangement within the crystal's unit cell. Additionally, the spatial distribution of these diffracted beams reveals details about the crystal lattice[93].

LEED is a powerful technique for surface analysis due to the de Broglie wavelength of electrons, which is calculated as:

$$\lambda = \frac{h}{\sqrt{2mE}} \tag{3.4}$$

In 3.4 formula, λ is the wavelength, h is Planck's constant, m represents the mass of the electron, and E is the electron energy. "Low-energy" electrons meet the condition of atomic diffraction, as their wavelengths are typically around 1 – 3 Å in the typical energy range employed in LEED (30-200 eV), which means that these wavelengths are of the

order of or smaller than interatomic distances. This fulfils the atomic diffraction condition, enabling the study of surface atomic structures. Moreover, low-energy electrons have a very short mean free path, typically spanning just a few atomic layers. Consequently, most elastic collisions occur in the topmost layers of a material, making LEED a valuable tool for investigating the 2D atomic structure of a sample's surface[94].

The schematic representation of the standard experimental arrangement for LEED is illustrated in Fig. 3.4. (a) In the standard LEED setup, an electron gun generates a collimated beam of low-energy electrons. These electrons interact with a sample placed on a sample holder, and the resulting diffraction pattern is observed using a hemispherical fluorescent screen equipped with grids to capture elastically scattered electrons. The electron gun unit comprises a cathode filament, a Wehnelt cylinder, and an electrostatic lens. The emitted electrons are accelerated to a specific energy within the gun and then scatter from the sample. A series of grids helps reject inelastically scattered electrons. The retarding voltage is adjusted to optimize the spot-to-background contrast in the LEED pattern. The resulting diffracted electrons pass through the fourth grid, are reaccelerated to a higher energy, and cause fluorescence of the screen where the diffraction pattern is visible.

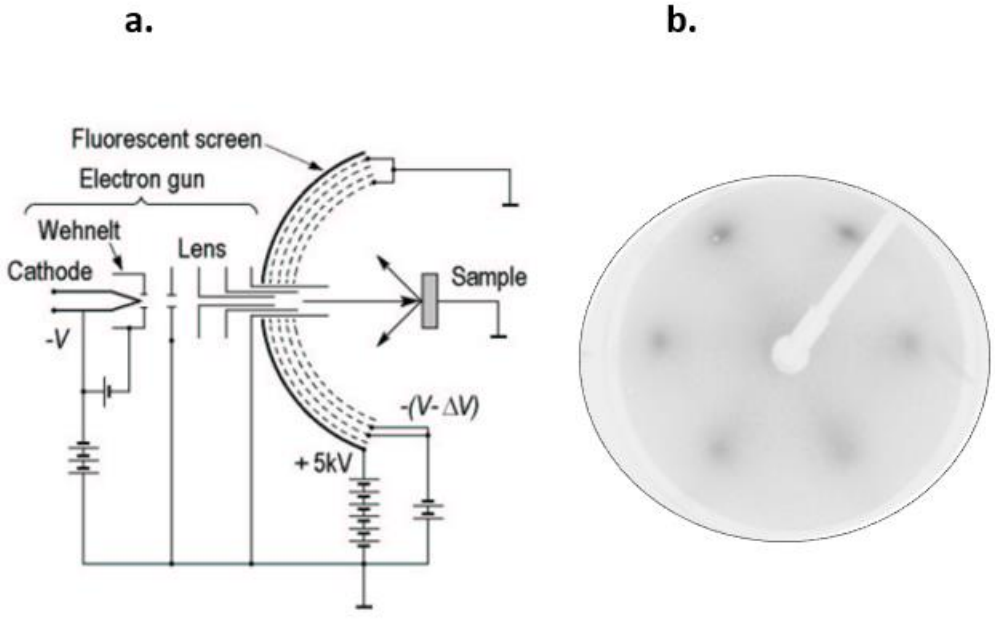

Fig. 3.4 (a)diagram of typical configuration of a four-grid LEED setup, adapted from reference [93]. Exemplary LEED pattern of CoO (111) surface shown in (b) was acquired in home laboratory of the author group.

3.2. Magnetic characterization techniques

3.2.1. Magneto-optic Kerr effect (MOKE)

The magneto-optical effect, first demonstrated by Michael Faraday in 1846[95], involves the rotation of the polarization plane of linearly polarized light passing through a glass rod subjected to a magnetic field. This rotation, known as Faraday rotation, is proportional to external magnetic field **H**. John Kerr's observation in 1877[96] extended the understanding of this effect to metallic iron mirrors, where the modification of light polarization, known as MOKE, was found to be proportional to **M** of the sample[97].

Today, MOKE is widely used to investigate the magnetization state in FM and ferrimagnetic samples due to its numerous advantages. It offers remarkable sensitivity, comparable to the best magnetometry techniques, making it particularly useful for studying the magnetism of ultrathin films[98]. In fact, MOKE can detect magnetization at the scale of a fraction of an AL within the FM material. MOKE provides rapid measurements, thanks to the short duration of the interaction between light and matter. By employing femtosecond pulsed lasers, time-resolved measurements with resolutions as low as 100 fs have been achieved[99]. Moreover, MOKE offers good lateral resolution, enabling the observation of magnetic domains[100] and facilitating the study of spatial magnetization distribution in various structures, including FM wires, patterned magnetic arrays, and self-organized magnetic structures[101]. In addition to its technical capabilities, MOKE measurements are relatively easy to perform and cost-effective. They can be conducted on samples located at a distance from the light source and detector, making MOKE a popular choice for studying thin film magnetism in vacuum chambers or under extreme conditions such as magnetic fields or varying temperatures.

MOKE relays on rotating the plane of polarized light reflected from the sample surface, a phenomenon called Kerr rotation. The switching of the magnetic orientation of the sample surface can cause this rotation leading to change of the intensity of the reflected light. The change of the polarized light intensity, which is captured by the detector, is proportional to the magnetization of the surface, and sensitive to the direction of the applied magnetic field on the sample. Hence, there are three geometries at which

MOKE can be set up, namely: Polar MOKE (PMOKE), Longitudinal MOKE (LMOKE), and Transverse MOKE (TMOKE).

In PMOKE, **M** is aligned out-of-plane with respect to the sample, while in LMOKE, **M** is aligned in-plane, and parallel to the plane of incidence of the polarized light, and lastly, TMOKE where **M** is also aligned in-plane but perpendicular to the plane of incidence of the polarized light, as demonstrated in Fig 3.5.

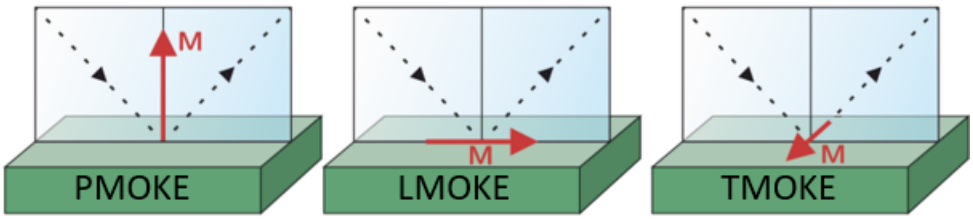

Fig. 3.5 MOKE configuration in three geometries: PMOKE, LMOKE, and TMOKE

A typical MOKE setup consists of set of electromagnetic coils, manipulator to hold the sample between the coils, a source of light (e.g., laser), a polarizer and an analyser, signal modulator, a Teslameter, and a detector (see Fig 3.6).

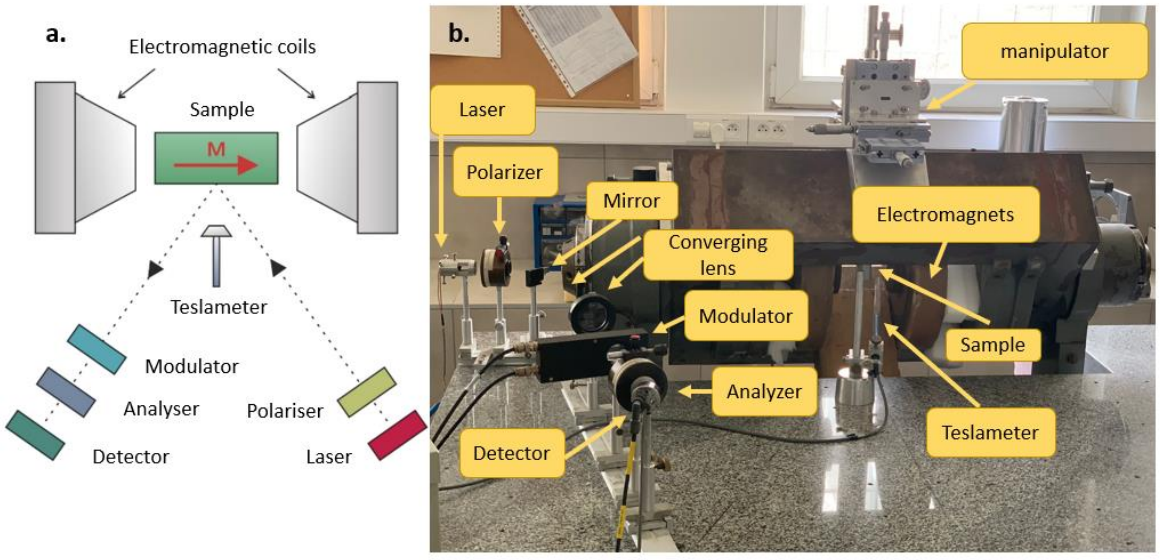

Fig 3.6 (a) schematic LMOKE setup. (b) Photo of PMOKE setup acquired in home laboratory of the author group

3.2.2. X-ray magnetic circular dichroism (XMCD)

The possibility of directly observing the Magnetic Circular Anisotropy (MCA) as a manifestation of orbital moment anisotropy was initially proposed by Bruno[24,102]. This opportunity emerged with the advent of a powerful magnetics technique known as XMCD spectroscopy. The technique was first introduced and refined by Schutz in 1987[103], and since then, it has undergone significant experimental[104,105] and theoretical[106,107] advancements, transforming into a precise tool for quantitative magnetometry. XMCD spectroscopy possesses several advantages over traditional magnetics techniques[24]. One of its primary strengths lies in its ability to accurately determine and separate the spin and orbital magnetic moments, along with their anisotropies, with element-specificity. Additionally, XMCD spectroscopy exhibits chemical sensitivity[108], enables the identification of magnetic moment orientations in ultrathin films and monolayer magnetic materials[109], leading also to element-specific magnetic imaging[110]. Furthermore, it allows for the determination of element-specific AC susceptibilities[111] and magnetization loops[112]. Lastly, XMCD spectroscopy demonstrates remarkable sensitivity at the sub-monolayer scale[104,113].

The origin of the XMCD effect in a magnetized sample can be most easily explained within a so-called one-electron picture[114], please see Fig. 3.7. In a 3d transition metals, the 2p core states are split in a j = 3/2 (L_3 edge) and a j = 1/2 (L_2 edge) levels. Corresponding spin and orbit angular momenta are coupled parallel and antiparallel to each other, respectively. XMCD can be described as a two-step process. Initially, the incoming beam helicity is parallel (antiparallel) to the 2p orbital moment. This arrangement results in the preferred excitation of electrons in the spin up (down) direction. The second step consists of the electron occupying a state in the 3d band. If there are less spin up than spin down holes available, the XMCD spectrum then has a negative net L_3 peak and a positive L_2 peak. Taking right (μ^+) and left (μ^-) polarizations, and **M** as the sample magnetization, the XMCD signal can be defined as the difference spectrum between them.

$$\Delta\mu = \mu^+(-M) - \mu^-(-M) = \mu^-(M) - \mu^+(M) \tag{3.5}$$

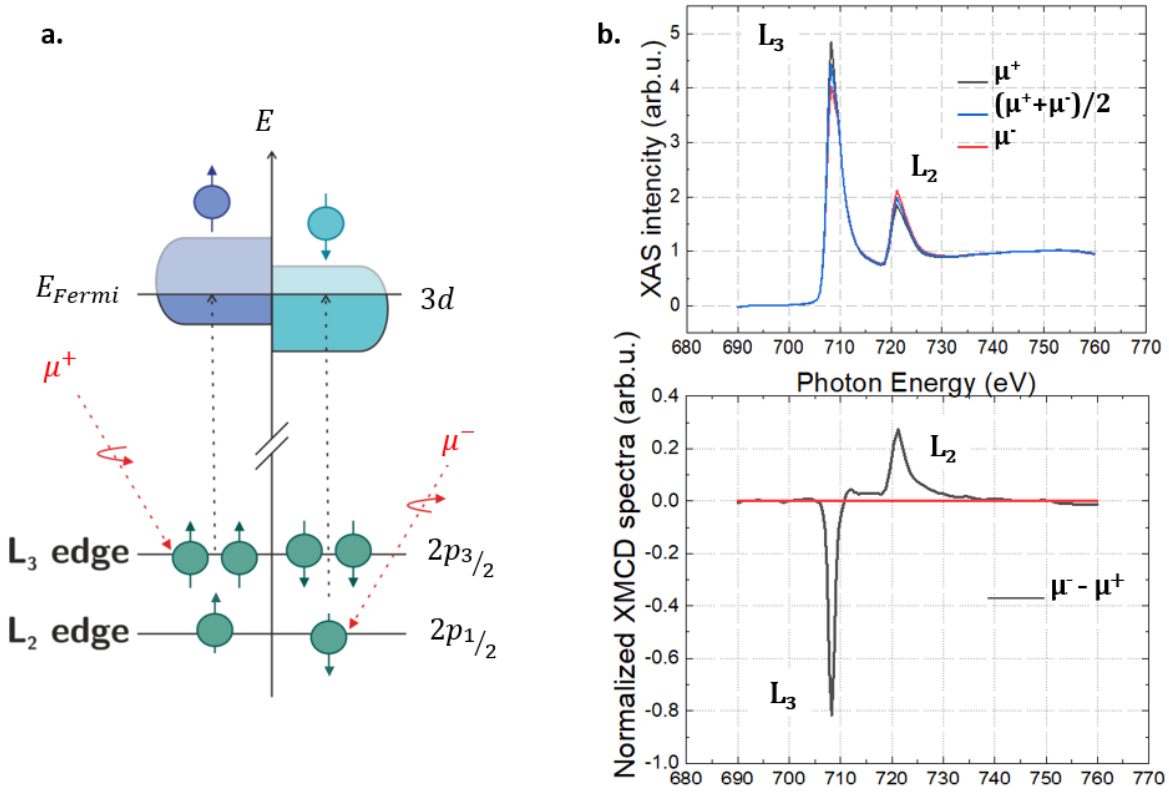

Fig. 3.7 (a) two-step picture for XMCD of a single-electron system in a magnetic material. Electrons from the $2p_{3/2}$ level are preferentially excited into spin up states in the 3d band, while those from the $2p_{1/2}$ level are preferentially excited into spin down states. (b) X-ray Absorption Spectroscopy and XMCD spectra for the Fe $L_{2,3}$ edge, showing the right (μ^+) and left (μ^-) handed polarization, along with their sum (absorption spectrum) and the difference spectrum (XMCD).

3.2.3. X-ray magnetic linear dichroism (XMLD)

X-ray Magnetic Linear Dichroism (XMLD) is a valuable method for investigating the magnetic properties of materials. This technique extends the capabilities of X-ray Absorption Spectroscopy (XAS) and relies on the difference in absorption spectra between linearly polarized radiation with electric field vector **E** aligned perpendicular

and parallel to the magnetic moments of the sample. Unlike X-ray Magnetic Circular Dichroism, XMLD's signal strength depends not only on the square of the magnetic moment but also on the angle between the **E** vector and the magnetic axis of the studied system. This makes it particularly useful for examining AFM materials. The XMLD effect arises from the distortion of atomic charge induced by the spin-orbit interaction, occurring when atomic spins align axially due to the exchange interaction.

To demonstrate the impact of spin-orbit coupling on the charge distribution, Fig. 3.8 (a) displays the charge densities of individual components within the spin-orbit split $p_{1/2}$ and $p_{3/2}$ states. Notably, each individual density, represented by the squares of wavefunctions, exhibits spatial (not spherical) anisotropy with respect to the z-axis alignment of the spin. Conversely, when summing over all m_j substates within each j manifold, the resulting charge distributions become spherically symmetric, see Fig. 3.8 (b). This observation leads to the conclusion that a linear magnetic dichroism effect will only be present if the m_j substates in the initial or final states of the electronic transition are split and contribute unequally to the X-ray absorption intensity. In magnetic materials, such a splitting between m_j substates in the valence and core shells naturally arises in the presence of the exchange interaction below the magnetic transition temperature.

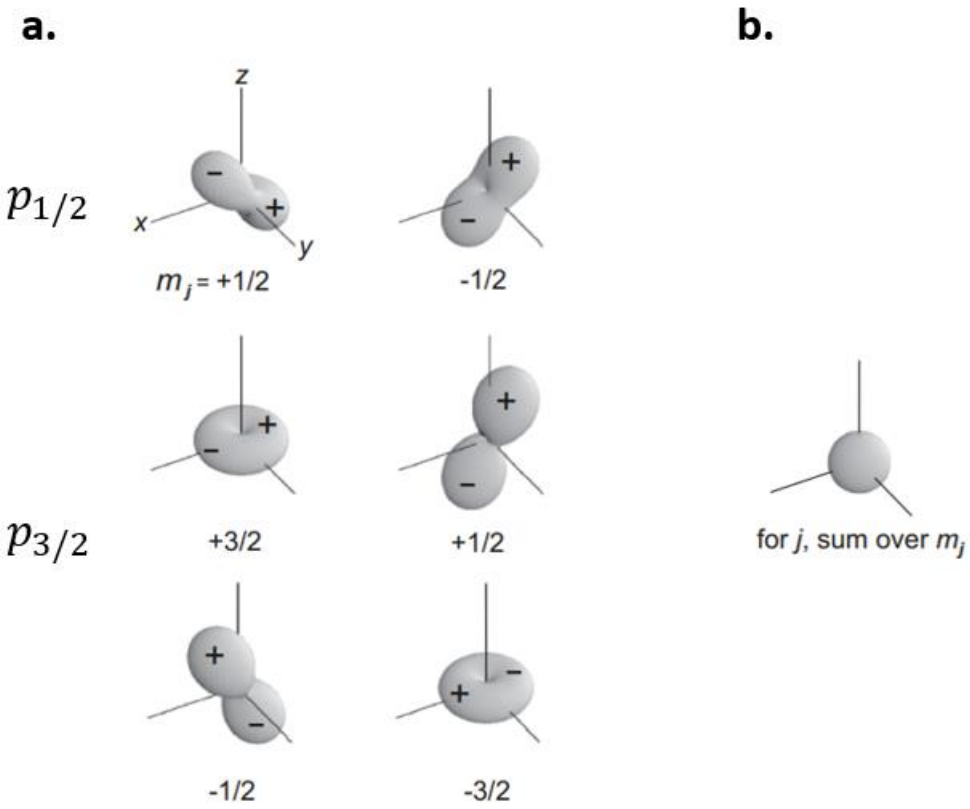

Fig. 3.8 The orbital densities corresponding to the p_j states ($p_{1/2}$ and $p_{3/2}$) are depicted. The particular substates are denoted by quantum numbers m_j for clarity. The z-axis is chosen as the reference axis for spin quantization. Notably, the charge distributions exhibit spatial asymmetry, leading to varying X-ray absorption intensities when the E-vector aligns either parallel or perpendicular to the z-axis. The (b) figure displays the spherically symmetric charge density resulting from the summation of all m_j states, as well as the summation of m_j states within a given *j*. Figure adapted from reference [20].

Experimentally, the difference in intensity for XMLD is often obtained by conducting two measurements (see equation 3.6): one with the **E** aligned parallel to the magnetic moments of the sample and another with the **E** perpendicular to it.

$$\Delta I_{XMLD} = I^{\parallel} - I^{\perp} \tag{3.6}$$

where $I^{\parallel}$ and $I^{\perp}$ are the absorbed intensities when **E** is aligned parallelly and perpendicularly with the magnetic axis, respectively.

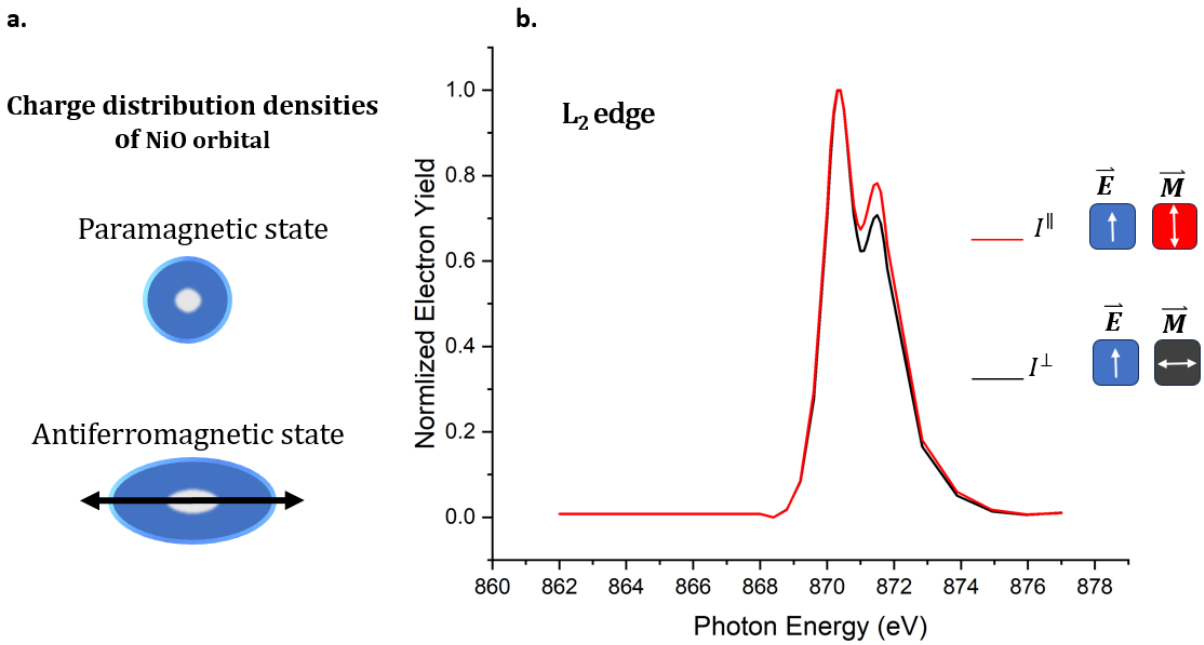

Fig. 3.9 (a) A schematic representation of the charge distribution densities of NiO above and below T_N. (b) An XMLD spectra of NiO for **E** aligned parallel and perpendicular to the magnetic moments **M**.

The origin of the XMLD effect in AFM oxides can be demonstrated using the example of NiO. Above T_N, NiO orbital has a symmetrical, sphere-like charge distribution densities as a typical paramagnet. But for lower temperatures, i.e., at RT, NiO is an AFM, and the Ni spins start to orient in two opposite directions leaving zero net magnetization and a preferred magnetic axis (see Fig. 3.9 (a)). This alignment of the Ni spins along the preferred magnetic axis leads to breaking the symmetry of the charge distribution in the Ni spin orbit and having ellipse-like charge distribution densities. This leads to creating a small a-symmetry in the x-ray absorption signal which is proportional to the charge anisotropy of the density distribution. According to equation 3.6, XMLD effect is calculated by the difference between $I^{\parallel}$ and $I^{\perp}$. Fig 3.9 (b) shows this difference in the second peak near L_2 absorption edge of Ni. This noticeable difference in the second peak of $I^{\parallel}$ and $I^{\perp}$ is considered as the fingerprint of the NiO magnetization.

4. Chapter four: NiO(111)/Fe(110)

4.1. Introduction

As mentioned in chapter two, controlling the magnetic spins in AFM can lead to advantageous usage in spintronics. Magnetic control of AFM spin structure can be done by applying a strong external magnetic field which drives the transition to spin-flop state [115,116], or by the employing the interfacial exchange coupling to a neighbouring FM [50,67,117]. This chapter focuses on the magnetic control method by tuning the MA of Fe(110) layer in NiO(111)/Fe(110) system. The exchange bias that is caused by the AFM layer, and the well-known SRT which is documented in FM layers [40,118–120], cause an exchange interaction in such systems which can be employed to get a better control over the magnetic spin structure on the AFM layer.

4.2. Sample preparation

Fe(110) was grown using MBE on atomically clean W(110) single-crystal surface at RT, subsequently followed by annealing at 675 K for about 15 minutes to smoothen the Fe surface. By having the principal shutter shadowing the sample during Fe growth, two sample regions, with the thicknesses of Fe 50 Å and 150 Å, were created. Analogous but more complicated sample consisting of several Fe stripes with the thickness in the range of (70-110 Å) was also prepared for dedicated experiment to document the temperature-driven SRT on Fe and NiO, as will be precisely described at the end of this chapter. Both samples were covered by homogeneous NiO(111) overlayers with the thickness d_{NiO} = 40 Å which was grown at RT by reactive deposition of Ni in partial oxygen pressure $1x10^{-6}$ Torr. Fig. 4.1 (a and b) show the LEED snapshots of the diffraction pattern of the surface of the system for both Fe and NiO taken during the preparation of the sample, followed by their corresponding ball model below (c and d).

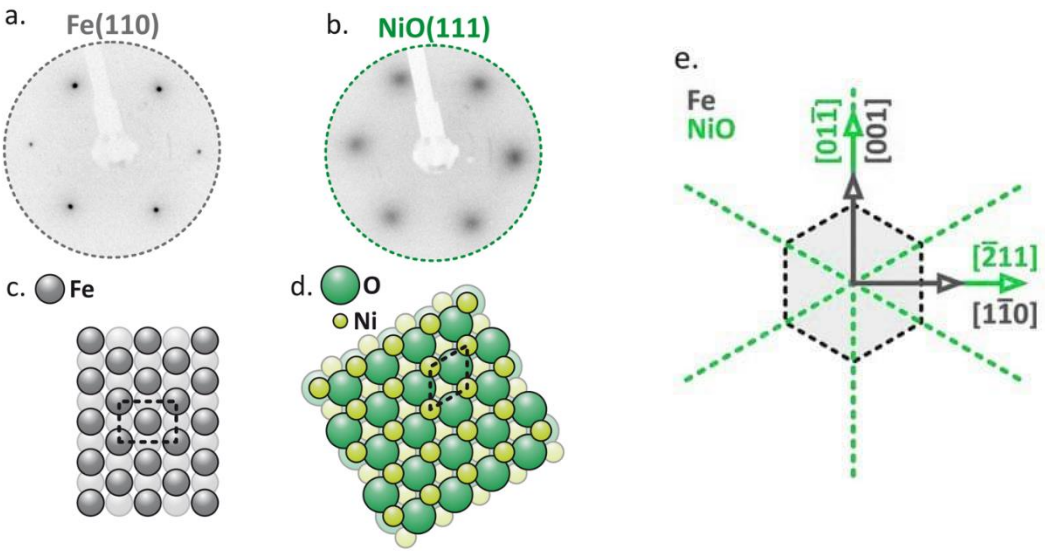

Fig. 4.1 (a) & (b) LEED snapshots for uncovered Fe(110) and NiO(111)/Fe(110), respectively. (c) & (d) corresponding ball models. Fe(110) and NiO(111) in-plane directions are shown in (e)

In Fig.4.2 the exemplary LEED patterns of the uncovered Fe(110) (top panel) and NiO(111)/Fe(110) surface (bottom panel) are shown for both studied Fe thicknesses, 50 Å (left) and 150 Å (right). Dashed lines mark image sections used for determination of diffraction spots intensity profiles, as presented in Fig. 4.3.

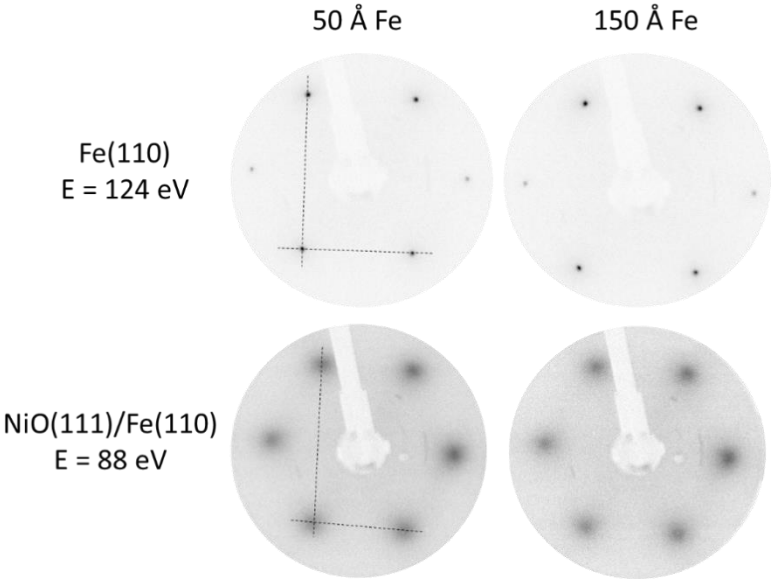

Fig.4.2. LEED patterns together with image sections (dashed lines) used for determination of diffraction spots intensity profiles, as further presented in Fig. 4.3.

In Fig. 4.3 intensity profiles as determined from corresponding diffraction patterns (Fig. 4.2) are shown. From both analyzed in-plane directions one can conclude that Fe(50 Å) and Fe(150 Å) (110) oriented surfaces are perfectly isostructural (please see top panel of Fig. 4.3). The same concerns sample after covering by NiO: NiO(111)/Fe(50 Å) and NiO(111)/Fe(150 Å) surfaces can be treated as almost isostructural (bottom panel of Fig. 4.3). This is an important conclusion because it means that all differences in magnetic properties of NiO/Fe bilayers described in the following part of this chapter have magnetic, not structural origin.

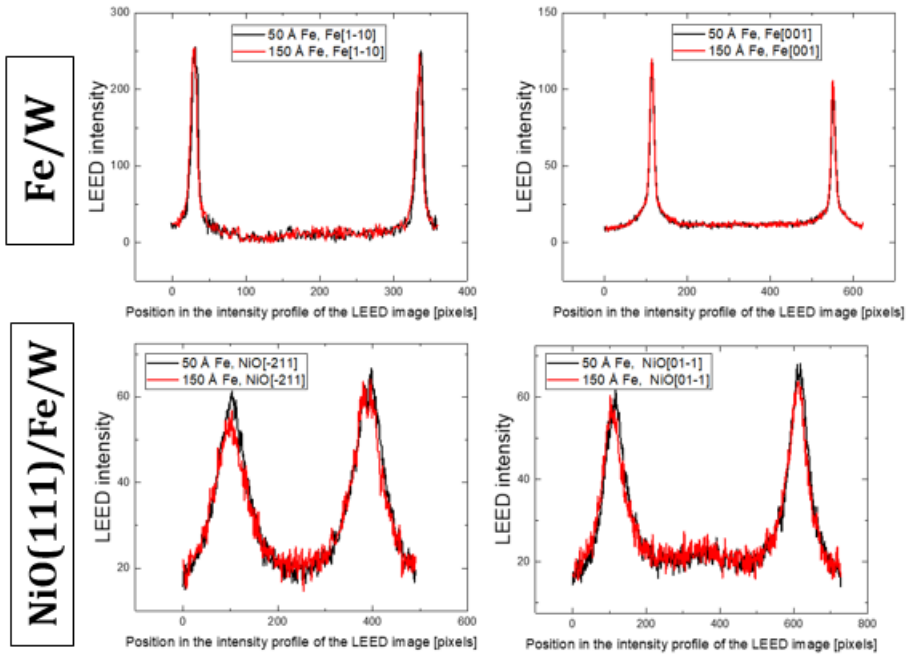

Fig.4.3 Intensity profiles as determined from corresponding diffraction patterns presented in Fig.4.2.

4.3. Results

XMCD spectra in Fig 4.4 (a), captured for both regions of Fe(110), show a noticeable asymmetry between the left- and right-hand polarization (LHP & RHP) on the region where **M** is aligned along $[1\bar{1}0]$ direction (parallel to **k**– thin Fe), while no XMCD effect is noticed on the thicker Fe where **M** is aligned perpendicular to **k**. Similarly, a small but noticeable distinction between the XMLD spectra can be seen, acquired with linear polarization parallel to NiO$[01\bar{1}]$||Fe[001] direction, on the 50 Å and 150 Å Fe regions, which is seen by comparing the second peak of the XAS spectra acquired before and after SRT. It is worth noting that the XMLD magnitude of NiO is typically defined by the so called R_{L2}, which in this thesis is defined as the ratio of the intensities of higher energy peak (P_2) to lower energy peak (P_1) at the vicinity of Ni L_2 absorption edge [121] (see Fig 4.4 (b)).

Fig. 4.4 (c) shows x-ray photoemission electron microscopy (PEEM) images, where XMCD-PEEM image of the Fe (50/150 Å) border is captured at RT (top image). The magnetic boundaries between the two thicknesses of Fe(111) are clearly seen. In this setup, the photon beam direction **k** is aligned along the magnetic spin direction of the thin Fe layer, specifically along Fe$[1\bar{1}0]$ (Fig. 4.4 (c) bottom of the top image), and perpendicular to the magnetization direction of the bulk-like thick Fe layer which is magnetized along [001] direction. The characteristic zig-zag pattern seen here indicates a 90° rotation of the magnetic spin orientation between these two Fe thicknesses [122].

On the same region, an XMLD-PEEM image was taken showing the domain structure for the homogeneous NiO(111) overlayer. This XMLD-PEEM image was acquired at the Ni L_2 edge with linear polarization **E** within the NiO(111)||Fe(110) sample surface plane and with **k** vector along NiO$[0\bar{1}1]$||Fe[001] direction. Fig. 4.4 (c) (middle image) shows a similar pattern with the distinguished zig-zag on NiO(111) surface, to the one that is captured on the Fe(110) with circular polarization. This zig-zag pattern represents clear evidence on the 90° rotation of NiO layer magnetic moments between two analysed NiO(111)/Fe(110) sample regions. There is no doubt that the vicinity to the Fe layer has led to having an SRT on the AFM NiO layer from NiO$[\bar{2}11]$∥Fe$[1\bar{1}0]$ to the NiO $[0\bar{1}1]$∥Fe[001], similar to the one on Fe (see Fig. 4.1 (e)). This means, the magnetic

structure of the AFM NiO layer is directly affected by the spin reorientation transition between the two orthogonal FM Fe regions.

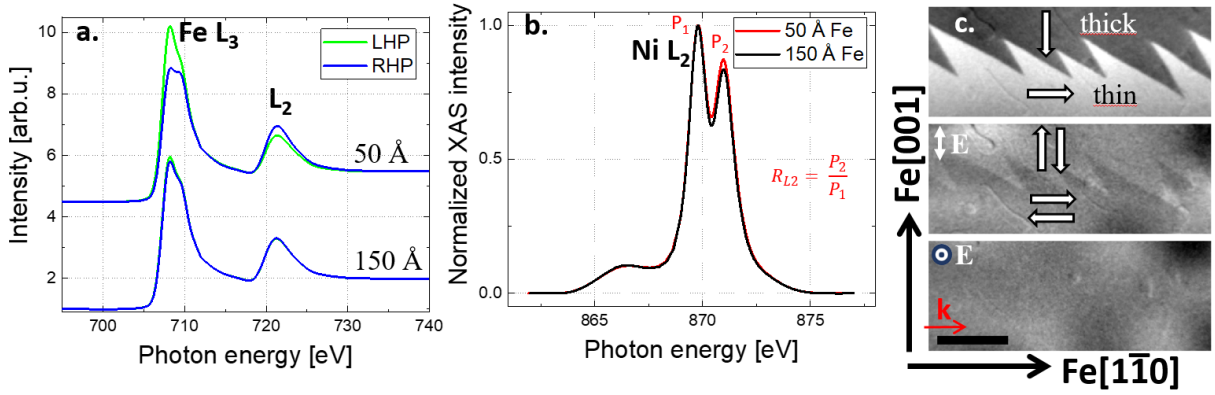

Fig. 4.4 (a) XAS spectra captured for 150 Å Fe and 50 Å Fe covering L_3 and L_2 edges absorption edges of Fe. (b) XMLD spectra captured for both NiO overlayers covering 150 Å and 50 Å Fe. (c) XMCD-PEEM and XMLD-PEEM images captured for Fe(110) and NiO(111) respectively, **k** is the direction of the x-ray beam, **E** is the is the electric field vector.

Fig. 4.4 (c) bottom image displays an XMLD-PEEM image acquired with linear polarization, closely aligned with the surface normal. In this instance, the absence of magnetic contrast substantiates the conclusion that NiO spins are confined within the NiO(111) sample plane, as anticipated. It is important to note that XMCD-PEEM images obtained at the Ni L_3 edge (not shown) do not reveal any magnetic contrast across the 50/150-Å Fe border, affirming that the contrast visible in the XMLD-PEEM image in Fig. 4.4 (c) originates solely from the AFM ordering in NiO. Consequently, Fig. 4.4 provides compelling evidence that in-plane SRTs are observed across the 50/150-Å Fe border in both the ferromagnetic Fe and antiferromagnetic NiO sublayers of the NiO(111)/Fe(110) bilayer.

To scrutinize the magnetic properties of antiferromagnetic NiO(111) overlayers, rigorous angle-resolved and temperature-dependent XMLD measurements were conducted, as depicted in Fig. 4.5 (a) alongside the experimental geometry sketch. Initially, the dependence of the R_{L2} ratio on the polar angle θ at various temperatures was examined (Fig. 4.5(b)), maintaining a fixed azimuthal angle $\varphi = 0°$ In this geometry, the

electric field vector **E** projection on the NiO(111)||Fe(110) sample plane aligns with the NiO[$\bar{2}$11] || Fe[1$\bar{1}$0] in-plane direction. Consequently, for the 50-Å-thick Fe region, increasing the polar θ angle corresponds to an augmentation in the angle between **E** and NiO spins. Conversely, in the 150-Å-thick Fe region, the angle between **E** and NiO spins remains constant as the θ angle varies. While one might intuitively expect a strong dependence of $R_{L2}(\theta)$ on the 50-Å-thick Fe region and no dependence on the 150-Å-thick Fe region, Fig. 4.5 (b) reveals that R_{L2} depends strongly on θ for the 150-Å region (black circles), whereas for the 50-Å-thick Fe region (green circles), the corresponding dependence is much weaker. This seemingly surprising observation aligns with findings in reference[123] suggesting that the XMLD asymmetry in NiO relies not only on the relative orientation of the electric field **E** and AFM spins but also on their orientation with respect to the crystallographic axes[124,125].

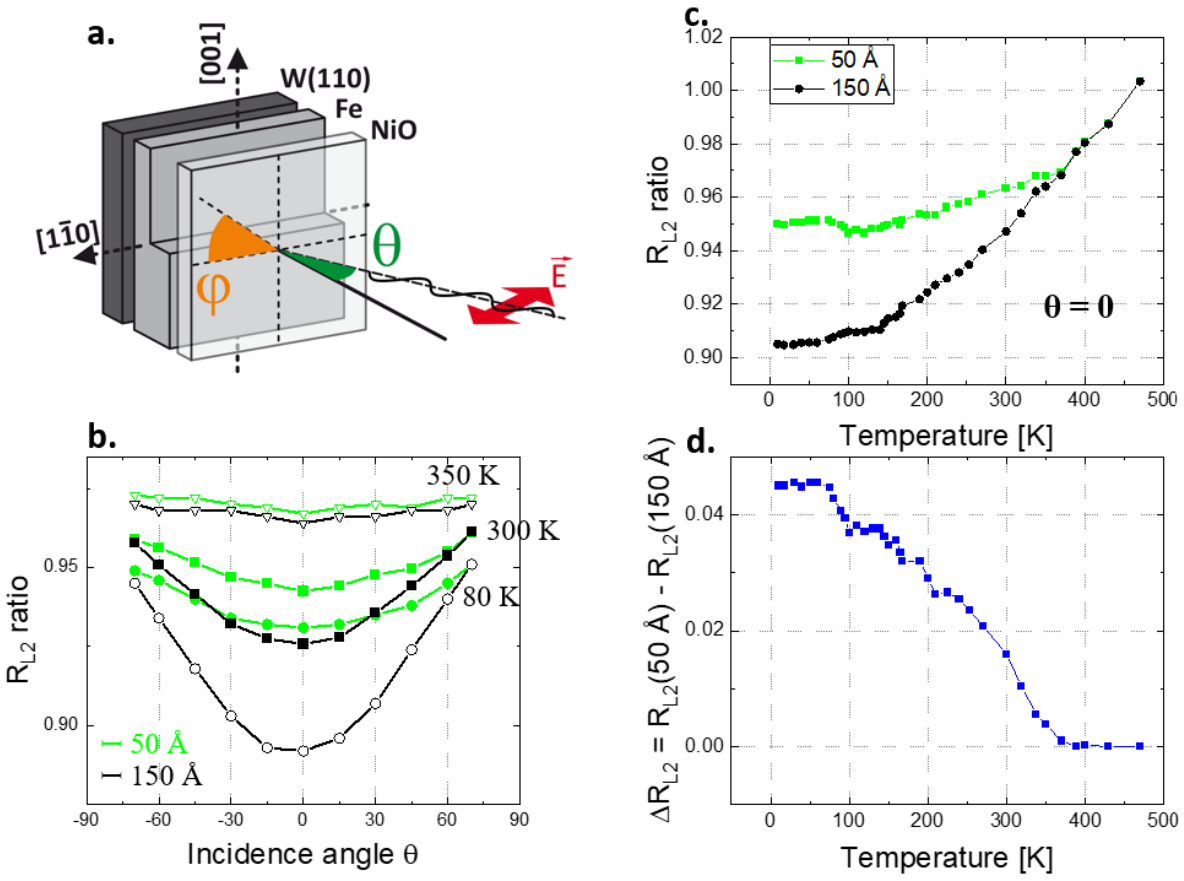

Fig 4.5 (a) Schematic sketch of the geometry of angle-resolved XMLD measurements. (b) Dependency of the R_{L2} ratio on the polar angle θ (with a fixed

$\varphi = 0°$) at temperatures of 80 K (circles), 300 K (squares), and 350 K (triangles), considering two different thicknesses of studied Fe layers, namely 50 Å (in green) and 150 Å (in black). (c) Variation of the R_{L2} ratio with temperature for regions of the sample corresponding to NiO/50 Å Fe and NiO/150 Å Fe. (d) Temperature-related changes in the R_{L2} ratios, as defined in (c), represented by $\Delta R_{L2(\theta=0)}$ calculated as $R_{L2(50\ Å)} - R_{L2\ (150\ Å)}$.

Angular dependencies of R_{L2} ratios at low temperatures, depicted in Fig. 4.5, confirm the confinement of NiO spins in-plane and their collinear coupling to neighbouring Fe magnetic moments. As temperature increases, the observed angular dependence gradually diminishes, and by 350 K, the R_{L2} ratio becomes nearly independent of θ for both sample regions. This implies that, due to finite-size effects, the T_N of the 40-Å-thick NiO(111) is reduced compared to its bulk value. Fig. 4.5 (c) shows results of systematic temperature-dependent R_{L2} measurements conducted in normal incidence geometry (θ = 0), with **E** || NiO[$\bar{2}$11]||Fe[1$\bar{1}$0] at $\varphi = 0°$, above both sample regions. The difference of these two R_{L2} ratios, defined as, defined as $\Delta R_{L2}(\theta=0) = R_{L2(50\ Å)} - R_{L2(150\ Å)}$, is presented in Fig. 4.5 (d). Based on these findings, T_N of the 40-Å-thick NiO(111) layer is estimated to be approximately 380 K. This value is consistent with reported T_N of different NiO monolayers[126].

To explore the MA of both Fe(110) and NiO (111) sublayers, Fig. 4.6 shows a systematic angle-dependent measurements of both sublayers using MOKE and XMLD, respectively. The in-plane MA of the ferromagnetic Fe(110) sublayer was examined through angle-dependent MOKE measurements. The magnetization in the remanence state was determined and plotted as a function of the in-plane azimuthal angle φ, as illustrated in Fig 4.6 (left panel), using data obtained from magnetic hysteresis loops. These findings unequivocally establish the presence of a robust uniaxial in-plane MA. Specifically, for the 50-Å-thick Fe, the anisotropy favours the Fe[1$\bar{1}$0] easy axis, while for the 150-Å-thick Fe, it aligns with the bulk-like Fe[001] orientation. This twofold in-plane MA of Fe is mirrored by the MA of the neighbouring NiO. To investigate that, XAS spectra were measured at varying φ angles. For each φ angle, two spectra were obtained, one at θ = 0 (normal incidence) and the other at θ = 60° (close to grazing incidence). For these measurements $\Delta R_{L2} = R_{L2(\theta = 0°)} - R_{L2(\theta = 60°)}$ was defined and determined.

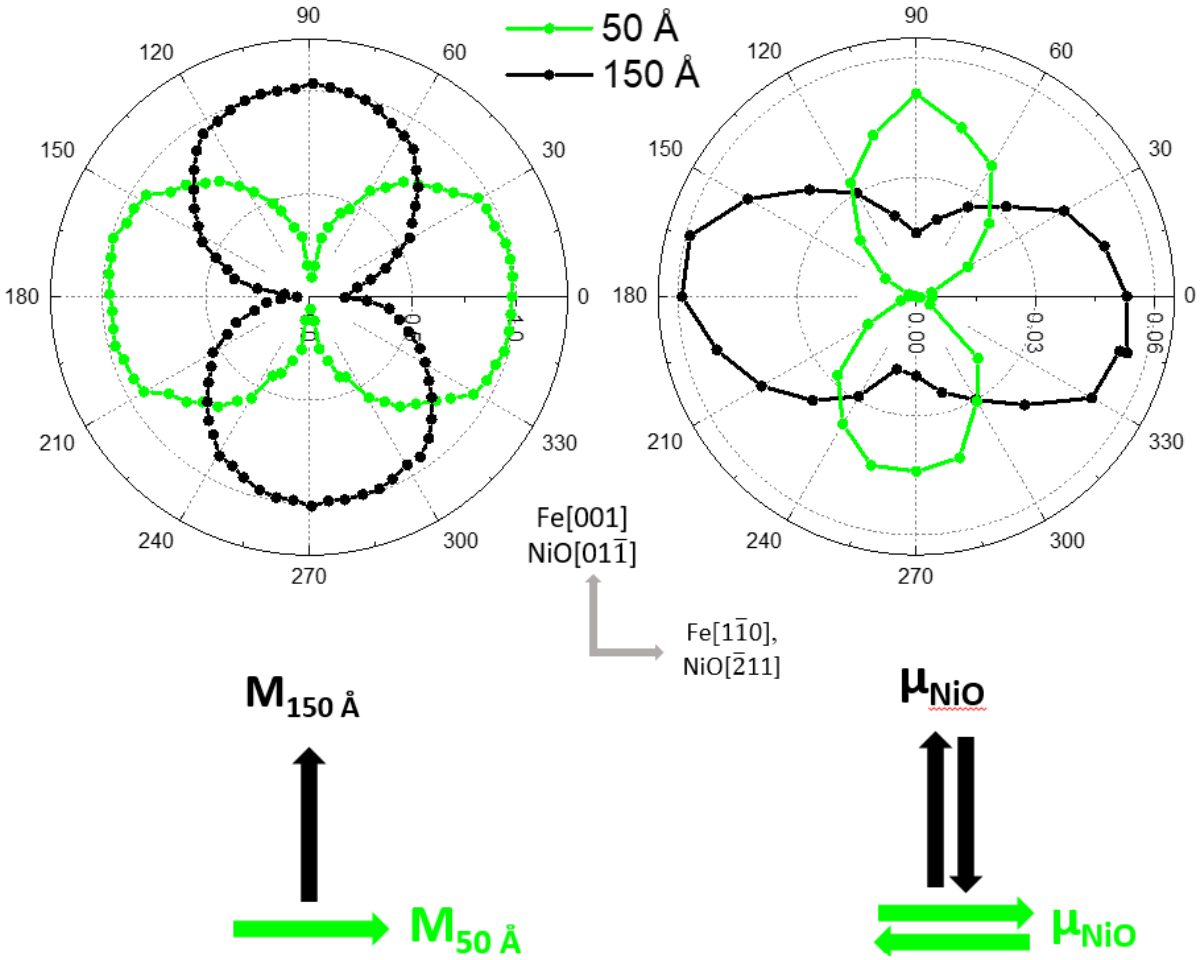

Fig 4.6 On the left side, in-plane angular dependencies of Fe magnetization in the remanent state, calculated from MOKE hysteresis loops. On the right side, XMLD magnitude defined by ΔR_{L2} (calculated as $R_{L2(\theta\ =\ 0°)} - R_{L2(\theta\ =\ 60°)}$) as a function of the azimuthal angle (φ). At the bottom of the image, arrows schematically indicate the easy axes of the FM Fe and AFM NiO sublayers for both sample regions. The 50- and 150-Å sample regions are coloured green and black, respectively.

In Fig. 4.6's right panel, plots of d ΔR_{L2} (φ) are presented for both thicknesses of the Fe sublayer. Unlike the threefold in-plane symmetry in bulk NiO(111) that is observed in previous works[127], the interaction with the adjacent Fe layer induces a twofold in-plane MA in NiO. The easy axis of NiO is determined by the FM's MA, aligning parallel to NiO[$\bar{2}$11]||Fe[1$\bar{1}$0] and NiO[0$\bar{1}$1]||Fe[001], for 50- and 150-Å-thick regions, respectively. In the NiO/50 Å Fe region, the XMLD effect vanishes along the Fe easy axis at $\varphi = 0$, but for NiO/150 Å Fe, it remains nonzero along the Fe easy axis at $\varphi = 90°$. This means that there is an additional MA of NiO above thick Fe film region.

The easy axis of thin Fe (Fe[$1\bar{1}0$]), coincides with NiO's easy axis (NiO[$\bar{2}11$]). Consequently, the NiO[$\bar{2}11$]||Fe[$1\bar{1}0$] orientation of AFM spins is favourable. However, in the NiO/150 Å Fe region, the easy axis of thick Fe (Fe[001]) does not align with any of NiO's easy axes (please see Fig. 4.1e) but lies precisely between two of them, causing an intrinsic contribution to NiO's effective MA and influencing angle-dependent XMLD results, leading to a nonzero value of dletaRL2 at $\varphi = 90°$.

Fig. 4.7 shows magnetic hysteresis loops for both Fe and NiO sublayers obtained using XMCD and XMLD, , respectively. The measurements involved applying an external magnetic field in a specific geometry ($\varphi = 0°, \theta = 60°$), aligning the in-plane component along the Fe[$1\bar{1}0$] direction. It's important to note that due to the substantial in-plane MA of Fe/W(110) films, the nonzero out-of-plane component of the external magnetic field does not affect the Fe magnetic state. This is because significantly higher fields are required to switch Fe(110) magnetic moments out of the (110) sample plane. For the 50 Å Fe region, below the critical thickness for SRT, a typical square hysteresis curve is observed. Conversely, the 150-Å-thick Fe exhibits a hard-axis loop with nearly zero magnetization in the remanent state. In the case of NiO sublayer, the external magnetic field has no effect on XMLD in the 50-Å-thin Fe region, as the XMLD does not sense the 180° reversal. However, in the 150-Å-thick Fe region, a change in R_{L2} is evident with changing the external magnetic field. This can be explained by considering the magnetization reversal of the thick Fe along its hard MA axis and the exchange coupling at the NiO/Fe interface.

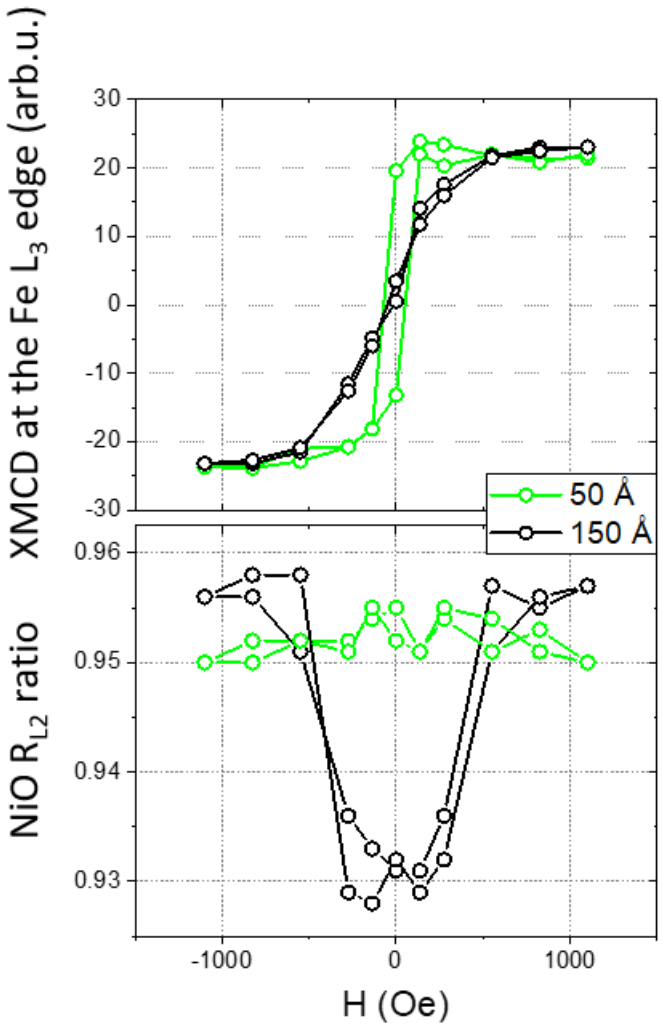

Fig. 4.7 Magnetic hysteresis loops for 150 Å and 50 Å regions of the sample, captured by XMCD (top) and XMLD (bottom) for Fe and NiO sublayers respectively.

The results in Fig. 4.7 show rotatable NiO spins in the NiO/Fe bilayer, and their orientation can be switched, for instance, by applying a ~500 Oe external magnetic field. This observation is confirmed by the absence of EB in NiO(111)/Fe(110) system, as indicated by the magnetic hysteresis loops of Fe (Fig. 4.7 top panel) which are symmetric around **H** = 0 axis. This observation was further validated through magnetic hysteresis loops obtained for NiO/Fe(110) bilayers using MOKE, such as the blue loop in Fig. 4.8 measured at 80 K for NiO/(50 Å Fe), where the external magnetic field was applied along the Fe[$1\bar{1}0$] direction. This finding implies that NiO spins exhibit full rotatability at low temperatures, likely due to the considerably smaller intrinsic MA of NiO compared to CoO (in chapter five). The lack of H_{EB} can be explained by potential spin-flop coupling between

Fe and NiO magnetic moments. However, such orthogonal coupling has already been ruled out by angle-dependent XMLD results shown in Figs. 4.5 and 4.6.

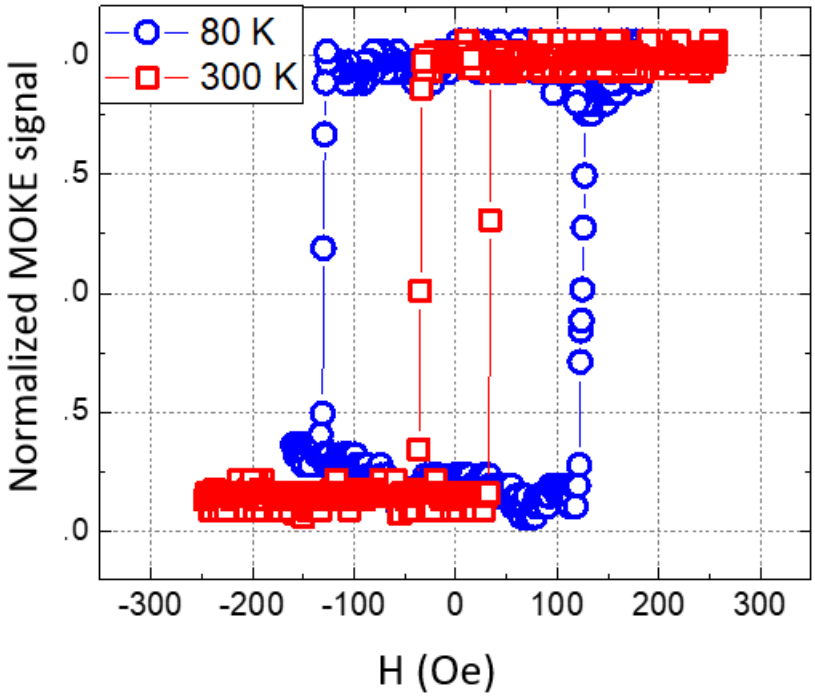

Fig. 4.8 Magnetic hysteresis loops on NiO/50 Å Fe region captured by MOKE at 300 and 80 K.

Fig 4.8 also shows that FM-AFM coupling leads to coercivity enhancement. The easy-axis hysteresis loops for the NiO/50 Å Fe region shown here were measured by MOKE at 300 K and 80 K. A substantial increase in coercive field can be observed when decreasing the temperature to 80 K. The alterations in coercivity induced by temperature can exclusively be ascribed to FM-AFM coupling, as in systems devoid of AFM influence, the coercive field of Fe(110) films demonstrates minimal dependence on temperature.

The interaction between the magnetic moments of NiO with the underlying Fe layer suggests the possibility of achieving field-free switching in AFM NiO states within a NiO/Fe system with uniform thicknesses of Fe and NiO. To achieve this, fine tuning of the thickness of the Fe sublayer is required. This precise tuning is essential to ensure that the effective in-plane MA of Fe approaches almost zero value, thereby placing the NiO/Fe bilayer in close proximity to the critical thickness of the Fe SRT.

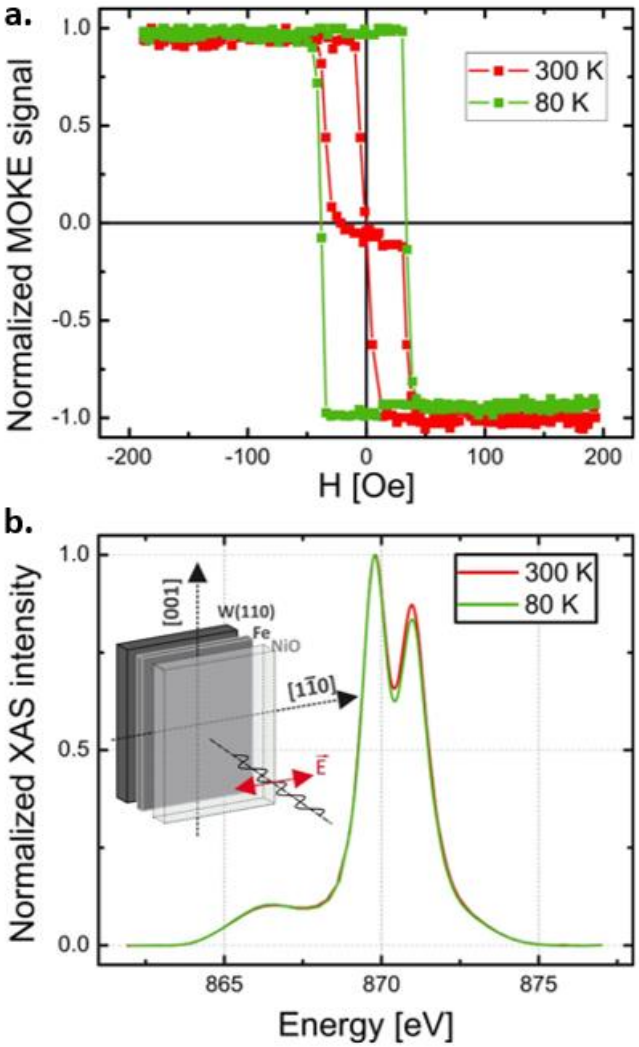

Fig. 4.9 (a) SRT in the 90 Å thick Fe sublayer driven by temperature. (b) The schematic representation of the XMLD experiment, and exemplary XAS spectra obtained with linear polarization of the photon beam. Both captured at 300 and 80 K are presented (red and green, respectively).

Fig. 4.9 (a) Hard and easy MOKE hysteresis loops documenting temperature driven SRT in 90 Å thick Fe sublayer. (b) The schematic sketch representing the geometry of the XMLD experiment and an exemplary XAS spectra acquired around L_2 edge for 90 Å Fe at 300 K and 80 K. Fig. 4.9 (a) shows that at 300 K (red curve), 90 Å Fe magnetization favours the Fe[1$\bar{1}$0] direction showing a typical hard loop captured by MOKE when the external magnetic field was applied parallel to Fe[001] direction. At this thickness Fe has a very small MA which makes it possible to switch its magnetization to [001]. This phenomenon in FM systems may occur due to the specific temperature dependence of MA constants, as mentioned in section 2.1.2.2 of this thesis. At 80 K, the green curve in Fig. 4.9 (a) confirms that

temperature induced SRT does take place in 40 Å NiO/ 90 Å Fe, as the Fe magnetization switch in-plane by 90° from $[1\bar{1}0]$ to [001] resulting in a square hysteresis loop. The normalized XAS spectra in Fig. 4.9 (b) confirm the temperature induced SRT in 40 Å NiO/ 90 Å Fe system, as the significant difference in the second peak of the spectra at 300 and 80 K indicates a temperature induced SRT in AFM as well.

To investigate further the temperature induced SRT in NiO(111)/Fe(110) bilayers, systematic temperature-dependent XAS measurements took place, focusing on three Fe thicknesses, namely 50 Å, 90 Å, and 150 Å. Fig. 4.10 shows the temperature-dependent behaviour of the normalized XMCD signal and XMLD data as defined by R_{L2} ratio. In case of 50 Å Fe, the magnetic spin structure is aligned along $[1\bar{1}0]$ direction, as verified by the temperature-dependent XMCD results in the top panel in Fig. 4.10 (triangles). Despite the anticipated increase in [001] in-plane MA of Fe(110) with decreasing temperature, this change is insufficient to prompt a rotation of the magnetization in the 50 Å Fe stripe. Conversely, a 150 Å thick Fe film exhibits temperature-independent magnetization along the in-plane [001] direction (squares in the upper panel of Fig. 4.10), with the [001] MA even strengthening as the temperature decreases. Due to FM-AFM coupling, in both cases d_{Fe} = 50 Å and d_{Fe} = 150 Å, the orientation of NiO magnetic moments, as indicated by the R_{L2} ratio in the lower panel of Fig. 4.10, is consistently fixed along NiO$[\bar{2}11]$||Fe$[1\bar{1}0]$ and NiO$[0\bar{1}1]$||Fe[001], respectively.

In the case of d_{Fe} = 90 Å, the Fe sublayer experience a temperature-driven in-plane SRT by 90° from Fe$[1\bar{1}0]$ to Fe[001] directions with decreasing the temperature. A substantial thermal hysteresis of this temperature-induced SRT is observed, spanning from 230 K to 270 K. Consequently, for each temperature within this range, there are two possible equilibrium states characterized by the orthogonal orientations of Fe magnetization. Due to the FM–AFM coupling between Fe and NiO sublayers, two orthogonal magnetic states are also observed in the antiferromagnetic NiO sublayer, which is evident from the temperature dependence of the R_{L2} ratio marked by circles in the lower panel of Fig. 4.10. On the cooling branch, within the temperature hysteresis, the magnetic state is stable with magnetic moments oriented along NiO$[\bar{2}11]$||Fe$[1\bar{1}0]$ direction, while in the heating branch, the system persists in the orthogonal NiO$[0\bar{1}1]$||Fe[001] orientation. The switching between these two orthogonal states of

NiO magnetic moments can be achieved through cycles of heating and cooling of the sample above 270 K and below 230 K, respectively.

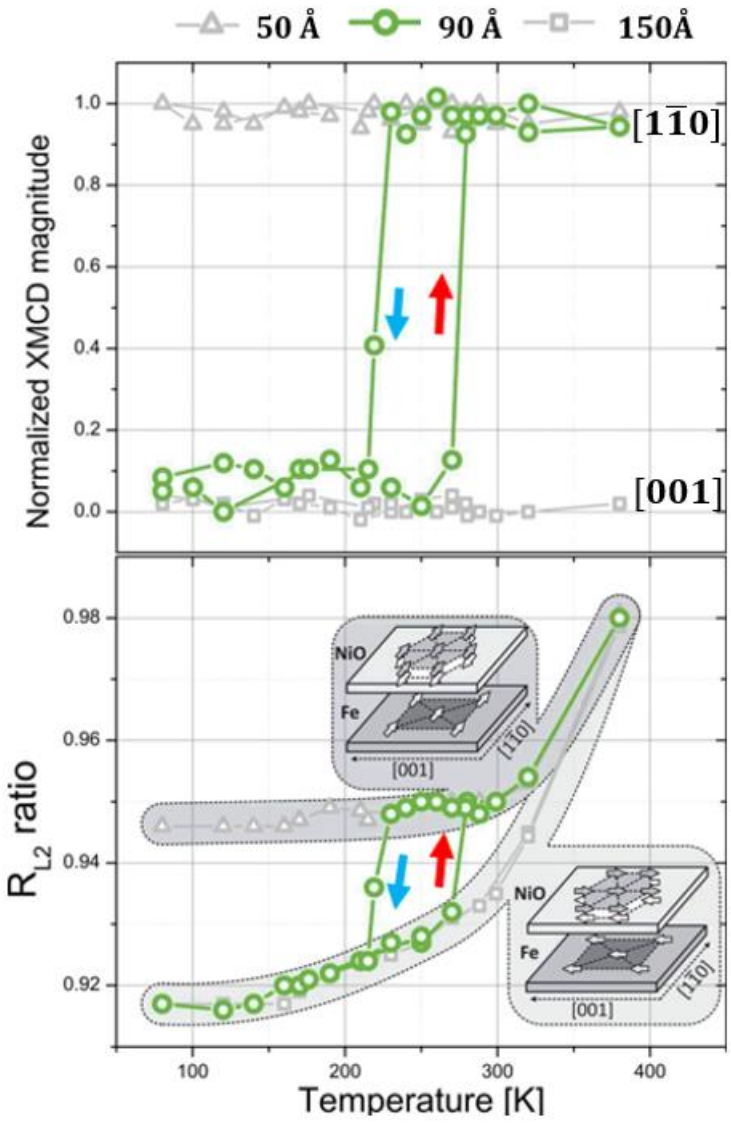

Fig. 4.10 Temperature dependence of XMCD and XMLD measurements on NiO(111)/Fe(110) system containing three different Fe thicknesses of 50 Å, 90 Å, and 150 Å.

To make more systematic experiment of such field free and temperature driven SRT on AFM, another sample consisting of 300 μm-wide Fe stripes in the range of thicknesses from 98Å to 113Å (see Fig. 4.11 (a)) was made. For such prepared sample, it requires a long time for stabilization at each temperature before the corresponding XAS measurement is performed because temperature change can lead to significant thermal

expansion and contraction of the manipulator that holds the sample. Consequently, due to time limitations in synchrotron facility, only the heating branch was measured contrary to the full thermal hysteresis measurements shown in Fig. 4.10. XMLD results defined by R_{L2} in Fig. 4.11 (b) show the temperature dependence for various thickness of Fe. These results show that depending on the thickness of Fe, the critical temperature, at which SRT occurs on NiO where the AFM moments switch from NiO[01$\bar{1}$]||Fe[001] to NiO[$\bar{2}$11]||Fe[1$\bar{1}$0], can be defined. With increasing the thickness of Fe, the critical temperature constantly increases. For this system, the results showed that Fe thicknesses that SRT occurs at are in the range from 98Å to 113Å .

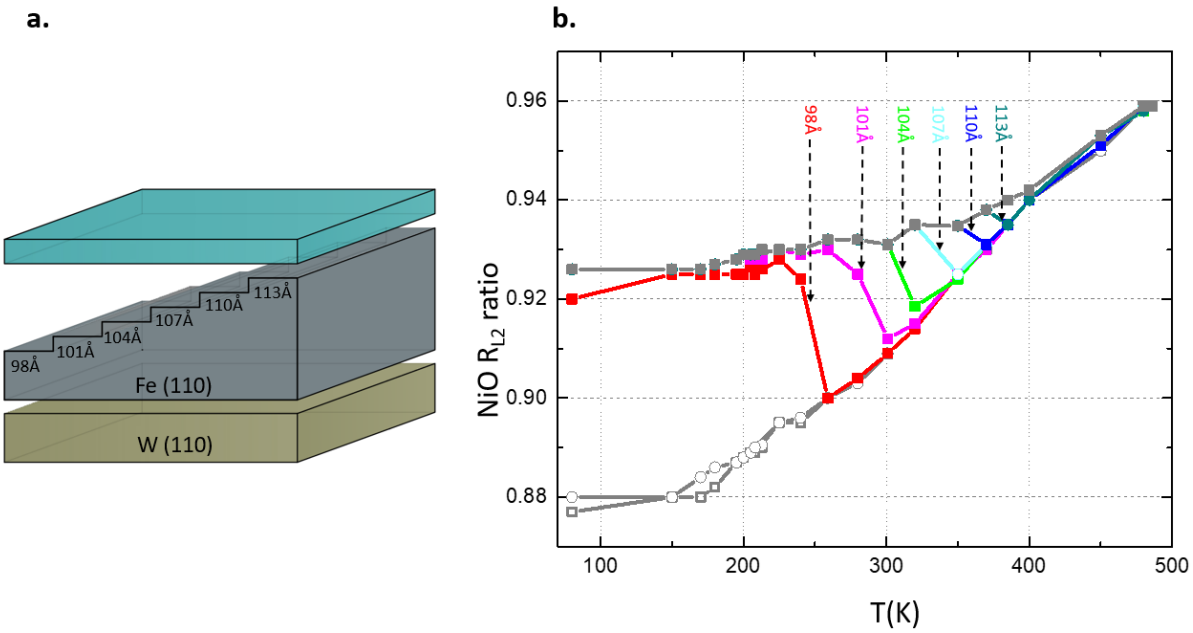

Fig. 4.11 (a) Schematic sketch of the sample showing the Fe thicknesses at which temperature induced SRT occurs. (b) Temperature dependence of R_{L2} ratio for various Fe thicknesses of the sample (colour coded) shows the temperature driven SRT.

5. Chapter five: CoO(111)/Fe(110)

5.1. Introduction

CoO/Fe is one of the intensively studied AFM/FM systems with the large potential in terms of exchange bias and frozen antiferromagnetic spins studies [128,129]. More precisely, such studies were mostly conducted for (001) oriented CoO/Fe systems [130–133], while bilayers including CoO(111) was rarely studied and often focused only on the magnetic hysteresis loops.[134]. This chapter investigates the magnetic properties of CoO(111)/Fe(110) bilayers either by conducting XMLD measurements, which is considered as a direct probe of AFMs magnetic properties, or by an indirect method in which the exchange bias is treated as a tool sensitive to orientation of AFM spins at the AFM/FM interface.

By making use of the previously mentioned controllable MA of Fe(110) sublayer, a large EB effect can be observed below T_N of CoO overlayer can be seen, and the orientation of the of frozen CoO spins has a kind of memory of the magnetic state of Fe above T_N.

5.2. Sample preparation

Similar to the previous systems, Fe was grown on atomically clean W(110) single crystal at RT using MBE to form two different thicknesses, namely 50 Å and 200 Å, by making use of the shutter to shadow the sample while depositing the iron. Then the film was annealed to 675 K for 10 minutes to produce atomically smooth Fe(110) surface. These two thicknesses of Fe(110) allow us to have two different magnetic anisotropies in one system, namely, 50 Å Fe with the easy axis along $[1\bar{1}0]$ (below the critical SRT for Fe) and a bulk-like 200 Å Fe region spontaneously magnetised along [001] in-plane direction.

Next, a homogenous 45 Å CoO(111) overlayer was grown by depositing Co in O_2 atmosphere (i.e., $1x10^{-6}$ Torr) at RT.

5.3. Results

Our MOKE and XMLD results on CoO(111)/Fe(110) systems showed that CoO magnetic spins follow the thickness induced spin reorientation transition in underlaying Fe. To follow the local orientation of magnetic moments of CoO, XMLD technique was used at PIRX end-station of the Polish Synchrotron Radiation Centre SOLARIS. Fig. 5.1 (a) shows the schematic structure of the system and the geometry of the XMLD experiment, where the normal incidence geometry ($\theta = 0$) was firstly used, and the vector of incoming linearly polarized X-ray beam was parallel to the Fe$[1\bar{1}0]$ in-plane direction.

The comparison of XMLD spectra on the CoO/50 Å Fe and CoO/200 Å Fe sample regions is treated as the evidence of the SRT on CoO layer induced by the SRT on Fe sub-layer. The so called R_{L3} ratio is considered as the fingerprint of the CoO magnetic moments orientation. It is determined as the ratio of the XAS intensity at 777.2 eV and at 779.8 eV energies where two out of four characteristic intensity peaks are visible in typical CoO absorption spectrum, as shown in Fig. 5.1 (b). XAS spectra collected at RT with linear polarization of the photon beam (shown in Fig. 5.1 (c)), on both regions of the sample are identical since CoO is paramagnetic at temperature above its T_N.

The XAS spectra for the two Fe thicknesses show significant differences after the sample has been cooled down in its remanent magnetic state (without an external magnetic field), which indicates a 90° SRT, please see Fig. 5.1 (d). Here, it is important to point out that CoO spins stay frozen along the local easy axis of CoO as long as the system remains under CoO T_N and independently on the current magnetic state of neighbouring Fe layer, that can be for example changed by applying an external magnetic field [135,136] during magnetization reversal process. To demonstrate that, this antiferromagnetic CoO component of the system was "defreezed" by heating the system to 300 K followed by subsequent cooling down to 80 K with an external magnetic field (1500 Oe) applied along the in-plane direction Fe$[1\bar{1}0]$ (which is a hard axis for 200 Å Fe). In these circumstances, both sample regions are magnetized along $[1\bar{1}0]$ direction as the system passes CoO T_N which at 80 K leads to identical XAS spectra for both sample areas, also after releasing the

external magnetic field. This is shown in Fig. 5.1 (d) when comparing XAS spectra for 50 and 200 Å regions, marked by the green solid line and open symbols, respectively.

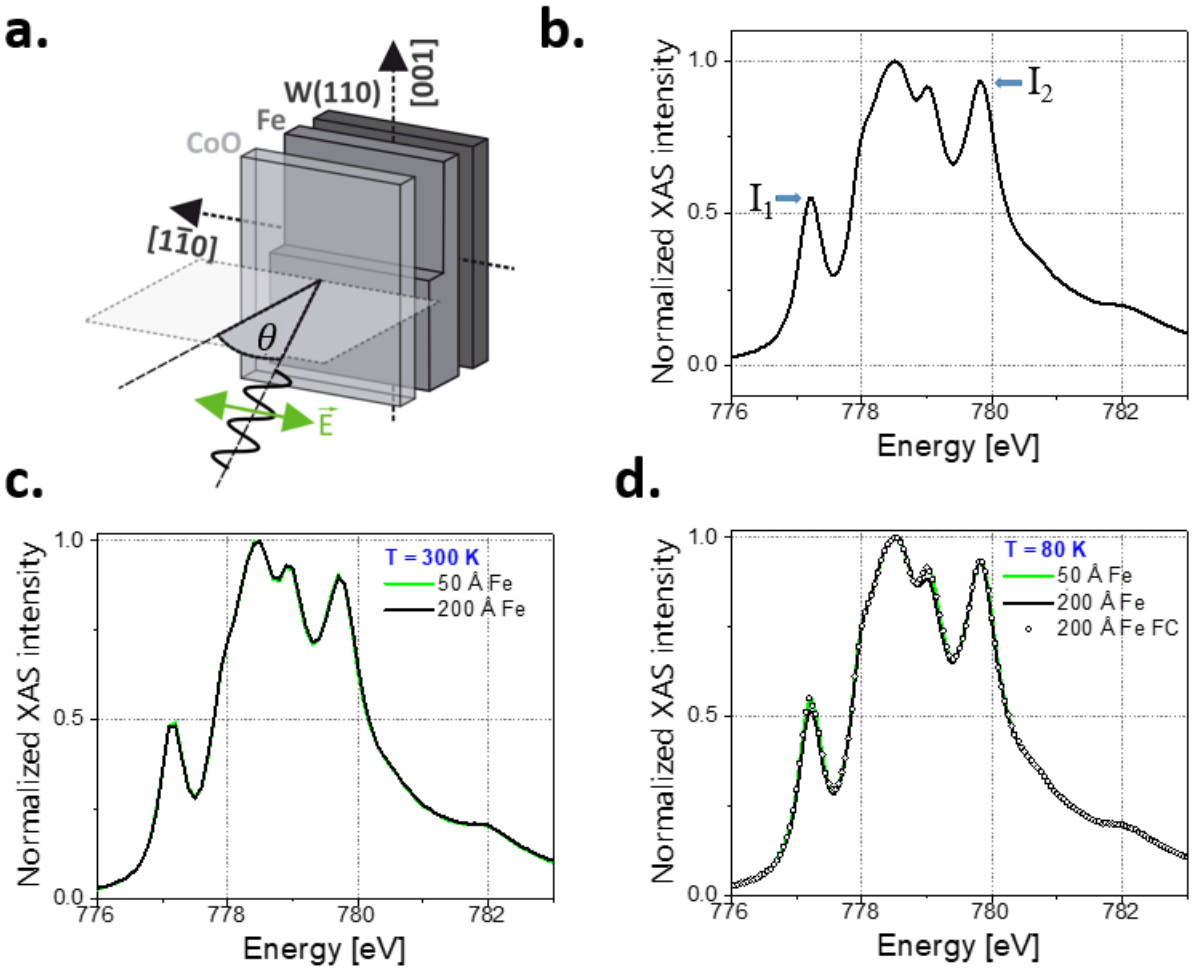

Fig. 5.1 (a) Schematic representation for XMLD experiment geometry, (b) exemplary XAS spectrum acquired with linear polarization around L_3 edge of Co, I_1 and I_2 are the intensities of the two chosen absorption peaks that are used to define the R_{L3} ratio. XMLD measurements acquired at 80 K and 300 K for both sample regions are shown in (c) and (d). The open symbols in (d) represent the XMLD measurement that was performed on 200 Å thick area after the sample was field-cooled with an external magnetic field applied along [1$\bar{1}$0] direction.

In general, the XLD effect can originate from both the AFM ordering and crystal field effect[137]. Contrary to crystal-field effect, the AFM contribution vanishes above T_N. In order to follow the angle and temperature dependence of XMLD effect it is convenient to

define the differential R_{L3} ratio $\Delta R_{L3} = R_{L3(50\ Å)} - R_{L3(200\ Å)}$. In Fig. 5.2 (a), ΔR_{L3} ratio dependence on polar angle θ is presented, as measured at 80 K. Clearly, the maximum of XMLD effect is observed for normal incidence geometry, in which a full in-plane sensitivity of XMLD to orientation AFM spins is available. This proves that due to exchange interaction with neighbouring ferromagnetic layer the CoO antiferromagnetic spins are forced to lie in CoO(111) || Fe(110) sample plane. In Fig. 5.2 (b) temperature dependence of ΔR_{L3} is shown for normal incidence geometry of the XMLD measurements. One can see that for 45 Å-thick CoO layer its T_N is roughly equal to bulk value (293 K) for CoO. Close to zero ΔR_{L3} value above 300 K confirms that XLD effect in CoO(111)/Fe(110) system is almost fully of magnetic origin.

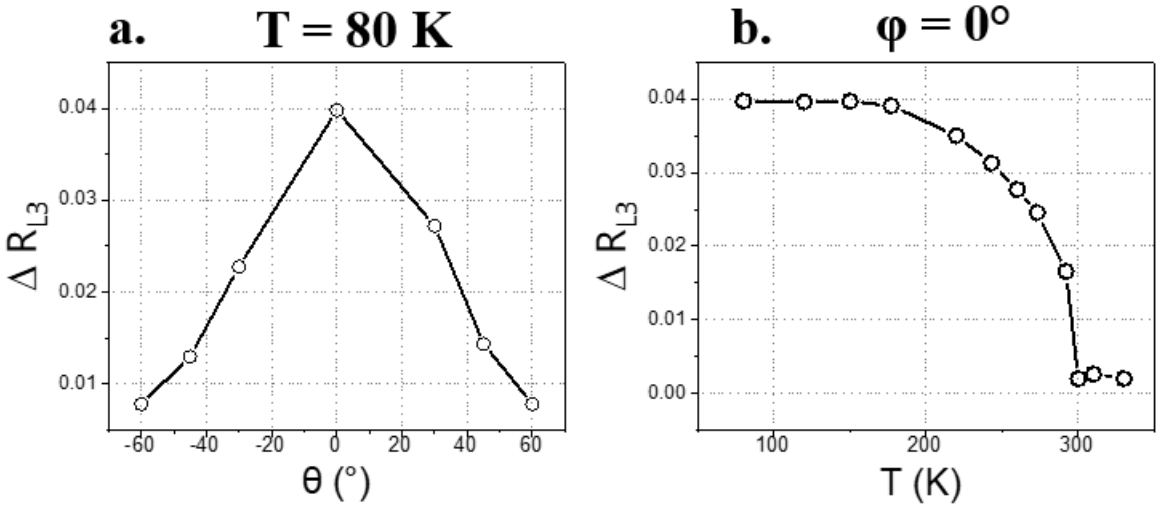

Fig. 5.2 $\Delta R_{L3} = R_{L3}(50\ Å) - R_{L3}(200\ Å)$ as a function of the polar angle (a) and the temperature (b). The temperature dependence of ΔR_{L3} was obtained for a fixed polar angle $\theta = 0$.

In following part of this chapter, the magnetic properties of CoO(111)/Fe(110) bilayers as probed by MOKE hysteresis loops will be investigated. The clearest indication of the probe of the AFM spins orientation in MOKE measurements is the field shift of the magnetic hysteresis loop caused by the exchange bias effect. Fig. 5.3 (a-d) shows MOKE measurements of CoO/50 Å Fe and CoO/200 Å Fe regions on the sample conducted at RT for two orthogonal in-plane orientation of the applied magnetic field. When the applied magnetic field was along the easy axis of the 50 Å Fe region (**H**|||[1$\bar{1}$0]), a characteristic square (easy) hysteresis loop is observed (Fig. 5.3a), while a typical hard axis loop is, as expected, observed for the CoO/200 Å Fe region of the system Fig. 5.3b. On the other hand, it was also expected to see exactly the opposite set of hysteresis loops when applying the magnetic field along the axis which is the easy one for 200 Å Fe sample region (**H**|||[001]). Giving that 300 K is above CoO T_N, no exchange bias was observed which agrees with the XMLD results in Fig. 5.1 (c).

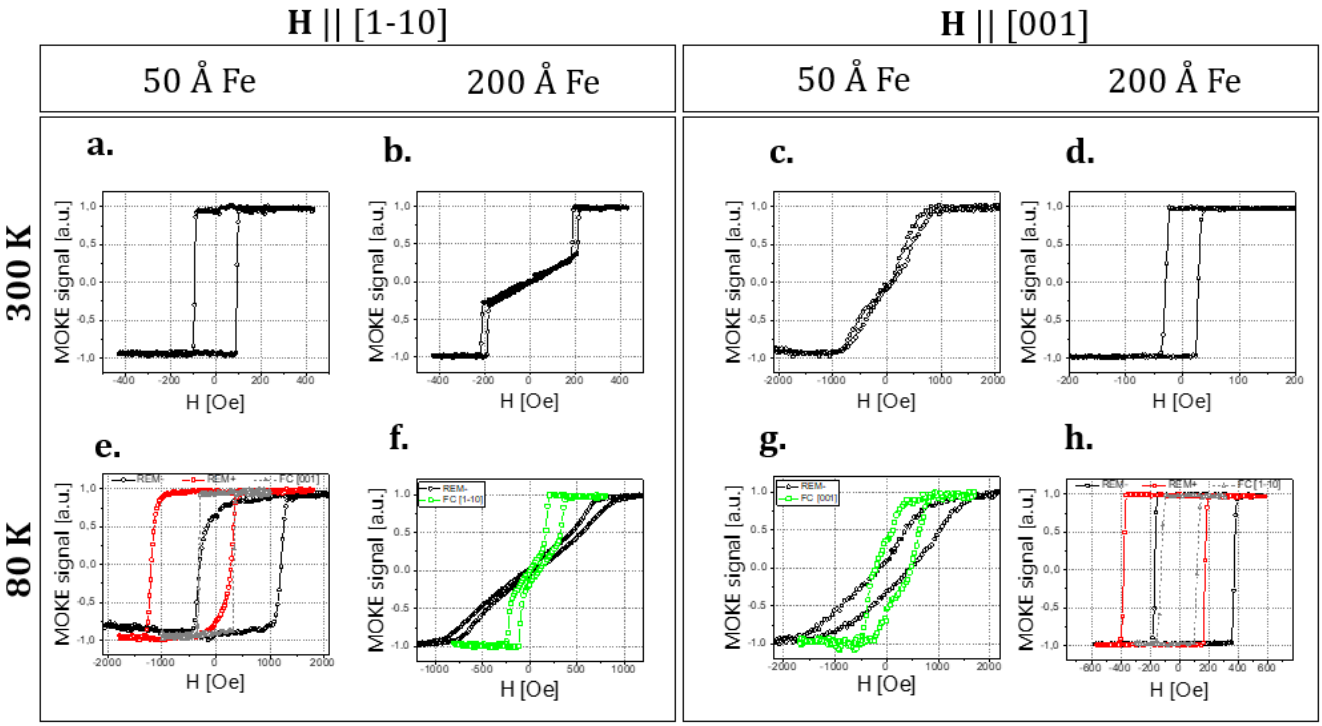

Fig. 5.3 Magnetic hysteresis loops for CoO/50 Å Fe and CoO/150 Å Fe acquired using longitudinal MOKE. Two in-plane orientations of the applied external magnetic field, namely **H**|||[1$\bar{1}$0] and **H**|||[001] are shown for 300 K measurements (a-d) and 80 K (e-h) measurements. The red hysteresis loops

correspond to the square (easy) measurements after cooling down in „positive" remanent state of the sample (REM+). Black curves for the low temperature measurements correspond to cooling in "negative" remanent state of the sample (REM-). Green curves correspond to hard axis loops after cooling down in the presence of an external magnetic field applied along particular hard axis. The grey dashed loops correspond to easy axis loops (in e and h) for both regions of the sample after FC procedure where the field is applied along particular hard axis of Fe.

Moving on to the 80 K measurements, please note that for measurements along easy axes the system can be cooled down in one of its remanent states (referred in Fig. 5.3 as 'REM -' or 'REM +'). These two remanent states of the sample correspond to magnetic states after applying the magnetic field at 300 K along the easy axis $[1\bar{1}0]$ (REM-) or along antiparallel $[\bar{1}10]$ direction (REM+) in case of Co/50 Å Fe region. The same applies to CoO/200 Å Fe region where the magnetic field was applied once along [001] (REM+ state), and once along antiparallel [00-1] (REM- state). On the other hand, identical result for REM+ and REM- on the hard axis hysteresis loops should be expected, giving that the magnetic spins go back to its easy axis once the field is released in both scenarios. The first noticeable thing in 80 K measurements is the large exchange bias on easy axis areas, Fig. 5.3 (e) and (h), where the field shift approaches ~ 400 Oe at Fig. 5.3 (e, 50 Å Fe region) and ~ 100 Oe at Fig. 5.3 (h, 200 Å Fe region). These values of H_{EB}, as expected, fit well to the $1/d_{Fe}$ dependence of the exchange bias. It is also worth noting that from the exchange bias results, one can conclude that cooling down the system in the remanent state of 50 Å Fe easy direction $[1\bar{1}0]$, results of imprinting this orientation to the CoO frozen spins once the system passes T_N and similarly with the 200 Å Fe easy axis [001] which will be imprinted on the CoO frozen spins on this region, which agrees with the XMLD results in Fig. 5.1 (d).

It is important to point out that cooling down the sample in the REM+ remanence state of thin Fe $[1\bar{1}0]$ leads to the opposite field shift as compared to cooling down in the second REM- remanent state, which is key evidence for the influence of the remanent state of Fe on the 0/180° orientation of interfacial CoO spins after passing T_N. Another way to prove this influence of Fe on the CoO spins is to cool down the system while applying an external magnetic field (field cooling) along the direction of the hard axis of Fe (**H**||[001] for 50 Å Fe and **H**||$[1\bar{1}0]$ for 200 Å Fe). This procedure results in CoO spins

oriented along the hard axis of Fe after passing T_N. Importantly, at low temperature these AFM spins stay frozen along this direction once the external magnetic field is released. Such procedure leads to non-biased, fully symmetric with respect to zero field axis and easy-like magnetic hysteresis loop , please see grey loops in Fig. 5.3 (e) and (h).

As expected, the hard loops at 80 K (Fig. 5.3 (f) and (g) black curves) are symmetrical and bias-free, however, they have larger anisotropy field compared to the corresponding hard loops at RT, see Fig.5 b and c. Cooling down the system with an external magnetic field applied along the hard direction of Fe will result with a noticeable exchange bias on the hard loops (Fig. 5.3 (f) and (g) green curves), H_{EB} of ~150 Oe for CoO/50 Å Fe and ~45 Oe for CoO/200 Å Fe. Specifically, cooling procedure with the external magnetic field applied along [001] for CoO/50 Å Fe (so along its hard axis) will force the AFM spins to align to this direction, leading to significant loop asymmetry (EB shift field) and reduction of anisotropy field after such hard axis-FC procedure as compared to the anisotropy field obtained by cooling in remanent state, see Fig. 5.3 (g). In analogy for the CoO/200 Å Fe region, FC with magnetic field applied along its hard axis (**H**||$[1\bar{1}0]$) forces CoO spins to align along this direction and results in exchange biased hard-like loop (Fig. 5.3 f, green) with reduced anisotropy field as compared to hard loop measured at low temperature after cooling in remanent state (black loop in Fig. 5.3 f)

This can be easily understood having in mind that EB is a kind of additional (unidirectional) MA that turns on after field-cooling procedure. In case of CoO/200 Å region (Fig. 5.3 (f)) exchange bias provides magnetic contribution to the energy of the system preferring $[1\bar{1}0]$ type of MA and so anisotropy field for **H** || $[1\bar{1}0]$ LMOKE geometry is smaller as compared to scenario without EB. The same explanation concerns Fe[001] anisotropy field and EB for CoO/50 Å area (Fig. 5.3 (g)). Such EB-induced modification of ferromagnetic component anisotropy seems to be interesting result as it shows a true interplay and bilateral nature of FM-AFM interaction. It is the RT FM uniaxial MA that can be used to tailor a desired orientation of AFM spins, but in response, the AFM component modifies the low temperature MA of FM sublayer. In order to follow such EB – anisotropy interplay in detail, temperature dependent MOKE measurements were performed.

Giving that FC procedure is time consuming and difficult to conduct during temperature dependence measurements, it was more logical to study the exchange bias

along with the anisotropy field in easy axis MOKE loops as a function of the temperature of the measurement. As shown in Fig. 5.3 measurements, it is expected that increasing the exchange bias along given direction will result in hysteresis loops with lower anisotropy field in the direction that is orthogonal to the external magnetic field. The temperature dependence results in Fig. 5.4 confirm the hypothesis, where the exchange bias H_{EB} and the anisotropy field H_{an} can be seen, as a function of temperature for both regions CoO/50 Å Fe and CoO/200 Å Fe (Fig. 5.4 (a) and (b) respectively).

Cooling the system in a remanent state makes the $H_{EB[1\text{-}10]}$ and $H_{EB[001]}$ of 50 Å and 200 Å areas, respectively, increasing and as a result corresponding anisotropy field $H_{an[001]}$ ($H_{an[1\text{-}10]}$) is also strongly increasing, please see Fig. 5.4 (a & b). This is because EB is now additional "force" that has to be overcome by external magnetic field in order to saturate Fe sublayer. The results for CoO/Fe(50 Å)/W(110) can be compared to the work done by Fruchart et al. on W(110)/Fe(60 Å)/W(110) epitaxial system[138], where MOKE hysteresis curves acquired with **H**||[001] indicate decrease of anisotropy field from ~200 Oe at 300 K to ~100 Oe at 133 K. This again supports the above interpretation. In the absence of antiferromagnetic overlayer, decreasing temperature makes the [001] axis preferred ($H_{an[001]}$ is decreasing) in contrast to CoO/Fe report where the onset of EB supports $[1\bar{1}0]$ orientation of Fe magnetization at low temperature (strong increase of $H_{an[001]}$ in Fig. 5.4 (a)). In Fig. 5.4 (b) CoO(111)/Fe(110) results are compared with H_{an}(T) temperature dependence determined for isostructural NiO(111)/Fe(110) bilayer, for which no H_{EB} is present, as shown in chapter four. Obviously, anisotropy field H_{an} in H_{EB} - free NiO/Fe system is much less temperature dependent as compared to exchange-biased CoO/Fe. One possible explanation for the clear differences in results for NiO/Fe and CoO/Fe may rely on the fact that there is a big difference between the ordering temperature of both AFMs, ~520 and ~290 K, respectively. For NiO(111)/Fe(110) sample, applying FC procedure with starting temperature 550 K (above the T_N of NiO) does not lead to the onset of EB and also does not freeze the AFM spins of NiO. This means that NiO spins are fully rotatable at low temperature which can probably be attributed to much smaller intrinsic MA of NiO as compared to magnetically hard CoO, this subject will be studied in detail as a continuation of work presented in the present thesis[76,142].

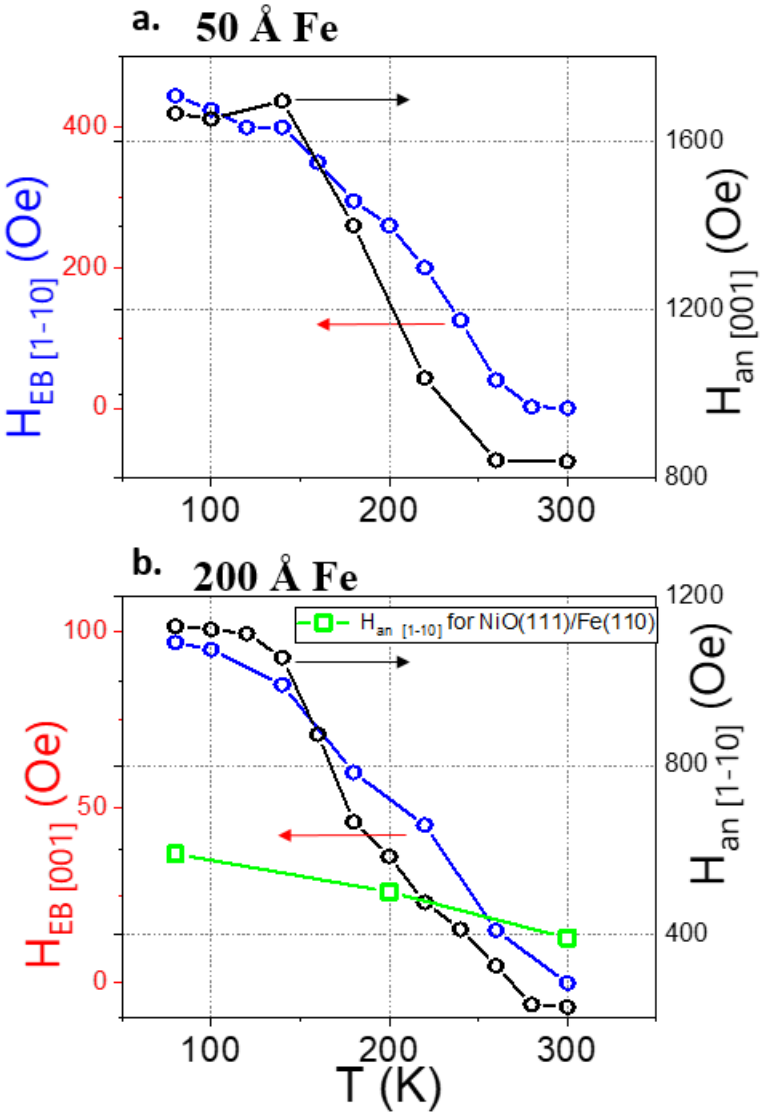

Fig. 5.4 Temperature dependence of the field shift (H_{EB}) acquired from MOKE easy hysteresis loops where the magnetic field was applied along [$1\bar{1}0$] in the top panel (a) for 50 Å Fe, and along [001] in the lower panel (b) for 200 Å Fe. The anisotropy field (H_{an}) corresponding to the hard axis hysteresis loops for 50 Å Fe where the field was applied along [001], and for 200 Å Fe where the field was applied along [$1\bar{1}0$] is also shown in (a) and (b), respectively. For comparison, the temperature dependence of anisotropy field $H_{an}(T)$ determined for exchange bias-free, isostructural NiO(111)/Fe(110) system is shown in (b, green).

In summary of this chapter, two surface-sensitive techniques were used, namely XMLD and MOKE as direct and indirect probes for AFM spin orientation at the FM/AFM interface, respectively. The advantage of XMLD is its direct nature and its sensitivity to the preferred AFM spin axis. However, indirect exchange bias studies using MOKE can be useful to detect the 0/180° orientation of the frozen AFM spins along specific axis of interest, while in such case XMLD technique is insensitive. These results highlight the possibility to influence the orientation of the frozen AFM spins by playing with the magnetic state and/or the anisotropy of the neighbouring FM layer above the T_N. On the other hand, due to the bilateral nature of the AFM-FM interaction, the strength of the FM anisotropy below the T_N is strongly modified depending on the certain orientation of the AFM spins is imprinted by a FM at the vicinity of T_N. Such AFM-FM interplay was further studied in detail for CoO/Au/Fe system, where the Au spacer serves as a convenient tool to control the AFM-FM interaction strength, as will be shown in the next chapter of this thesis.

6. Chapter six: CoO(111)/Au(111)/Fe(110)

6.1. Introduction

Typically, the most easily measurable quantity related to exchange bias is the horizontal shift of the magnetic hysteresis loop. However, drawing conclusions solely from the H_{EB} can be challenging or even impossible, as both the MA of the ferromagnet and antiferromagnet can play decisive roles in establishing and determining the magnitude of the exchange bias. For example, if the MA of the AFM is too low, the AFM spins may rotate along with the FM magnetization during reversal, resulting in enhanced coercivity but a fully symmetric magnetic hysteresis loop with respect to its zero-field axis[139,140]. Even when the intrinsic MA of the AFM is sufficiently large to induce exchange bias, the induced unidirectional MA may be noncollinear with the orientation of the external magnetic field used during film growth or FC procedures[141]. The situation becomes further complicated by the fact that the MA of the FM layer can also contribute significantly to the exchange bias in certain cases where it is not expected, such as when the magnetic field during magnetization reversal is perpendicular to the field applied during the FC procedure[142–144]. Considering these complexities, it is necessary to study exchange bias in single systems where both MAs and the strength of the AFM-FM interaction are well-defined and controllable.

The objective of this chapter is to investigate the interplay between uniaxial and unidirectional magnetic anisotropies in exchange-coupled FM/AFM systems and tune them by manipulating the strength of indirect exchange coupling or adjusting the balance between surface and volume contributions to the MA in the FM layer. To achieve this, a system of epitaxial CoO(111)/Au(111)/Fe(110) trilayers grown on W(110) single crystals was made. By incorporating a wedged FM bottom layer in the stack, it was possible to control its in-plane uniaxial MA, including both the smooth evolution of its strength and the change in its sign. The latter is evident in already described and used as a tool to control magnetism of NiO and CoO in two previous chapters, SRT [44,145,146], where a critical Fe thickness leads to a 90-degree in-plane switching of the Fe easy axis[37,40,119,147,148]. The strength of FM-AFM interaction and the resulting unidirectional MA were modulated by varying the thickness of a non-magnetic (NM) spacer in the wedged Au sublayer. To track the evolution of the effective in-plane MA of the FM layer, the

unidirectional MA axis, and the strength of the exchange bias effect, magnetic hysteresis loops were measured and analyzed in a two-dimensional (d_{Fe}, d_{Au}) space.

6.2. Sample preparation

The sample was prepared in UHV conditions and consists of an iron wedge (40 Å -140 Å) covered by orthogonally wedged Au sublayer (0-15 Å) with a so-called chimney of 30 Å-thick macroscopic Au region (please see Fig. 6.1). The iron was grown on an atomically clean W(110) single crystal using MBE at RT. To produce a high-quality smooth Fe (110) surface[120], the film was annealed to 675K for 10 minutes, similarly to samples described in two previous chapters. The same procedure followed the Au deposition, in this case the annealing temperature was adjusted to 500 K which resulted in a good quality crystal surface structure as confirmed by LEED. Next CoO layer was prepared by covering the entire surface of the sample with 60 Å of CoO, grown by reactive deposition of metallic Co in an O_2 atmosphere (partial pressure of 1×10^{-6} Torr).

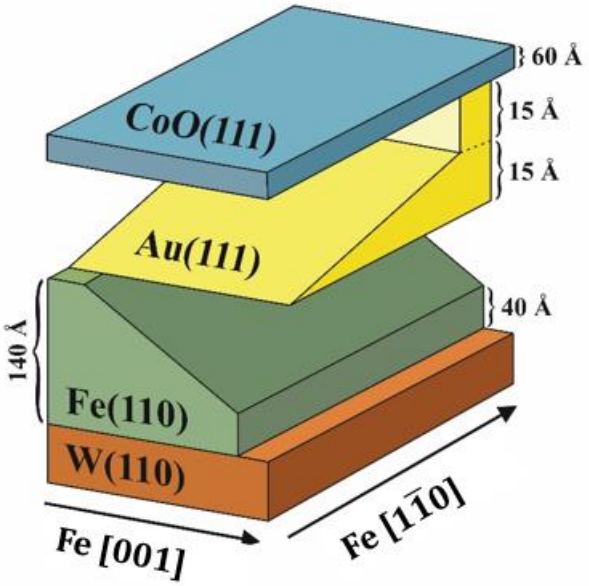

Fig. 6.1 Schematic picture showing the macroscopic architecture of the sample, along with in-plane the crystallographic directions of Fe(110) sublayer.

In Fig. 6.2, the LEED diffraction patterns are shown, acquired at subsequent stages of CoO(111)/Au(111)/Fe(110) sample preparation. The dark spots in the LEED images refer to the diffraction pattern of the surface of the sample at each preparation step. On the lower panel, corresponding ball models of Fe(110), Au(111) and CoO(111) are presented.

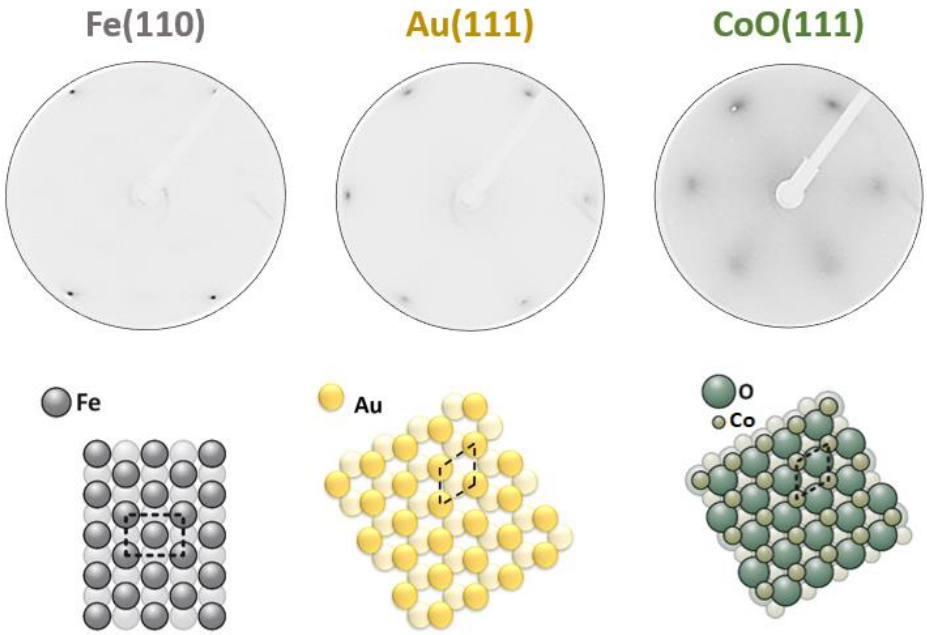

Fig. 6.2 Diffraction LEED patterns of the surface of: Fe(110), captured at electron energy E = 50 eV, Au(111)/Fe(110), captured at E = 55 eV and CoO(111)/Au(111)/Fe(110), captured at E = 80 eV. The bottom panel shows corresponding ball models.

6.3. Results

The magnetic properties of the CoO(111)/Au(111)/Fe(110) trilayers were initially visualized in situ using a longitudinal magneto-optic Kerr effect (MOKE)

microscope. Fig. 6.3 (a) displays a differential MOKE image of a selected area in the remanent state after the application of an external magnetic field aligned along the Fe[$1\bar{1}0$] in-plane direction. To enhance magnetic contrast and highlight characteristic features in the sample, a reference image taken at a small external magnetic field along [$1\bar{1}0$] was subtracted from the remanence image (H = 0). As a result, the dark region represents areas where the remanent magnetization remained along the saturation direction, [$1\bar{1}0$], while the brighter region corresponds to the magnetization direction along [001] in the remanent state. This conclusion was drawn, for instance, by comparing the hysteresis curves of regions of interest E and B or F and C. To obtain higher-quality hysteresis loops, the results presented in Fig. 6.3 (b) were obtained using an ex situ standard MOKE setup (not in microscopic mode). Additionally, XMLD and XMCD techniques were employed to confirm that the CoO overlayers effectively protected the samples from ambient conditions, enabling the investigation of their magnetic properties' ex situ without the need for additional capping layers.

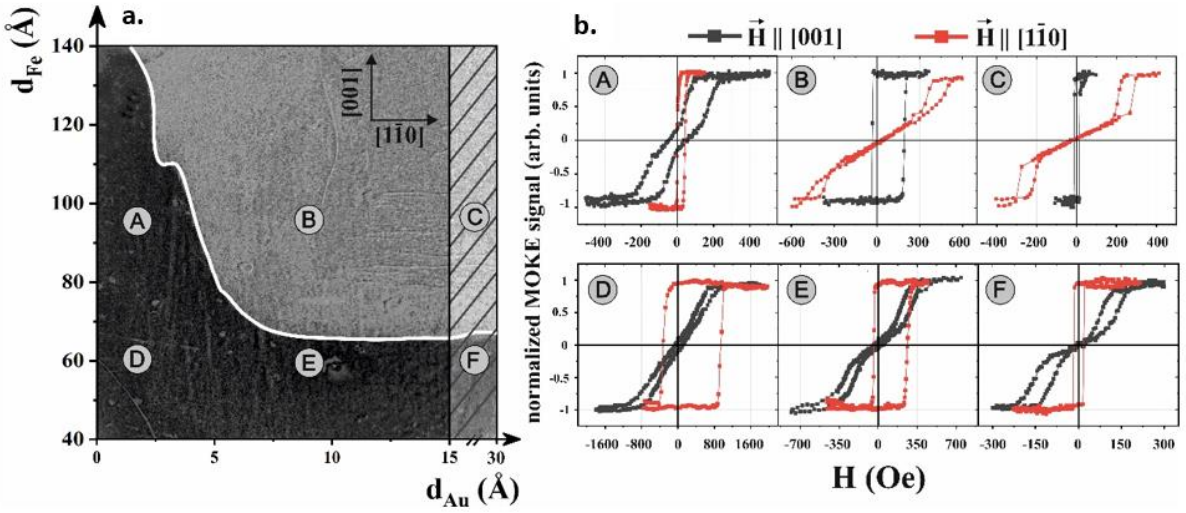

Fig. 6.3 (a) Differential MOKE microscope image of the system. The magnification of the MOKE microscope was intentionally tuned to cover the chosen field of view which is 4.6 mm (horizontal) x 4.0 mm (vertical). (b) MOKE hysteresis loops for two orthogonal directions of the external magnetic field as measured for selected regions of interest A-F defined in (a). Presented MOKE results were obtained at 80 K.

Fig. 6.3 (a) illustrates the marking of six representative regions of interest (ROIs: A, B, C, D, E, and F), and corresponding low temperature MOKE hysteresis loops that are

presented in Fig. 6.3 (b). Square hysteresis loops, also indicative of exchange bias, are observed for ROIs D and A when the external magnetic field is oriented along the Fe[$1\bar{1}0$] direction (red plots in Fig. 6.3 (b)). This suggests that, for this specific Au thickness (~2Å), Fe's easy axis is independent of its thickness and aligned with [$1\bar{1}0$], at least up to d_{Fe} = 140 Å. It should be noted that for d_{Au} < 2Å, the spin reorientation transition (SRT) to Fe[001] orientation of magnetization would occur above d_{Fe} = 140 Å, which is the maximum Fe thickness studied in this chapter. This observation is supported by the magnetic hysteresis loops measured in the complementary MOKE geometry with **H** || [001], where characteristic hard axis loops with magnetization close to zero in the remanent state are observed (gray plots in Fig. 6.3 (b)). A different conclusion can be drawn from the comparison of ROIs E and B (d_{Au} = 9 Å), as well as F and C (d_{Au} = 30 Å, 'chimney' region). In both cases, with increasing Fe thickness, an in-plane SRT from Fe[$1\bar{1}0$] to Fe[001] bulk-like easy axis is observed. Specifically, the magnetic hysteresis loops transition from 'square' to 'hard-like' for **H** || [$1\bar{1}0$] geometry (red color), and vice versa for **H** || [001] (gray color). Moreover, in the 'chimney' area, the exchange bias effect is completely suppressed, and the magnetic hysteresis loops both before (F) and after (C) SRT are symmetric with respect to the zero-field axis. These initial observations provide an overview of the sample's magnetic properties in the two-dimensional (d_{Fe}, d_{Au}) space. The continuous white line in Fig. 6.3 (a) denotes the critical SRT border in this space, which exhibits a significant decrease in thickness with d_{Au} and hints of oscillations, particularly visible around d_{Au} = 2.5 Å, consistent with a previous report on quantum well states in uncovered Au(111)/Fe(110) bilayers[149].

The lack of clear periodic oscillations with increasing d_{Au} is attributed to the strong interaction between Fe and AFM CoO for low spacer thicknesses. From the data presented in Fig. 6.3 (b), some quantitative conclusions can be made regarding the exchange bias and unidirectional MA. For example, the exchange bias effect follows the thickness-induced SRT in Fe. As the Fe thickness increases for a given d_{Au} (e.g., $SRT_{E \rightarrow B}$), the strongly exchange-biased hysteresis loop (E, red in Fig. 6.3 (b)) switches to a 'hard-like' and symmetric (H_{EB} = 0) loop (B, red), while the corresponding **H** || [001] loop (B, gray) becomes shifted along the external magnetic field axis. This indicates that the SRT in Fe, resulting from the change in its uniaxial MA easy axis, also drives the in-plane rotation of

the unidirectional MA axis in the system. This effect can also be observed, for example, for d_{Au}-driven $SRT_{A \rightarrow B}$.

To gain a deeper understanding of the dependence of exchange bias and unidirectional MA on Fe's uniaxial MA, magnetic hysteresis loops were systematically acquired in **H** || $[1\bar{1}0]$ geometry as a function of d_{Au} (sequences D → E → F and A → B → C) and d_{Fe} (exemplary E → B sequence). These results are shown in Fig. 6.4 (a), b, and c, respectively. The top row in Fig. 6.4 depicts the plots of normalized Fe magnetization in the remanent state at RT, which is above the CoO T_N. Three scenarios were chosen for analysis: the absence of SRT (Fig. 6.4 (a)) and both d_{Au}- and d_{Fe}-induced SRTs (Fig. 6.4 (b) and (c)).

In the case without SRT, the sample was cooled down to its positive remanent state (after saturation in positive H), and the dependence of exchange bias (d_{Au}) was observed at 80 K (green plot at the bottom of Fig. 6.4 (a), labeled as 'REM+'). A continuous, albeit non-monotonic, dependence of exchange bias on the Au thickness is observed, with a maximum magnitude of ~300 Oe for ~1 monolayer thick Au spacer, smoothly decreasing to ~70 Oe at d_{Au} = 15 Å, and complete suppression of exchange bias at the 'chimney' region with d_{Au} = 30 Å. Interestingly, the insertion of a single Au monolayer enhances the exchange bias effect in the CoO/Au/Fe trilayer by ~100% compared to direct coupling in the CoO/Fe bilayer (d_{Au} = 0). Similar effects have been reported for polycrystalline IrMn/NM/CoFe systems with NM = {Ag, Al, Ti}, intentionally rough AFM/FM interfaces[89], and thin non-magnetic spacer-induced enhancement of the exchange bias has been observed in other studies[150–152], attributed to the partial reduction of magnetic frustration at the AFM/FM interface[150,152] or increased net FM component along the biasing field[151]. The quality of the LEED diffraction images on the CoO surface is significantly worse compared to the sharp diffraction spots of the Fe(110) sublayer, which somewhat resembles the rough interface scenario described in Reference[89]. However, it is worth to note the almost exact coincidence between the observed maximum exchange bias in Fig. 6.4 (a) and the clear local maximum of the critical SRT border line in Fig. 6.3 (a) for d_{Au} = 2.5 Å. The latter could be attributed to the recently reported quantum well states (QWS) in Au(111)/Fe(110) uncovered bilayers[149]. While QWS cannot be ruled out as a driving force for the observed enhanced, Au-mediated AFM/FM exchange interaction, the absence of subsequent oscillations of

exchange bias for thicker Au does not support such an interpretation. On the other hand, the interfacial oxidation of the Fe surface during CoO growth, which negatively impacts the exchange bias effect, is suppressed by the presence of an ultrathin Au spacer. Additionally, the exchange interaction across such a thin Au film is still strong enough to ensure a significant exchange bias effect. The Au film becomes an efficient barrier against the oxidation process after the completion of its first AL, as confirmed by XAS spectra of Fe (not shown). After cooling down the sample to its second, 'negative' remanence state (labeled as 'REM-' in Fig. 6.4 (a)), a change in the sign of the H_{EB} is observed, while the magnitude (absolute value) of exchange bias depends on the spacer thickness in the same manner as after 'REM+' cooling. Comparing these two 'REM+' and 'REM-' exchange bias dependencies clearly indicates that it is the magnetic state of the FM Fe sublayer at RT that determines the direction (+/- 180°) of interfacial AFM CoO spins and, consequently, the unidirectional MA of the system below T_N. This conclusion holds true even for the highest investigated thickness of the Au spacer (15 Å) for which exchange bias is detectable. This means that the magnetic state of the Fe sublayer above the CoO T_N can be utilized to remotely control the spin orientation at the bottom interface of the AFM. Conversely, once a particular direction is established at the uncompensated CoO(111) interface, it indirectly biases the Fe magnetization below T_N towards positive or negative external magnetic field values.

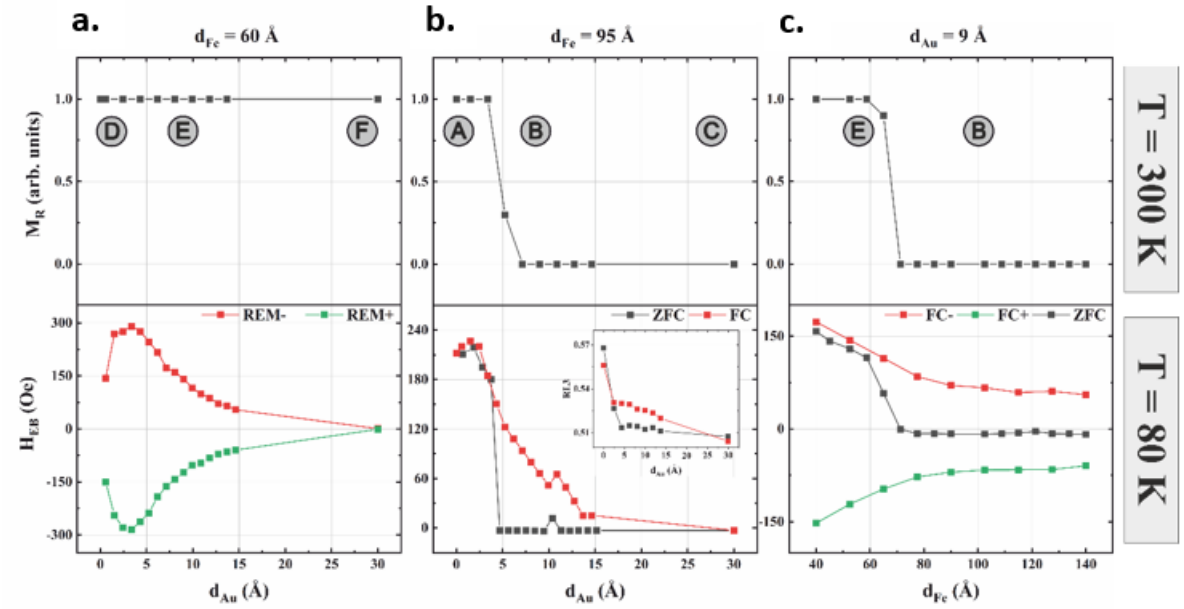

Fig. 6.4 Exchange Bias and remanence values as function of Au and Fe thicknesses conducted from several MOKE scans where **H** || [1$\bar{1}$0]. (a) REM and

H_{EB} at d_{Fe} = 60 Å as a function of d_{Au}. (b) REM and H_{EB} at d_{Fe} = 95 Å as a function of d_{Au}. (c) REM and H_{EB} at d_{Au} = 9Å as a function of d_{Fe}.

In the second scenario (d_{Au}-induced SRT for the A→B→C sequence) depicted in Fig. 6.4 (b), the sample underwent cooling in one of its remanent states. At 80 K, the behaviour of exchange bias (bottom row in Fig. 6.4 (b)) was primarily influenced by the SRT observed at RT (upper panel of Fig. 6.4 (b)). Starting from a critical thickness of d_{Au} = 5 Å, the H_{EB} drops down decreased to zero due to the switch in the easy axis of unidirectional MA to the Fe[001] in-plane orientation, which became orthogonal to the applied external magnetic field during magnetization reversal. This rotation of the unidirectional MA axis by 90° is illustrated in Fig. 6.4 (b) (grey plot). When comparing the B and C regions of interest (ROIs), an interesting evolution of magnetic hysteresis loops can be observed. Despite being equidistant from the SRT border in the two-dimensional (d_{Fe}, d_{Au}) space shown in Fig. 6.3 (a), which would typically result in similar anisotropy field values determined from hard axis [$1\bar{1}0$] magnetic hysteresis loops, the red loops in Fig. 6.3 (b) (upper panel) exhibited different saturation points, approximately at 450 Oe for the B ROI and 300 Oe for the C ROI. This apparent discrepancy can be explained by considering the freezing of interfacial CoO spins and the easy axis of unidirectional MA, which are determined by the Fe magnetization orientation above the CoO T_N. At 300 K, the Fe magnetization in the B ROI is oriented along the Fe[001] direction, resulting in an additional (unidirectional) MA that promotes the [001] orientation and makes the loop in **H** || [$1\bar{1}0$] MOKE geometry harder. In contrast, for the ROI C (chimney), the Au spacer is thick enough to completely suppress the exchange bias interaction, leading to a significantly reduced anisotropy field in **H** || [$1\bar{1}0$] compared to the B ROI.

The same effect can be observed for the E and F ROIs in Fig. 6.3 (b), but in this case, the hard-axis magnetic hysteresis loops in **H** || [001] geometry should be analysed. It is important to note that the critical SRT thickness remains unchanged as the Au thickness increases from the B and E regions (significant exchange bias) to the C and F regions (H_{EB} = 0). This is evident from the nearly flat white border line in Fig. 6.3 (a) for d_{Au} > 8 Å. Although exchange bias strongly contributes to the effective MA of Fe, it surprisingly does not shift the critical SRT thickness, which may initially appear contradictory. This can be explained by the fact that for the E → B path, the H_{EB} at 80 K rapidly drops to zero exactly

in the sample region where the SRT is observed at 300 K. In other words, in a ZFC exchange-biased system, the effective MA, including its unidirectional contribution, continuously decreases and reaches a non-zero value (still unidirectional MA is contributing) at the critical SRT region. For example, in the case of the E → B path, this can be observed close to $d_{Fe} \sim 70$ Å. Further increasing the Fe thickness causes a sudden drop and a change in the sign of the effective MA value as its last (unidirectional) component switches to an orthogonal in-plane direction. This effect is triggered by the specific MA landscape above the CoO T_N.

The situation changes significantly when the FC procedure is applied, where the Fe magnetization is aligned by the external magnetic field along the $[1\bar{1}0]$ in-plane direction for all Au thicknesses, thereby suppressing the SRT by the external magnetic field as the system passes the CoO T_N. Under these conditions, the low-temperature exchange bias no longer exhibits a jump in the H_{EB} to zero but instead continuously decreases with increasing spacer thickness, similar to what was observed in the scenario without SRT shown in Fig. 6.4 (a). However, it should be noted that for d_{Au} above approximately 5 Å, the Fe magnetization is oriented along Fe$[1\bar{1}0]$ only when forced by the external magnetic field during FC cooling. Once the field is released (H is set to zero after the FC procedure), at 80 K, the Fe magnetization switches to its intrinsic Fe[001] easy axis while the interfacial CoO spins remain frozen along the Fe$[1\bar{1}0]$ direction. Consequently, the H_{EB} remains large throughout the entire range of Au thicknesses, even though the magnetic hysteresis loops change from nearly square (typical for the easy axis) for $d_{Au} < 5$ Å to hard-like (but still exchange-biased) for thicker Au spacers. These MOKE measurements provide direct information about the unidirectional MA axis and exchange bias and can also serve as an indirect probe of the orientation of interfacial AFM spins in CoO. The inset in Fig. 6.4 (b) provides direct confirmation of these conclusions through XMLD measurements obtained at 80 K using the PIRX beamline at the National Synchrotron Radiation Centre Solaris in Kraków.

In the case of AFM CoO, as already introduced in previous chapter, the XMLD magnitude is defined by the R_{L3} ratio, which compares the intensity of two selected peaks around the L_3 absorption edge of Co in X-ray absorption spectra. The $R_{L3}(d_{Au})$ dependence is plotted in the inset of Fig. 6.4 (b) for both ZFC- and FC-cooled samples. The change in R_{L3} between $d_{Au} = 0$ and 2.5 Å correlates well with the observed enhancement of H_{EB} at

this Au thickness, indicating an increased population of frozen interfacial CoO spins oriented along the Fe[$1\bar{1}0$] in-plane direction. Furthermore, for the ZFC-cooled sample, around the critical Au thickness of ~5 Å, the XMLD magnitude (R_{L3}) decreases even more, which agrees well with the disappearance of H_{EB} at 80 K and the presence of SRT in Fe at 300 K. After the FC procedure was applied in the PIRX measurement chamber, the R_{L3} ratio no longer exhibits a rapid one-step jump at the SRT but instead continuously decreases as the interaction mediated by Au becomes weaker. In the 'chimney' position, the XMLD is almost identical for both ZFC- and FC-cooled samples, as expected when the FM-AFM interaction is no longer present.

In the third scenario (Fig. 6.4 (c)), the SRT induced by the Fe thickness was observed at $d_{Fe} \sim 70$ Å at RT. Consequently, after ZFC cooling, a sudden drop of H_{EB} to zero value occurred. However, this reduction in the H_{EB} at the critical SRT thickness was no longer observed after the FC procedure, where an external magnetic field was applied either along the Fe[$1\bar{1}0$] or antiparallel to Fe[$1\bar{1}0$] in-plane direction, resulting in negative or positive values of the H_{EB}, respectively. These results are labelled as 'FC+' and 'FC-' in Fig. 6.4 (c), similar to the 'REM+' and 'REM-' convention in plots in Fig. 6.4 (a). It should be noted that applying the 'FC+' or 'FC-' procedure in the first scenario (Fig. 6.4 (a)) leads to the same results as cooling in the 'REM+' and 'REM-' states since no SRT occurs in that sample region.

In the previous paragraphs, the interplay between the FM and AFM sublayers was demonstrated, and these results can be summarized as follows: the RT orientation of the Fe magnetization freezes the particular orientation of interfacial AFM spins as the system passes its T_N. As a result, at low temperature, these frozen AFM spins induce exchange bias and unidirectional MA in Fe, while the easy axis of uniaxial MA of Fe remains unchanged. In the following section of this chapter, examples of how the interaction with AFM can also reorient the easy axis of the effective MA of the FM layer will be provided. To achieve this, one can focus on a sample region where a large exchange bias can be induced, which naturally corresponds to thin Fe and thin Au spacer configurations. The results for such configurations are shown in Fig. 6.5.

Fig. 6.5 (a) illustrates three magnetic hysteresis loops obtained in the longitudinal MOKE geometry with an applied field parallel to the [001] direction. These loops correspond to a specific sample region near ROI D, specifically with Fe and Au thicknesses

of 70 Å and 4 Å, respectively. The first loop (blue in Fig. 6.5 (a)) represents measurements taken at 300 K and exhibits a typical "hard-like" magnetic hysteresis curve without any exchange bias effect. Upon cooling the sample to 80 K using the ZFC method, the magnetic hysteresis loop (grey in Fig. 6.5 (a)) undergoes slight changes but still retains its "hard-like" character. Importantly, the loop shows no exchange bias ($H_{EB} = 0$), and its anisotropy field (H_S) remains nearly unchanged compared to the 300 K loop. This observation is a result of the weak temperature dependence of the effective MA of Fe on the W(110) substrate. Interestingly, when the sample is cooled using the FC technique with an external magnetic field aligned parallel to [001], not only does the non-zero exchange bias emerge, but the low-temperature magnetic hysteresis loop (red in Fig. 6.5 (a)) also becomes more square-like and surely displays 100% remanent magnetization as compared to saturation magnetization. (Please note that the last comment is evident providing that remanent state for exchange biased system with asymmetric magnetic hysteresis loop should rather be defined as $\mathbf{H} = H_{EB}$ instead of $\mathbf{H} = 0$). This square-like shape is characteristic of magnetization reversal along the easy axis.

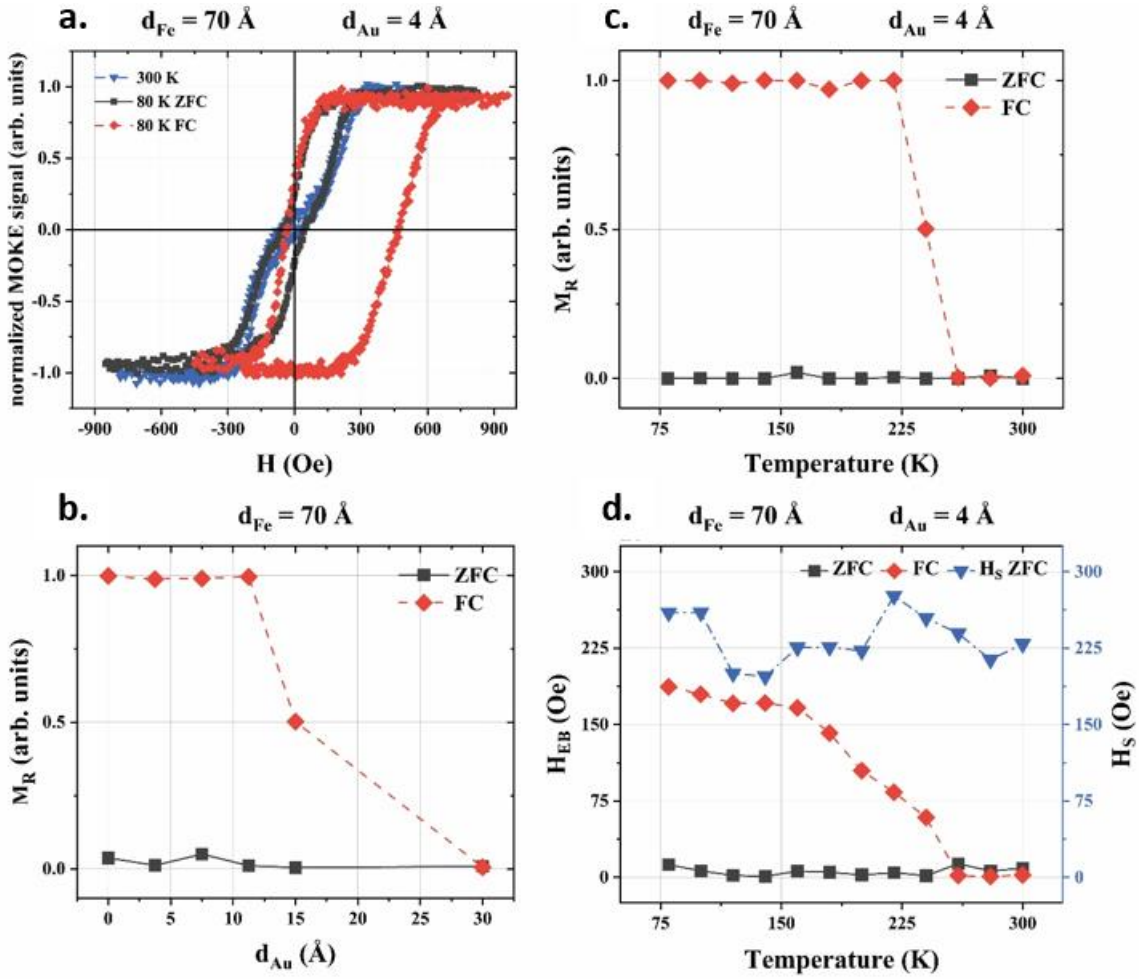

Fig. 6.5 (a) Three magnetic hysteresis loops were measured in the MOKE geometry with an applied field parallel to the [001] direction. These measurements were performed on a sample region corresponding to a Fe thickness of 70 Å and an Au thickness of 4 Å. (b) The dependencies of the magnetization in the remanent state, $M_R(d_{Au})$, at 80 K were obtained for both the FC and ZFC cooled samples. (c) The temperature dependencies of the magnetization in the remanent state, $M_R(T)$, were measured after FC (red) and ZFC (grey) cooling of the sample. (d) The temperature dependence of H_{EB} is shown in (d), along with the anisotropy field, H_s (blue), for the ZFC case.

This phenomenon can be elucidated by considering the significant contribution of an additional (unidirectional) MA, which strongly favours the orientation of Fe magnetization along the [001] axis. This effect is evident over a wide range of Au thicknesses, as depicted in Fig. 6.5 (b), where the magnetization in the remanent state (M_R) at 80 K is plotted against the d_{Au} value for both ZFC and FC samples. It is apparent

that below an Au spacer thickness of approximately 15 Å, the exchange bias serves as a robust [001] MA source, surpassing the intrinsic [$1\bar{1}0$] -like MA of Fe. At the "chimney" region, the Fe-CoO interaction is fully suppressed, and thus, even after the FC procedure, the Fe magnetization reverts to the Fe[$1\bar{1}0$] direction. Likewise, for a specific selected region of interest (ROI) in the sample, the Au-mediated Fe-CoO exchange interaction can be progressively diminished by increasing the temperature. Figures. 6.5 (c) and 6.5 (d) present the temperature dependence of the magnetization in the remanent state and the H_{EB}, respectively. Evidently, for the ZFC-cooled sample, both M_R and H_{EB} values remain near zero across the entire temperature range studied. However, after the FC procedure, the M_R reaches unity, and an H_{EB} of approximately 180 Oe is induced at 80 K, gradually diminishing with rising temperature. Consequently, the [001] contribution to the MA of Fe diminishes, and at a critical temperature of approximately 260 K, a temperature induced SRT occurs, resulting in the switch of the Fe magnetization to its intrinsic [$1\bar{1}0$] easy axis, as indicated by the M_R drop to zero in Fig 6.5 (c). Such a temperature-induced SRT can only be observed in strongly exchange-biased systems, as it originates solely from the temperature dependence of the exchange bias. In contrast, the effective MA of an exchange bias -free system (after zero-field cooling) remains largely temperature-independent, as confirmed by the H_s(T) plot in Fig. 6.5 (d) (blue curve).

In summary, by selectively choosing the ROI in the two-dimensional space defined by the thicknesses of Fe and Au, it is possible to finely control the uniaxial and unidirectional MA of Fe, as well as the strength of the Fe-CoO indirect exchange interaction mediated by Au. Consequently, a wide range of magnetic moment orientations can be stabilized within both the FM and AFM sublayers, and reorientations between distinct magnetic configurations can be triggered by variations in Fe or Au thicknesses, as well as by temperature changes. The specific magnetic state of the FM layer above the T_N of the AFM, coupled with the cooling procedure employed, plays a crucial role in determining the low-temperature orientation of interfacial AFM spins.

7. Chapter seven: Conclusion

The control of the spin orientation in antiferromagnets is of key importance in modern spintronics. The research findings demonstrate the possibility of manipulating and controlling the magnetic properties of multilayer systems through precise interface engineering and thermal-hysteresis-induced spin reorientation processes. Fine-tuning the interfacial MA at the sub-nano scale enables the realization of two orthogonal magnetic states in the exchange-coupled AFM adjacent to FM in NiO(111)/Fe(110) bilayers. The ability to achieve either of two orthogonal magnetic states in AFM, as schematically shown in Fig. 7.1, with field-free switching between them may potentially lead to new ideas and applications for example in what is known as heat-assisted magnetic recording (HAMR). The critical temperature for such reversal can be precisely tuned, covering the range from 250 to 370 K, including RT. Magnetic hysteresis loops confirm the fully rotatable nature of the NiO spins, which can be switched by small external magnetic fields due to strong interfacial exchange coupling with neighbouring Fe moments.

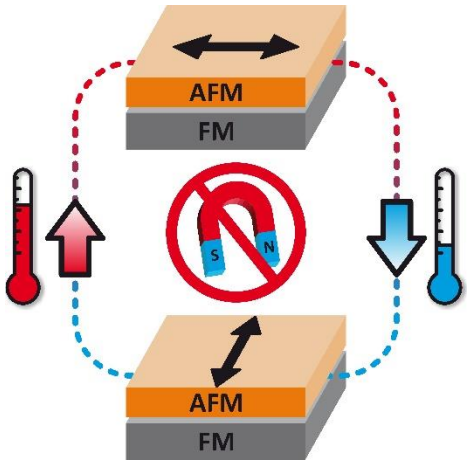

Fig. 7.1 A sketch showing two orthogonal magnetic states of AFM in AFM/FM system without necessity of applying external magnetic field to switch between them.

The next study presented in chapter five of this thesis focuses on CoO(111)/Fe(110) systems. By means of XMLD and MOKE techniques it was shown that the orientation of CoO magnetic spins is influenced by the underlying Fe thickness-induced spin reorientation transition. This orientation change in CoO is observed below

its T_N and remains "frozen" as long as the system is below T_N of antiferromagnetic CoO layer, independently on the low temperature magnetic state of Fe.

Fig 7.2 shows a specific orientation of frozen AFM spins that can be programmed in a CoO(111)/Fe(110) bilayer and detected by changes in the exchange-biased magnetic hysteresis loop. By cooling the sample down from various remanent states above ' T_N of CoO, Fig 7.2 (a) and (b) demonstrate the imprinting of the CoO spin orientation by the Fe layer's magnetization orientation. This imprinting affects the MA of the system, showing the intricate interplay of ferromagnet-antiferromagnet interactions.

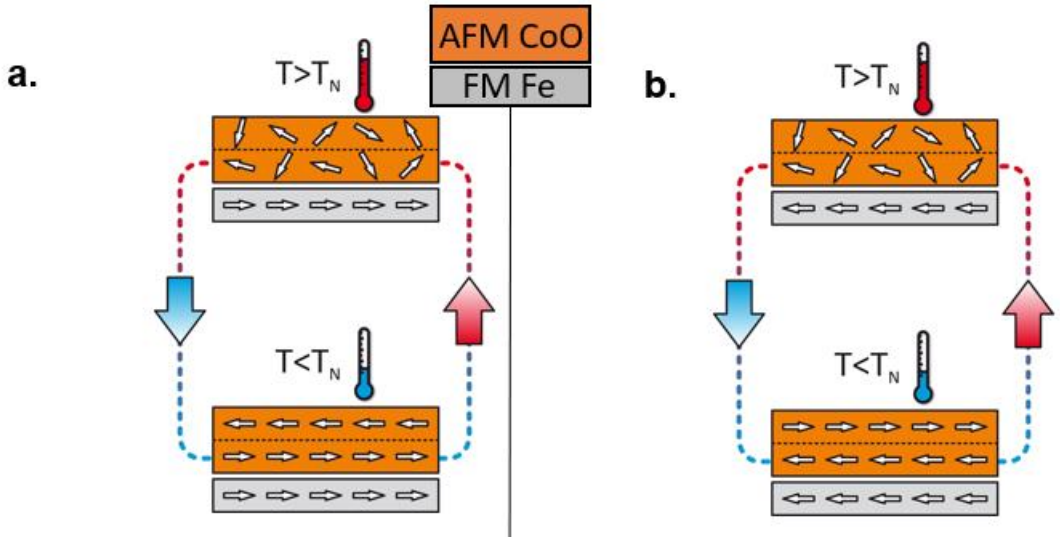

Fig. 7.2 Representation of the magnetic orientation of the AFM layer in the AFM/FM system above and below its Neel temperature.

Lastly, the investigation of CoO(111)/Au(111)/Fe(110) systems reveals that precise control over the MA of the Fe layer and the strength of the Fe-CoO indirect exchange interaction can be achieved by choosing specific regions of MA landscape spanned over the two-dimensional Fe and Au thickness space. This allows for the stabilization of various magnetic moment orientations in both the FM and AFM sublayers, with the possibility of triggering spin reorientations through adjustments of thickness or temperature. The choice of the FM layer's magnetic state above the T_N, along with the cooling procedure, plays a crucial role in determining the low-temperature orientation of interfacial AFM spins.

8. References

1. Wadley, P. *et al.* Electrical switching of an antiferromagnet. *Science (1979)* **351**, 587–590 (2016).
2. Sander, D. *et al.* The 2017 Magnetism Roadmap. *J Phys D Appl Phys* **50**, 363001 (2017).
3. Dieny, B. *et al.* Giant magnetoresistive in soft ferromagnetic multilayers. *Phys Rev B* **43**, 1297–1300 (1991).
4. Baltz, V. *et al.* Antiferromagnetic spintronics. *Rev Mod Phys* **90**, 015005 (2018).
5. Haney, P. M., Duine, R. A., Núñez, A. S. & MacDonald, A. H. Current-induced torques in magnetic metals: Beyond spin-transfer. *J Magn Magn Mater* **320**, 1300–1311 (2008).
6. MacDonald, A. H. & Tsoi, M. Antiferromagnetic metal spintronics. *Philosophical Transactions of the Royal Society A: Mathematical, Physical and Engineering Sciences* **369**, 3098–3114 (2011).
7. Gomonay, E. V. & Loktev, V. M. Spintronics of antiferromagnetic systems (Review Article). *Low Temperature Physics* **40**, 17–35 (2014).
8. Sklenar, J. *et al.* Spin Hall effects in metallic antiferromagnets – perspectives for future spin-orbitronics. *AIP Adv* **6**, 055603 (2016).
9. Fina, I. & Marti, X. Electric control of antiferromagnets. *IEEE Trans Magn* 1–1 (2016) doi:10.1109/TMAG.2016.2606561.
10. Jungwirth, T., Marti, X., Wadley, P. & Wunderlich, J. Antiferromagnetic spintronics. *Nat Nanotechnol* **11**, 231–241 (2016).
11. Bommanaboyena, S. P. *et al.* Readout of an antiferromagnetic spintronics system by strong exchange coupling of Mn2Au and Permalloy. *Nat Commun* **12**, 6539 (2021).
12. A Bland, B Heinrich & JAC Bland. Ultrathin Magnetic Structures. **I + II**, (1994).
13. Jensen, P. J. & Bennemann, K. H. Magnetism of Interacting Two-Dimensional Nanostructures. in *Frontiers in Magnetic Materials* 459–501 (Springer-Verlag, 2005). doi:10.1007/3-540-27284-4_16.
14. Weller, D. & Moser, A. Thermal effect limits in ultrahigh-density magnetic recording. *IEEE Trans Magn* **35**, 4423–4439 (1999).
15. Falicov, L. M. *et al.* Surface, interface, and thin-film magnetism. *J Mater Res* **5**, 1299–1340 (1990).
16. Jensen, P. & Bennemann, K. Magnetic structure of films: Dependence on anisotropy and atomic morphology. *Surf Sci Rep* **61**, 129–199 (2006).

17. Zuckermann, M. J. The proximity effect for weak itinerant ferromagnets. *Solid State Commun* **12**, 745–747 (1973).

18. Hasegawa, H. & Herman, F. Finite-temperature band theory of ferromagnetic-antiferromagnetic interfaces including exchange anisotropy. *Phys Rev B* **38**, 4863–4872 (1988).

19. Altbir, D., Kiwi, M., Martnez, G. & Zuckermann, M. J. Magnetic metal films on paramagnetic substrates: A theoretical study. *Phys Rev B* **40**, 6963–6970 (1989).

20. J. Stöhr & H. Siegmann. *Magnetism*. (2009).

21. Aharoni, A. Introduction to the Theory of Ferromagnetism. **109**, (2000).

22. Néel, L. Anisotropie magnétique superficielle et surstructures d'orientation. *Journal de Physique et le Radium* **15**, 225–239 (1954).

23. Pappas, D. P., Kämper, K.-P. & Hopster, H. Reversible transition between perpendicular and in-plane magnetization in ultrathin films. *Phys Rev Lett* **64**, 3179–3182 (1990).

24. Stöhr, J. Exploring the microscopic origin of magnetic anisotropies with X-ray magnetic circular dichroism (XMCD) spectroscopy. *J Magn Magn Mater* **200**, 470–497 (1999).

25. van Vleck, J. H. On the Anisotropy of Cubic Ferromagnetic Crystals. *Physical Review* **52**, 1178–1198 (1937).

26. Carcia, P. F., Meinhaldt, A. D. & Suna, A. Perpendicular magnetic anisotropy in Pd/Co thin film layered structures. *Appl Phys Lett* **47**, 178–180 (1985).

27. Gradmann, U. & Müller, J. Flat Ferromagnetic, Epitaxial 48Ni/52Fe(111) Films of few Atomic Layers. *Physica Status Solidi (b)* **27**, 313–324 (1968).

28. Kittel, C. *Introduction to solid state physics*. (1996).

29. Trygg, J., Johansson, B., Eriksson, O. & Wills, J. M. Total Energy Calculation of the Magnetocrystalline Anisotropy Energy in the Ferromagnetic 3d Metals. *Phys Rev Lett* **75**, 2871–2874 (1995).

30. van Vleck, J. H. On the Anisotropy of Cubic Ferromagnetic Crystals. *Physical Review* **52**, 1178–1198 (1937).

31. Bruno, P. *Magnetismus von Festkörpern und Grenzflächen*. (1993).

32. Johnson, M. T., Bloemen, P. J. H., Broeder, F. J. A. den & Vries, J. J. de. Magnetic anisotropy in metallic multilayers. *Reports on Progress in Physics* **59**, 1409–1458 (1996).

33. Bruno, P. & Renard, J.-P. Magnetic surface anisotropy of transition metal ultrathin films. *Applied Physics A Solids and Surfaces* **49**, 499–506 (1989).

34. Gradmann, U. Chapter 1 Magnetism in ultrathin transition metal films. in 1–96 (1993). doi:10.1016/S1567-2719(05)80042-3.

35. Bruno, P. Physical origins and theoretical models of magnetic anisotropy. *Magnetismus von Festkörpern und grenzflächen* **24**, (1993).

36. Sander, D. The magnetic anisotropy and spin reorientation of nanostructures and nanoscale films. *Journal of Physics: Condensed Matter* **16**, R603–R636 (2004).

37. Gradmann, U., Korecki, J. & Waller, G. In-plane magnetic surface anisotropies in Fe(110). *Applied Physics A Solids and Surfaces* **39**, 101–108 (1986).

38. M. Ślęzak. Wpływ morfologii podłoża na magnetyzm epitaksjalnych nanostruktur metali 3d. (Akademia Górniczo-Hutnicza w Krakowie, 2009).

39. Albrecht, M., Furubayashi, T., Przybylski, M., Korecki, J. & Gradman, U. Magnetic step anisotropies. *J Magn Magn Mater* **113**, 207–220 (1992).

40. Baek, I. G., Lee, H. G., Kim, H. J. & Vescovo, E. Spin reorientation transition in Fe(110) thin films: The role of surface anisotropy. *Phys Rev B Condens Matter Mater Phys* **67**, (2003).

41. Fruchart, O., Nozières, J.-P. & Givord, D. Temperature-driven in-plane anisotropy reorientation transition in Fe(110) films. *J Magn Magn Mater* **165**, 508–511 (1997).

42. Moschel, A. & Usadel, K. D. Reorientation transitions of first and second order in thin ferromagnetic films. *Phys Rev B* **51**, 16111–16114 (1995).

43. Allenspach, R. Ultrathin films: magnetism on the microscopic scale. *J Magn Magn Mater* **129**, 160–185 (1994).

44. Millev, Y. & Kirschner, J. Reorientation transitions in ultrathin ferromagnetic films by thickness- and temperature-driven anisotropy flows. *Phys Rev B* **54**, 4137–4145 (1996).

45. Gerhardter, F., Li, Y. & Baberschke, K. Temperature-dependent ferromagnetic-resonance study in ultrahigh vacuum: Magnetic anisotropies of thin iron films. *Phys Rev B* **47**, 11204–11210 (1993).

46. Shull, C. G. & Smart, J. S. Detection of Antiferromagnetism by Neutron Diffraction. *Physical Review* **76**, 1256–1257 (1949).

47. Finazzi, M., Duò, L. & Ciccacci, F. Magnetic properties of interfaces and multilayers based on thin antiferromagnetic oxide films. *Surf Sci Rep* **64**, 139–167 (2009).

48. *Magnetic Properties of Antiferromagnetic Oxide Materials*. (2010).

49. Gray, I. *et al.* Spin Seebeck Imaging of Spin-Torque Switching in Antiferromagnetic Pt/NiO Heterostructures. *Phys Rev X* **9**, 041016 (2019).

50. Kozioł-Rachwał, A. *et al.* Control of spin orientation in antiferromagnetic NiO by epitaxial strain and spin-flop coupling. *APL Mater* **8**, (2020).

51. Mermin, N. D. & Wagner, H. Absence of Ferromagnetism or Antiferromagnetism in One- or Two-Dimensional Isotropic Heisenberg Models. *Phys Rev Lett* **17**, 1133–1136 (1966).

52. SAKO, S., OHSHIMA, K., SAKAI, M. & BANDOW, S. Magnetic property of CoO ultrafine particle. *Surface Review and Letters* **03**, 109–113 (1996).

53. Fisher, M. E. & Barber, M. N. Scaling Theory for Finite-Size Effects in the Critical Region. *Phys Rev Lett* **28**, 1516–1519 (1972).

54. Zhang, R. & Willis, R. F. Thickness-Dependent Curie Temperatures of Ultrathin Magnetic Films: Effect of the Range of Spin-Spin Interactions. *Phys Rev Lett* **86**, 2665–2668 (2001).

55. Song, C. *et al.* How to manipulate magnetic states of antiferromagnets. *Nanotechnology* vol. 29 Preprint at https://doi.org/10.1088/1361-6528/aaa812 (2018).

56. Han, J. H. *et al.* Antiferromagnet-controlled spin current transport in SrMnO3/Pt hybrids. *Phys Rev B* **90**, 144431 (2014).

57. Hoogeboom, G. R., Aqeel, A., Kuschel, T., Palstra, T. T. M. & van Wees, B. J. Negative spin Hall magnetoresistance of Pt on the bulk easy-plane antiferromagnet NiO. *Appl Phys Lett* **111**, (2017).

58. Sapozhnik, A. A. *et al.* Manipulation of antiferromagnetic domain distribution in Mn2Au by ultrahigh magnetic fields and by strain. *physica status solidi (RRL) - Rapid Research Letters* **11**, 1600438 (2017).

59. Meiklejohn, W. H. & Bean, C. P. New Magnetic Anisotropy. *Physical Review* **102**, 1413–1414 (1956).

60. Zhang, W. & Krishnan, K. M. Epitaxial exchange-bias systems: From fundamentals to future spin-orbitronics. *Materials Science and Engineering: R: Reports* **105**, 1–20 (2016).

61. Manna, P. K. & Yusuf, S. M. Two interface effects: Exchange bias and magnetic proximity. *Phys Rep* **535**, 61–99 (2014).

62. Soeya, S., Nakamura, S., Imagawa, T. & Narishige, S. Rotational hysteresis loss study on exchange coupled Ni81Fe19/NiO films. *J Appl Phys* **77**, 5838–5842 (1995).

63. Tsunoda, M., Tsuchiya, Y., Hashimoto, T. & Takahashi, M. Magnetic anisotropy and rotational hysteresis loss in exchange coupled Ni–Fe/Mn–Ir films. *J Appl Phys* **87**, 4375–4388 (2000).

64. Jiménez, E. *et al.* Emergence of noncollinear anisotropies from interfacial magnetic frustration in exchange-bias systems. *Phys Rev B* **80**, 014415 (2009).

65. Leighton, C. *et al.* Two-Stage Magnetization Reversal in Exchange Biased Bilayers. *Phys Rev Lett* **86**, 4394–4397 (2001).

66. Nogués, J., Leighton, C. & Schuller, I. K. Correlation between antiferromagnetic interface coupling and positive exchange bias. *Phys Rev B* **61**, 1315–1317 (2000).

67. Scholl, A., Liberati, M., Arenholz, E., Ohldag, H. & Stöhr, J. Creation of an antiferromagnetic exchange spring. *Phys Rev Lett* **92**, (2004).

68. Camarero, J. *et al.* Magnetization reversal, asymmetry, and role of uncompensated spins in perpendicular exchange coupled systems. *Appl Phys Lett* **89**, (2006).

69. Sampaio, L. C. *et al.* Probing interface magnetism in the FeMn/NiFe exchange bias system using magnetic second-harmonic generation. *Europhysics Letters (EPL)* **63**, 819–825 (2003).

70. Ślęzak, M. *et al.* Memory of frozen and rotatable antiferromagnetic spins in epitaxial CoO(1 1 1)/Fe and NiO(1 1 1)/Fe bilayers. *Nucl Instrum Methods Phys Res B* **539**, 148–151 (2023).

71. Ślęzak, M. *et al.* Tailorable exchange bias and memory of frozen antiferromagnetic spins in epitaxial CoO(1 1 1)/Fe(1 1 0) bilayers. *J Magn Magn Mater* **545**, (2022).

72. Ślęzak, M. *et al.* Controllable magnetic anisotropy and spin orientation of a prototypical easy-plane antiferromagnet on a ferromagnetic support. *Phys Rev B* **104**, (2021).

73. Ohldag, H. *et al.* Correlation between Exchange Bias and Pinned Interfacial Spins. *Phys Rev Lett* **91**, 017203 (2003).

74. Camarero, J. *et al.* Field dependent exchange coupling in NiO/Co bilayers. *Phys Rev B* **67**, 020413 (2003).

75. Koon, N. C. Calculations of Exchange Bias in Thin Films with Ferromagnetic/Antiferromagnetic Interfaces. *Phys Rev Lett* **78**, 4865–4868 (1997).

76. Tsai, S.-H., Landau, D. P. & Schulthess, T. C. Effect of interfacial coupling on the magnetic ordering in ferro-antiferromagnetic bilayers. *J Appl Phys* **93**, 8612–8614 (2003).

77. Finazzi, M. Interface coupling in a ferromagnet/antiferromagnet bilayer. *Phys Rev B* **69**, 064405 (2004).

78. Finazzi, M., Biagioni, P., Brambilla, A., Duò, L. & Ciccacci, F. Disclinations in thin antiferromagnetic films on a ferromagnetic substrate. *Phys Rev B* **72**, 024410 (2005).

79. Finazzi, M. *et al.* Magnetic anisotropy of NiO epitaxial thin films on Fe(001). *Phys Rev B* **69**, 014410 (2004).

80. Finazzi, M. *et al.* Interface Coupling Transition in a Thin Epitaxial Antiferromagnetic Film Interacting with a Ferromagnetic Substrate. *Phys Rev Lett* **97**, 097202 (2006).

81. Parkin, S. S. P., More, N. & Roche, K. P. Oscillations in exchange coupling and magnetoresistance in metallic superlattice structures: Co/Ru, Co/Cr, and Fe/Cr. *Phys Rev Lett* **64**, 2304–2307 (1990).

82. Stiles, M. D. Interlayer exchange coupling. *J Magn Magn Mater* **200**, 322–337 (1999).

83. Yosida, K. Magnetic Properties of Cu-Mn Alloys. *Physical Review* **106**, 893–898 (1957).

84. Ruderman, M. A. & Kittel, C. Indirect Exchange Coupling of Nuclear Magnetic Moments by Conduction Electrons. *Physical Review* **96**, 99–102 (1954).

85. Elmers, H. J., Liu, G., Fritzsche, H. & Gradmann, U. Indirect exchange coupling for orthogonal anisotropies. *Phys Rev B* **52**, R696–R699 (1995).

86. Nayyef, H. *et al.* Tunable interplay between exchange coupling and uniaxial magnetic anisotropy in epitaxial CoO/Au/Fe trilayers. *Sci Rep* **13**, 10902 (2023).

87. Gökemeijer, N., Ambrose, T. & Chien, C. Long-Range Exchange Bias across a Spacer Layer. *Phys Rev Lett* **79**, 4270–4273 (1997).

88. Paul, A., Bürgler, D. E., Luysberg, M. & Grünberg, P. Enhanced exchange bias due to an ultra-thin, non-magnetic insulator spacer layer. *Europhysics Letters (EPL)* **68**, 233–239 (2004).

89. Thomas, L., Kellock, A. J. & Parkin, S. S. P. On the exchange biasing through a nonmagnetic spacer layer. *J Appl Phys* **87**, 5061–5063 (2000).

90. J. Wiley. *The characterization of high-temperature vapors*. (1967).

91. Knudsen, M. Die Gesetze der Molekularströmung und der inneren Reibungsströmung der Gase durch Röhren. *Ann Phys* **333**, 75–130 (1909).

92. Arthur, J. R. Molecular beam epitaxy. *Surf Sci* **500**, 189–217 (2002).

93. Yates, J. T. Surface Science: An Introduction. *Phys Today* **57**, 79–80 (2004).

94. Oura, K., Katayama, M., Zotov, A. V., Lifshits, V. G. & Saranin, A. A. Surface Analysis I. Diffraction Methods. in 47–75 (2003). doi:10.1007/978-3-662-05179-5_4.

95. Michael Faraday. I. Experimental researches in electricity.—Nineteenth series. *Philos Trans R Soc Lond* **136**, 1–20 (1846).

96. Kerr, J. XLIII. *On rotation of the plane of polarization by reflection from the pole of a magnet*. *The London, Edinburgh, and Dublin Philosophical Magazine and Journal of Science* **3**, 321–343 (1877).

97. Jaroslav Hamrle. Magneto-optical determination of the in-depth magnetization profile in magnetic multilayers. Condensed Matter. (Université Paris Sud , 2003).

98. Ferré, J., Jamet, J. P. & Meyer, P. Magneto-Optical Studies of Magnetic Ultrathin Film Structures. *physica status solidi (a)* **175**, 213–223 (1999).

99. Koopmans, B., van Kampen, M., Kohlhepp, J. T. & de Jonge, W. J. M. Ultrafast Magneto-Optics in Nickel: Magnetism or Optics? *Phys Rev Lett* **85**, 844–847 (2000).

100. Hubert, A. & Schäfer, R. Domain Theory. in *Magnetic Domains* 99–335 (Springer Berlin Heidelberg). doi:10.1007/978-3-540-85054-0_3.

101. Devolder, T. *et al.* Sub-50 nm planar magnetic nanostructures fabricated by ion irradiation. *Appl Phys Lett* **74**, 3383–3385 (1999).

102. Bruno, P. Tight-binding approach to the orbital magnetic moment and magnetocrystalline anisotropy of transition-metal monolayers. *Phys Rev B* **39**, 865–868 (1989).

103. Schütz, G. *et al.* Absorption of circularly polarized x rays in iron. *Phys Rev Lett* **58**, 737–740 (1987).

104. Dunn, J. H. *et al.* An angle-dependent magnetic circular X-ray dichroism study of Co/Cu(100): experiment versus theory. *Journal of Physics: Condensed Matter* **7**, 1111–1119 (1995).

105. Samant, M. G. *et al.* Induced spin polarization in Cu spacer layers in Co/Cu multilayers. *Phys Rev Lett* **72**, 1112–1115 (1994).

106. Dürr, H. A. & van der Laan, G. Magnetic circular x-ray dichroism in transverse geometry: Importance of noncollinear ground state moments. *Phys Rev B* **54**, R760–R763 (1996).

107. Carra, P., Thole, B. T., Altarelli, M. & Wang, X. X-ray circular dichroism and local magnetic fields. *Phys Rev Lett* **70**, 694–697 (1993).

108. Baberschke, K. The magnetism of nickel monolayers. *Appl Phys A Mater Sci Process* **62**, 417–427 (1996).

109. Idzerda, Y. U. *et al.* Magnetic structure of Fe/Cr/Fe trilayers. *Phys Rev B* **48**, 4144–4147 (1993).

110. Stöhr, J. *et al.* Element-Specific Magnetic Microscopy with Circularly Polarized X-rays. *Science (1979)* **259**, 658–661 (1993).

111. Aspelmeier, A. *et al.* Ac susceptibility measurements of magnetic monolayers: MCXD, MOKE, and mutual inductance. *J Magn Magn Mater* **146**, 256–266 (1995).

112. Chen, C. T. *et al.* Element-specific magnetic hysteresis as a means for studying heteromagnetic multilayers. *Phys Rev B* **48**, 642–645 (1993).

113. Tjeng, L. H., Idzerda, Y. U., Rudolf, P., Sette, F. & Chen, C. T. Soft-X-ray magnetic circular dichroism: a new technique for probing magnetic properties of magnetic surfaces and ultrathin films. *J Magn Magn Mater* **109**, 288–292 (1992).

114. Ulises, M. & Rivas, G. *X-ray magnetic circular dichroism (XMCD)*. (2021).

115. Nogués, J. *et al.* Isothermal tuning of exchange bias using pulsed fields. *Appl Phys Lett* **82**, 3044–3046 (2003).

116. Machado, F. L. A. *et al.* Spin-flop transition in the easy-plane antiferromagnet nickel oxide. *Phys Rev B* **95**, (2017).

117. Kuch, W. *et al.* Tuning the magnetic coupling across ultrathin antiferromagnetic films by controlling atomic-scale roughness. *Nat Mater* **5**, 128–133 (2006).

118. Gradmann, U., Korecki, J. & Waller, G. *In-Plane Magnetic Surface Anisotropies in Fe(110)*. *Appl. Phys. A* vol. 39 (1986).

119. Ślęzak, M. *et al.* Multiple spin reorientation transitions and large in plane magnetic anisotropy in epitaxial Au/Co/Fe(1 1 0) films. *J Magn Magn Mater* **475**, 195–200 (2019).

120. Ślęzak, M. *et al.* Giant in-plane magnetic anisotropy in epitaxial bcc Co/Fe(110) bilayers. *Phys Rev B* **94**, (2016).

121. Wu, Y. Z. *et al.* Tailoring the spin direction of antiferromagnetic NiO thin films grown on vicinal Ag(001). *Phys Rev B* **74**, 212402 (2006).

122. Vescovo, E. *et al.* Domain faceting in an in-plane magnetic reorientation transition. *Phys Rev B Condens Matter Mater Phys* **82**, (2010).

123. Gradmann, U., Dürkop, T. & Elmers, H. J. Magnetic moments and anisotropies in smooth and rough surfaces and interfaces. *J Magn Magn Mater* **165**, 56–61 (1997).

124. Arenholz, E., Van Der Laan, G., Chopdekar, R. V. & Suzuki, Y. Angle-dependent Ni2+ X-ray magnetic linear dichroism: Interfacial coupling revisited. *Phys Rev Lett* **98**, (2007).

125. Arenholz, E., Van Der Laan, G. & Nolting, F. Magnetic structure near the CoNiO (001) interface. *Appl Phys Lett* **93**, (2008).

126. Alders, D. *et al. Temperature and thickness dependence of magnetic moments in NiO epitaxial films*. (1998).

127. Kurosawa, K., Miura, M. & Saito, S. Magnetic torque measurements on NiO (111) platelets. *Journal of Physics C: Solid State Physics* **13**, 1521–1527 (1980).

128. Abrudan, R. *et al.* Structural and magnetic properties of epitaxial Fe/CoO bilayers on Ag(001). *Phys Rev B Condens Matter Mater Phys* **77**, (2008).

129. Wu, J. *et al.* Direct measurement of rotatable and frozen CoO spins in exchange bias system of CoO/Fe/Ag(001). *Phys Rev Lett* **104**, (2010).

130. Zhu, J. *et al.* Strain-modulated antiferromagnetic spin orientation and exchange coupling in Fe/CoO(001). *J Appl Phys* **115**, (2014).

131. Brambilla, A. *et al.* Magnetic properties of the CoO/Fe(001) system with a bottom-up engineered interface. *J Magn Magn Mater* **475**, 54–59 (2019).

132. Giannotti, D. *et al.* Magnetic anisotropy at the buried CoO/Fe interface. *Appl Phys Lett* **109**, (2016).

133. Li, Q. *et al.* Activation of antiferromagnetic domain switching in exchange-coupled Fe/CoO/MgO(001) systems. *Phys Rev B Condens Matter Mater Phys* **91**, (2015).

134. Nowak, G. *et al.* Structural and magnetic properties of stoichiometric epitaxial CoO Fe exchange-bias bilayers. *Phys Rev B Condens Matter Mater Phys* **75**, (2007).

135. Gökemeijer, N. J. & Chien, C. L. Memory effects of exchange coupling in [formula omitted] bilayers. in *Journal of Applied Physics* vol. 85 5516–5518 (1999).

136. Miltényi, P. *et al.* Tuning exchange bias. *Appl Phys Lett* **75**, 2304–2306 (1999).

137. Li, Q. *et al.* Antiferromagnetic proximity effect in epitaxial CoO/NiO/MgO(001) systems. *Sci Rep* **6**, (2016).

138. Fruchart, O., Nozieres, J. P. & Givord, D. Temperature-driven in-plane anisotropy reorientation transition in Fe(110) films. *J Magn Magn Mater* **165**, 508–511 (1997).

139. Stiles, M. D. & McMichael, R. D. Coercivity in exchange-bias bilayers. *Phys Rev B* **63**, 064405 (2001).

140. Fulcomer, E. & Charap, S. H. Thermal fluctuation aftereffect model for some systems with ferromagnetic-antiferromagnetic coupling. *J Appl Phys* **43**, 4190–4199 (1972).

141. Shi, H., Lederman, D. & Fullerton, E. E. Exchange bias in FexZn1−xF2/Co bilayers . *J Appl Phys* **91**, 7763 (2002).

142. Chung, S. H., Hoffmann, A. & Grimsditch, M. Interplay between exchange bias and uniaxial anisotropy in a ferromagnetic/antiferromagnetic exchange-coupled system. *Phys Rev B Condens Matter Mater Phys* **71**, (2005).

143. Fraune, M., Rüdiger, U., Güntherodt, G., Cardoso, S. & Freitas, P. Size dependence of the exchange bias field in NiO/Ni nanostructures. *Appl Phys Lett* **77**, 3815–3817 (2000).

144. Hoffmann, A. *et al.* Tailoring the exchange bias via shape anisotropy in ferromagnetic/antiferromagnetic exchange-coupled systems. *Phys Rev B* **67**, 220406 (2003).

145. Oepen, H. P., Millev, Y. T. & Kirschner, J. The reorientation transition in Co/Au(111). *J Appl Phys* **81**, 5044–5046 (1997).

146. Oepen, H. P., Speckmann, M., Millev, Y. & Kirschner, J. Unified approach to thickness-driven magnetic reorientation transitions. *Phys Rev B* **55**, 2752–2755 (1997).

147. Ślęzak, M., Ślęzak, T., Matlak, K., Drózdz, P. & Korecki, J. Adsorption induced modification of in-plane magnetic anisotropy in epitaxial Co and Fe/Co films on Fe(110). *AIP Adv* **8**, (2018).

148. Ślęzak, M. *et al.* From Termination Dependent Chemical Sensitivity of Spin Orientation in All-bcc Fe/Co Magnetic Superlattices toward the Concept of an Artificial Surface of a Ferromagnet. *J Phys Chem Lett* **13**, 8522–8528 (2022).

149. Ślęzak, M. *et al.* Oscillating magnetic anisotropy in epitaxial Au/Fe(1 1 0) and Co/Au/Fe(1 1 0) films. *J Magn Magn Mater* **497**, (2020).

150. Kozioł-Rachwał, A. *et al.* Interface engineering towards enhanced exchange interaction between Fe and FeO in Fe/MgO/FeO epitaxial heterostructures. *Appl Phys Lett* **115**, (2019).

151. Garcia, F., Sort, J., Rodmacq, B., Auffret, S. & Dieny, B. Large anomalous enhancement of perpendicular exchange bias by introduction of a nonmagnetic spacer between the ferromagnetic and antiferromagnetic layers. *Appl Phys Lett* **83**, 3537–3539 (2003).

152. Vinai, G., Moritz, J., Bandiera, S., Prejbeanu, I. L. & Dieny, B. Large exchange bias enhancement in (Pt(or Pd)/Co)/IrMn/Co trilayers with ultrathin IrMn thanks to interfacial Cu dusting. *Appl Phys Lett* **104**, (2014).

9. List of the author's publications

- H. Nayyef et al. Tunable interplay between exchange coupling and uniaxial magnetic anisotropy in epitaxial CoO/Au/Fe trilayers. Scientific Reports, volume 13/10902 (2023). DOI: 10.1038/s41598-023-38098-6
- M. Ślęzak et al. Memory of frozen and rotatable antiferromagnetic spins in epitaxial CoO (1 1 1)/Fe and NiO(1 1 1)/Fe bilayers. Nuclear Instruments and Methods in Physics Research Section B: Beam Interactions with Materials and Atoms, Volume 539/148-151 (2023). DOI:10.1016/j.nimb.2023.03.038
- W. Janus et al. Tunable magnetic anisotropy of antiferromagnetic NiO in (Fe)/ NiO/MgO/Cr/MgO(001) epitaxial multilayers. Scientific Reports, volume 13/4824 (2023)DOI:10.1038/s41598-023-31930-z
- A. Kozioł-Rachwał et al. Beating the limitation of the Néel temperature of FeO with antiferromagnetic proximity in FeO/CoO. Appl. Phys. Lett. volume 120/072404 (2022) DOI: 10.1063/5.0082729
- M. Ślęzak et al. Tailorable exchange bias and memory of frozen antiferromagnetic spins in epitaxial CoO(111)/Fe(110) bilayers. Journal of Magnetism and Magnetic Materials, Volume 545/168783 (2021). DOI: 10.1016/j.jmmm.2021.168783
- M. Ślęzak et al. Controllable magnetic anisotropy and spin orientation of a prototypical easy-plane antiferromagnet on a ferromagnetic support. Phys. Rev. B volume104/ 34434 (2021). DOI: 10.1103/PhysRevB.104.134434
- P. Dróżdż et al. Driving the polar spin reorientation transition of ultrathin ferromagnets with antiferromagnetic– ferromagnetic

phase transition of nearby FeRh alloy film. Scientific Reports volume 10/ 14901 (2020) DOI:10.1038/s41598-020-71912-z

- M. Ślęzak et al. Fine tuning of ferromagnet/antiferromagnet interface magnetic anisotropy for field-free switching of antiferromagnetic spins. Nanoscale, volume 12/ 18091-18095 (2020). DOI: 10.1039/D0NR04193A
- A. Kozioł-Rachwał et al. Control of spin orientation in antiferromagnetic NiO by epitaxial strain and spin-flop coupling. APL Materials volume 8/061107 (2020)DOI:10.1063/5.0011736